

SCALABLE SYNTHESIS AND DYNAMIC MECHANICAL CHARACTERIZATION OF  
MULTIFUNCTIONAL POLYMER AEROGELS

by

Sadeq Malakooti



APPROVED BY SUPERVISORY COMMITTEE:

---

Hongbing Lu, Chair

---

Ray H. Baughman

---

Dong Qian

---

Ill Ryu

---

Terry Baughn

Copyright © 2020

Sadeq Malakooti

All Rights Reserved

*To my loves, Nastaran and Nika Nancy*

SCALABLE SYNTHESIS AND DYNAMIC MECHANICAL CHARACTERIZATION OF  
MULTIFUNCTIONAL POLYMER AEROGELS

by

SADEQ MALAKOOTI, BS, MSc, MSc

DISSERTATION

Presented to the Faculty of

The University of Texas at Dallas

in Partial Fulfillment

of the Requirements

for the Degree of

DOCTOR OF PHILOSOPHY IN

MECHANICAL ENGINEERING

THE UNIVERSITY OF TEXAS AT DALLAS

May 2020

## ACKNOWLEDGMENTS

I have been privileged in my life for having many dedicated and devoted teachers who have taken an interest in me and from whom I have learned a lot about life. Foremost, I would like to express my sincere appreciation to Professor Hongbing Lu for his guidance, support, motivation, enthusiasm, and immense knowledge during the entire course of this study. Furthermore, I would like to express my appreciation to Professor Nicholas Leventis at the Department of Chemistry at Missouri University of Science and Technology for his help and guidance on the chemistry side of the work. I would also like to express my appreciation to Professor Ning Xiang at the School of Architecture at Rensselaer Polytechnic Institute for his guidance on the acoustic measurements. I also appreciate the guidance of the other members of the supervisory committee; Dr. Ray H. Baughman, Dr. Dong Qian, Dr. Ill Ryu and Dr. Terry Baughn for their comments and suggestions. Acknowledgments are due to students and coworkers in Dr. Lu's group including Dr. Gitogo Churu for his lab mentorship in making samples and Dr. Huiyang Luo for help with split Hopkinson pressure bar test. Also, many thanks go to all my solid mechanics' fellow students in the Department of Mechanical Engineering for their comments and suggestions. The support from AFOSR FA9550-14-1-0227, NSF CMMI-1636306, CMMI-1661246, and ECCS-1307997, and Nashi New Materials, Inc. China is also acknowledged. Also, special thanks go to Covestro LLC (formerly Bayer Corporation U.S.A.) for the generous supply of Desmodur N3300A.

Finally, I am deeply grateful to my parents for their unwavering belief in education and lovely concern all the time. I am also indebted to my love, Nastaran, to whom this dissertation is dedicated, for her love, support and appreciation of my research.

February 2020

# SCALABLE SYNTHESIS AND DYNAMIC MECHANICAL CHARACTERIZATION OF MULTIFUNCTIONAL POLYMER AEROGELS

Sadeq Malakooti, PhD  
The University of Texas at Dallas, 2020

Supervising Professor: Dr. Hongbing Lu

Aerogels are low-density nanoporous solids containing hierarchical three-dimensional networks of nanoparticles pursued primarily for thermal and acoustic insulations and often for functionalization purposes. This work presents scalable sol-gel synthetic routes and characterization of various polymer aerogels including polyurea, poly(isocyanurate–urethane) and polybenzoxazine aerogels.

The first part of this thesis deals with a family of ambient-dried ductile polyurea aerogels with exceptional sound transmission loss characteristics (e.g., over 30 dB within 1 to 4 kHz at bulk density  $0.25 \text{ g/cm}^3$  and 5 mm thickness). This uncommon behavior breaks the empirical “Mass Law” nature of the most conventional acoustic materials. Following an analytical approach using Biot's dynamic theory of poroelasticity, the acoustic properties of the aerogels are modeled and the results are compared with the experimental observations, to construct a design platform for the future aerogel based acoustic thin panels.

In the second part, the fabrication of a family of low-density, ambient-dried and hydrophobic poly(isocyanurate–urethane) aerogels derived from a triisocyanate precursor is reported. Those aerogels are highly-stretchable and have a Poisson's ratio of only 0.22. Under dynamic conditions, their mechanical properties (e.g., mechanical strength) are three orders of magnitude stiffer than their quasi-static results. These scalable and flexible aerogels have great potentials in engineering applications including damping, energy absorption, and substrates for flexible devices.

Lastly, this thesis ends with the synthesis and characterization of ambient-dried polybenzoxazine aerogels as a high-performance polymeric aerogel with strong and robust thermomechanical properties at elevated temperatures. Those aerogels are inherently flame-retardant and superhydrophobic over the entire bulk density range. In addition, they are mechanically strong with strengths (e.g., 1 MPa at  $0.24 \text{ g cm}^{-3}$  at room temperature) higher than those of other high-performance aerogels of similar density, including polyimide and polyamide (Kevlar-like) aerogels as well as polymer cross-linked X-silica and X-vanadia aerogels, at a significantly lower cost which makes them suitable for various industrial applications including high performance structural and thermal protection applications.

## TABLE OF CONTENTS

ACKNOWLEDGMENTS .....	v
ABSTRACT.....	vi
LIST OF TABLES .....	xi
LIST OF FIGURES .....	xii
CHAPTER 1 THE THESIS PHILOSOPHY .....	1
CHAPTER 2 SOUND INSULATION PROPERTIES IN LOW-DENSITY, MECHANICALLY STRONG AND DUCTILE NANOPOROUS POLYUREA AEROGELS .....	4
2.1. Introduction .....	4
2.2. Experimental section .....	7
2.2.1. Material synthesis and characterizations .....	7
2.2.2. Acoustic measurements .....	7
2.3. Theoretical modeling.....	8
2.3.1. Random mass-spring model .....	8
2.3.2. Wave propagation in poroelastic aerogels.....	12
2.3.2.1. Acoustic field equations.....	12
2.3.2.2. Poroelastic model.....	14
2.3.3.3. Boundary conditions .....	18
2.3.2.4. Sound transmission loss .....	19
2.3.2.5. Material parameterization .....	19
2.4. Results and discussion.....	21
2.5. Conclusion.....	29
CHAPTER 3 SOUND TRANSMISSION LOSS ENHANCEMENT IN AN INORGANIC-ORGANIC LAMINATED COMPOSITE PANEL USING MULTIFUNCTIONAL LOW-DENSITY NANOPOROUS POLYUREA AEROGELS .....	30
3.1. Introduction .....	30
3.2. Materials and methods .....	32
3.2.1. Preparation and characterization of PUA aerogels.....	32
3.2.2. Preparation of laminated composites.....	32
3.2.3. Airborne sound transmission loss measurements .....	33

3.3. Analytical modeling .....	34
3.3.1. Acoustic fluid medium .....	35
3.3.2. Isotropic linear elastic medium.....	36
3.3.3. Linear poroelastic medium .....	37
3.3.4. Boundary conditions.....	41
3.3.5. Diffuse sound transmission loss .....	42
3.3.6. Materials parameterization .....	43
3.4. Results and discussion.....	45
3.5. Conclusions .....	53
<b>CHAPTER 4 SCALABLE, HYDROPHOBIC AND HIGHLY-STRETCHABLE POLY(ISOCYANURATE-URETHANE) AEROGELS.....</b>	<b>55</b>
4.1. Introduction .....	55
4.2. Results and discussion.....	57
4.2.1. Synthesis and chemical characterization .....	57
4.2.2. General material properties .....	59
4.2.3. Mechanical characterization .....	63
4.3. Experimental .....	72
4.3.1. Materials .....	72
4.3.2. Synthesis of Poly(isocyanurate-urethane) aerogels.....	72
4.3.3. Methods .....	73
4.3.3.1. Chemical characterization.....	73
4.3.3.2. Physical characterization .....	73
4.3.3.3. Structural characterization .....	74
4.3.3.4. Thermal characterization .....	74
4.3.3.5. Mechanical characterization .....	74
4.4. Conclusions .....	76
<b>CHAPTER 5 LOW-COST, AMBIENT DRIED, SUPERHYDROPHOBIC, HIGH STRENGTH, THERMALLY INSULATING AND THERMALLY RESILIENT POLYBENZOXAZINE AEROGELS.....</b>	<b>77</b>
5.1. Introduction .....	77
5.2. Results and discussion.....	79

5.2.1. Materials synthesis .....	79
5.2.2. Chemical characterization .....	80
5.2.3. Physical characterization .....	83
5.2.3.1. General material properties .....	83
5.2.3.2. Structural properties .....	86
5.2.4. Thermo-mechanical characterization .....	88
5.2.4.1. Quasi-static uniaxial and shear properties at room temperature .....	88
5.2.4.2. Quasi-static compressive properties at elevated temperatures.....	91
5.2.4.3. High-torque dynamic mechanical analysis in shear at elevated temperatures.....	94
5.3. Conclusion.....	97
5.4. Experimental section .....	98
REFERENCES .....	102
BIOGRAPHICAL SKETCH .....	115
CURRICULUM VITAE.....	116

## LIST OF TABLES

Table 2.1. The air properties used in the present calculations .....	20
Table 2.2. The aerogel material parameters used in the present calculations.....	21
Table 3.1. The PUA aerogel material parameters used in the present calculations.....	44
Table 3.2. The gypsum and air material parameters used in the present calculations.....	45
Table 3.3. The STL values and enhancements (STL-E) at different frequencies and the sound transmission classes (STC) of gypsum and gypsum-aerogel composite panels, all in dB, at different sizes.....	49
Table 4.1. The bulk density, porosity, linear shrinkage, recovery speed and glass transition temperature (T <sub>g</sub> ) data of the synthesized aerogel samples. ....	60
Table 4.2. Room temperature quasi-static Young's modulus, Poisson's ratio and speed of wave propagation data of the synthesized aerogel samples. ....	64

## LIST OF FIGURES

Figure 2.1. (a) Schematic of a three-microphone impedance tube for STL measurements; (b) The image of PUA aerogel sample ( $\rho b = 0.1 \text{ g/cm}^3$ ) made in panel form (the test sample cut in a disk shape is shown in the corner).....	8
Figure 2.2. SEM image of a polyurea aerogel at $0.25 \text{ g/cm}^3$ bulk density. ....	9
Figure 2.3. (a) One dimensional multi-DOF mass-spring system; (b) homogenous and (c) random distributions of the normalized spring constants. ....	11
Figure 2.4. Two dimensional wave problem geometry of an infinite poroelastic layer in contact with two semi-infinite fluid mediums impinged by plane harmonic acoustic waves.....	12
Figure 2.5. SEM images of PUA aerogels at different densities: (a) $0.11 \text{ g/cm}^3$ , (b) $0.25 \text{ g/cm}^3$ and (c) $0.45 \text{ g/cm}^3$ . Higher resolution is given in the subset. ....	22
Figure 2.6. Experimental STL values of PUA aerogels in comparison with common commercial porous materials.....	23
Figure 2.7. Vibration transmission loss as a function of frequency for the 60-DOF mass-spring system. ....	24
Figure 2.8. Experimental and theoretical STL values of PUA aerogels at different densities. ....	26
Figure 2.9. Contour plot of STL in dB as a function of frequency and bulk density at constant thickness (5 mm).....	27
Figure 2.10. Contour plot of STL in dB as a function of frequency and thickness at constant bulk density ( $0.25 \text{ g/cm}^3$ ).....	28
Figure 3.1. (a) A view from the connecting window of the ASTM E90 test chamber prepared for a $1 \text{ m}^2$ test specimen; (b) $1 \text{ m}^2$ test sample installation with using sample frame holders in compliance with ASTM E90; (c) A view from an aerogel panel sprayed with green glue before bonding to the another layer; (d) A schematic for the final configuration of the composite sample including two gypsum skin layers (shown in yellow color) accompanied with two core aerogel layers (shown in white color); (e) $10 \text{ m}^2$ composite sample preparation by consolidating several smaller aerogel samples using double sided tapes and green glue; (f) A view from a $10 \text{ m}^2$ aerogel layer.....	34
Figure 3.2. Schematic diagram for the laminated composite lay-up and sound transmission problem model. ....	35

Figure 3.3. (a) and (c) The SEM images of the PUA aerogels at bulk densities 0.15 g/cm <sup>3</sup> and 0.25 g/cm <sup>3</sup> , respectively; (b) and (d) The fiber diameter size distributions of the PUA aerogel networks at bulk densities 0.15 g/cm <sup>3</sup> and 0.25 g/cm <sup>3</sup> , respectively.....	46
Figure 3.4. The effect of PUA aerogels on the airborne STL values of 1 m <sup>2</sup> samples as a function of frequency. ....	48
Figure 3.5. The effect of PUA aerogels on the airborne STL values of 10 m <sup>2</sup> samples as a function of frequency. ....	50
Figure 3.6. The comparison between the plane strain theoretical solution with experimental airborne STL values of gypsum-aerogel composite samples as a function of frequency at different sizes.....	51
Figure 3.7. Airborne STL of an unbounded aerogel-gypsum layered composite as a function of frequency at different average core bulk densities (the ratio of the two aerogel bulk densities was kept to 1.5). ....	53
Figure 4.1. (a) Synthetic protocol of the PU aerogels; (b) Reaction pathway to isocyanurate cross-linking urethane aerogels. ....	58
Figure 4.2. Typical solid-state CPMAS <sup>13</sup> C NMR spectrum of the aerogel.....	59
Figure 4.3. Typical flexible PU aerogel panel at (a) original, (b) deformed and (c) final shapes at bulk density 0.28 g/cm <sup>3</sup> ; (d) and (e) SEM images of the PU aerogels at bulk densities 0.28 g/cm <sup>3</sup> and 0.37 g/cm <sup>3</sup> , respectively; (f) Water drop contact angles on the surface of the PU aerogel at bulk density 0.28 g/cm <sup>3</sup> .....	62
Figure 4.4. (a) Differential scanning calorimetry and (b) Thermogravimetric analysis of PU aerogels at bulk densities 0.28 g/cm <sup>3</sup> (solid line) and 0.37 g/cm <sup>3</sup> (dash line). ....	63
Figure 4.5. (a) Typical quasi-static uniaxial tensile stress-strain responses of PU aerogels at different bulk densities; (b) Power-law relationship of Young's modulus with bulk density of the PU aerogels ; (c) and (d) Cyclic quasi-static load-unload compression testing at 50% strain of PU aerogels at bulk densities 0.28 and 0.37 g/cm <sup>3</sup> , respectively; (e) Maximum stress and (f) Normalized absorption energy during 10 consecutive cycles for PU aerogels at bulk densities 0.28 and 0.37 g/cm <sup>3</sup> . ....	66
Figure 4.6. Quasi-static load–unload-reload compression testing of PU aerogels at bulk densities of 0.28 and 0.37 g/cm <sup>3</sup> . ....	68
Figure 4.7. Dynamic mechanical analysis in compression mode (a: storage modulus, b: loss modulus, and c: tan delta) of PU aerogels at bulk densities 0.28 (dash line) and 0.37 (solid line) g/cm <sup>3</sup> at different temperatures and frequencies. ....	70

Figure 4.8. Room temperature compressive behavior of PU aerogels at bulk densities 0.28 (dash line) and 0.37 (solid line) g/cm <sup>3</sup> at high strain rates.....	72
Figure 5.1. (a) The chemical synthesis of the benzoxazine (BO) monomer, and (b) The synthetic protocol of the ambient-dried polybenzoxazine (PBO) aerogels.....	80
Figure 5.2. Infrared (FTIR) spectra of the BO monomer and of representative PBO-10 aerogel sample. ....	81
Figure 5.3. Solid-state CPMAS <sup>13</sup> C NMR spectra of the BO monomer and of representative PBO-10 aerogel sample. ....	82
Figure 5.4. N <sub>2</sub> -sorption measurements of the PBO aerogels; (a) Isotherm and (b) BJH plots. ....	85
Figure 5.5. SEM micrographs at two magnifications of the PBO aerogels and the water drop (5 mL) average contact angles on the smooth and sanded PBO-xx aerogel surfaces, pointing to a superhydrophobic state. ....	87
Figure 5.6. (a) Typical quasi-static uniaxial compression stress–strain responses of the PBO aerogels at different bulk densities; (b) Power–law relationships of the Young's modulus and the yield strength with bulk density of the PBO aerogels along with those values for X-silica, X-vanadia, polyimide, and polyamide (Kevlar-like) aerogels at the same density range; (c) Cyclic quasi-static load–unload compression testing at -20% strain of PBO-10 for 100 cycles; (d) Apparent Young's modulus (top) and peak stress (bottom) values of the PBO-10 at different cycles; (e) Sequential cyclic load–unload-reload compression testing of the PBO-12 sample; and (f) Quasi-static pure torsion testing of intact and preloaded PBO-12 samples. All experiments have been carried out at room temperature. Insets in (a) and (f) are the typical PBO samples before and after quasi-static compression and pure torsion tests, respectively. ....	89
Figure 5.7. The quasi-static compressive properties of PBO aerogels at elevated temperatures: (a) Young's modulus; (b) Compressive strength; and (c) Rupture strain level. (d) The effect of thermal soaking time on the compressive stress-strain behavior of PBO-10 sample. And (e) Infrared images of PBO-7 sample (23 mm length and 7.6 mm diameter) on a heating stage for 10 min time interval. ....	94
Figure 5.8. Shear viscoelastic properties of PBO-12 sample as a function of frequencies at different temperature: (a) Storage modulus; (b) Master curve for storage modulus and the storage shift factor at different temperature in the inset; (c) Loss modulus; and (d) tanδ. ....	96
Figure 5.9. Isofrequency shear complex modulus and tanδ of PBO-12 as a function of temperature at reference frequency of 1 Hz. ....	97

## CHAPTER 1

### THE THESIS PHILOSOPHY

*Aerogels* are characterized as quasi-stable, low-density, high specific surface area and nanoporous three-dimensional assemblies of nanoparticles. First invented by Kistler in 1931 [1], conventional aerogels were associated with silica and were produced by drying wet silica gels by converting their pore filling liquid into a supercritical fluid [2]. Owing to their extremely low thermal conductivity, silica aerogels have been implemented successfully in thermal insulation applications [3]. However, silica aerogels are extremely fragile and unsuitable for handling as required by most engineering applications. This limitation has been addressed by introducing polymer cross-linked silica aerogels (known as X-Aerogels), whereas a nano-thin polymer coating covered conformally the entire skeletal framework of conventional silica aerogels. The density increased by only a factor of 2-3 (still very lightweight materials) but the ultimate strength increased by a factor of 300 [4]. Subsequently, it was reasoned that since the exceptional mechanical strength of X-aerogels was attributed to the polymer coating, purely polymeric aerogels with the same nanostructure and interparticle connectivity of X-aerogels would have similar mechanical properties. That hypothesis has been confirmed with purely polymeric aerogels from all major polymeric classes such as polyureas [5], polyurethanes [6], polyimides [7] and polyamides (Kevlar<sup>TM</sup>-like) [8]. Indeed, new applications that were previously unrelated to aerogels, as in ballistic protection (armor), have now become feasible [9].

Over the past decades, the mechanical properties of silica aerogels and X-aerogels have been exhaustively studied, e.g., [9]. On the other hand, limited attempts have been made to systematically study the mechanical properties of organic aerogels at different mechanical loading conditions (one can check [10,11]). The primary thrust of this research is to focus on this gap. In this thesis, I aim to focus on the mechanics of different organic aerogels such as polyurea, poly(isocyanurate-urethane), and polybenzoxazine aerogels, in specific, at different loading and environmental conditions to elucidate the coupled dynamic behavior of the organic aerogel nanoparticle network with the pore liquid at different contexts including acoustic wave interactions with aerogels.

The first part of this research is focused on the polyurea (PUA) aerogels. Primary acoustic measurements have been shown a remarkable sound transmission loss behavior for these materials. The normal incidence sound transmission loss for the low-density PUA aerogels was reported in the 20-40 dB range, in contrast with traditional sound insulation materials, such as polyurethane foam, which can only reach up to 5 dB only [12]. This uncommon behavior has been repeated for the PUA aerogels at a laminated composite configuration with gypsum wallboards in a diffuse sound field-based sound transmission loss measurement [13]. These experimental results show that the PUA aerogels break the empirical "Mass Law" nature of conventional acoustic materials. According to the mass law, the mean sound transmission loss of a single-layer conventional material increases at an approximately constant rate of 6 dB by doubling the mass per unit area due to the increasing forces of inertia. On the PUA aerogel, my main problem of interest is to seek and construct a predictable and quantitative framework to interpret the PUA aerogel's acoustic behavior. Such a framework is required for the material design and optimization of future aerogel-based structures.

The second part of this research focuses on the poly(isocyanurate-urethane) aerogels (PU aerogels). In contrast with PUA aerogel where only the acoustic properties were studied, at this part, fundamental and advanced mechanical characterizations such as quasi-static and high strain rate mechanical tests have taken into account for the PU aerogels. Through a sol-gel synthesis, using inexpensive multifunctional small-molecule monomers, the PU aerogels were synthesized [14]. The rigidity and flexibility of the samples were controlled by the monomer concentration. The aerogels exhibit a highly stretchable behavior with a rapid increase in Young's modulus with bulk density (slope of log-log plot  $> 6.0$ ). In addition, the aerogels are very compressible (more than 80% compressive strain) with a high shape recovery rate (more than 80% recovery in 30 s). Under tension even at high strains (e.g., more than 100% tensile strain), the aerogels at lower densities do not display a significant lateral contraction and have a Poisson's ratio of only 0.22. Under dynamic conditions, the properties (e.g., complex moduli and dynamic stress-strain curves) are highly frequency- and rate-dependent, particularly in the Hopkinson pressure bar experiment where in comparison with quasi-static compression results, the properties such as mechanical strength were three orders of magnitude stiffer.

Finally, in the last chapter, I studied the mechanical properties of ambient-dried polybenzoxazine aerogels at elevated temperatures [15]. Those materials are inherently flame-retardant and superhydrophobic over the entire bulk density range (0.24–0.46 g cm<sup>-3</sup>). In addition, they are mechanically strong with strengths (e.g., 1 MPa at 0.24 g cm<sup>-3</sup> at room temperature) higher than those of other high-performance aerogels of similar density, including polyimide and polyamide (Kevlar-like) aerogels as well as polymer cross-linked X-silica and X-vanadia aerogels, at a significantly lower cost.

## CHAPTER 2

# SOUND INSULATION PROPERTIES IN LOW-DENSITY, MECHANICALLY STRONG AND DUCTILE NANOPOROUS POLYUREA AEROGELS

Aerogels are quasi-stable, nanoporous, low-density, three-dimensional assemblies of nanoparticles. In this chapter, an extremely high sound transmission loss for a family of ductile polyurea aerogels (e.g., over 30 dB within 1 to 4 kHz at bulk density  $0.25 \text{ g/cm}^3$  and 5 mm thickness) is reported. The fundamental mechanisms behind the aerogel acoustic attenuations are investigated. Sharing striking similarities with acoustic metamaterials, initially, aerogels are studied via a one-dimensional multi degree-of-freedom mass-spring system. Different effects such as spring constant disparity are investigated in regard to the structural vibration wave transmission loss. Results are given for different configurations consistent with the aerogel nano/microstructures. A significant wave attenuation is observed by considering a random spring distribution. In the next step towards modeling such a complex hierarchical and random structural material, the continuum Biot's dynamic theory of poroelasticity is implemented to analyze the experimental sound transmission loss results. In this framework, a two-dimensional plane strain analysis is considered for the interaction of a steady-state time-harmonic plane acoustic wave with an infinite aerogel layer immersed in and saturated with air. The effects of bulk density and thickness on the aerogel sound transmission loss are elucidated. By comparing the theoretical results with the experimental observations, this study develops a qualitative/quantitative basis for the dynamics of the aerogel nanoparticle network as well as the airflow and solid vibroacoustic interactions. This basis provides a better understanding of the overall acoustic properties of the aerogels that might also be helpful in the design of the future hierarchical materials.

### 2.1. Introduction

For decades if not longer, the quest for light-weight, sound insulating materials has been a central interest of the engineering acoustics community. The challenge primarily originated from the insufficient acoustical performance of the traditional bulky materials, specifically in the low-frequency range, which is more important in speech comprehension [16]. Empirically, at the low-

frequency range, the mean sound transmission loss of a single-layer conventional material increases at an approximately constant rate of 6 dB by doubling the mass per unit area due to the increasing forces of inertia. This phenomenon is referred to as “The Mass Law”[17]. As a result, the current lightweight materials (e.g., acoustical foams) are not able to solely address the realistic engineering demands and therefore had to be employed in appropriately designed multilayered structures, which are not always an efficient engineering solution due to either thick panels or heavy structures.

In contrast with traditional acoustic materials, aerogels are quasi-stable, low-density 3D assemblies of nanoparticles which are primarily pursued for thermal insulations and often nanoporous hosts of functional guests. Aerogels are typically derived from drying wet-gels by turning the pore-filling solvent into a supercritical fluid. Traditional aerogels are mainly based on silica. Interestingly, the experimental and theoretical results on the sound-absorbing properties of the silica aerogel structures have revealed a huge improvement compared with their commercial counterparts [18]. But, in spite of their very attractive attributes, the application of the silica aerogels have been mostly confined to space exploration due to their structural fragility. The other major limiting factor is the production cost of aerogels, mainly due to the supercritical drying which even limits the size of the final product. To overcome those problems, a new class of aerogels has recently emerged using major polymeric sources, like polyurea.

Polyurea (PUA) aerogels were first reported by De Vos-Biesmans in a 1996 U.S. Patent [19]. Due to the environmental impact concerns, Leventis et al. proposed an alternative synthesis for PUA aerogels by replacing expensive amines with water [5]. Recently, using this approach, we discovered extremely high acoustic attenuation properties in a family of purely organic aerogels, including not only PUA aerogels, but also polydicyclopentadiene (pDCPD) aerogels as well [20]. The acoustic attenuation that was reached was in the 20-40 dB range, in contrast to traditional sound insulation materials, such as polyurethane foam, which can only reach up to 5 dB only. Thereby, the main motivation of this work was to study the sound transmission loss (STL) behavior of this family of purely organic aerogels, specifically on PUA aerogels, in pursuit of a better understanding on their main acoustic insulating mechanisms.

In order to make a material with higher sound transmission loss, sound reflection and/or sound energy absorption should be improved. In the aerogel case, the material is highly porous and therefore the sound energy absorption property is more important to consider as the incident sound pressure wave can penetrate into the material. The sound energy is partly converted into heat within a porous medium via a huge number of internal reflections with the solid network. Meantime, the dimensionless Knudsen number ( $Kn$ ) can characterize the airflow regime in a porous medium,  $Kn = \lambda / \Gamma$ , where  $\lambda$  is the mean free path of air molecule (m) and  $\Gamma$  is the characteristic length of the porous medium (m). The characteristic length can be approximated as the average pore size of the porous material. In most aerogels the average pore size is on the order of 2 to 50 nm, i.e., on the same order of magnitude with the air molecules mean free path. In this picture, the Knudsen number becomes close to 1 meaning that both viscous and molecular flows are dominant in the airflow thus facilitating the wave energy dissipation in air-saturated aerogel materials. On the other hand, solid-phase sound energy dissipation features can be characterized by their dynamic mechanical properties. Bulk polyurea has been used commercially for more than a decade and is well known as a highly viscoelastic material with strong frequency dependency [21]. Its time-dependent properties have been favorably emphasized in different applications, such as blast mitigating coatings and acoustic dampening.

However, from a different perspective, our aerogels have striking similarities with certain acoustic metamaterials, but their nanostructures are orders of magnitude smaller than those of the latter. Within this framework, the central hypothesis of this work that porous nanostructured materials with multiscale, random, heterogeneous structural elements and porosities would provide highly tortuous paths and synergistic dynamic mechanisms for broadband acoustic attenuation. Using a finite one dimensional (1D) mass-spring model, Jensen has shown that the disparity in spring constants can introduce a phononic bandgap in a periodic structure [22]. This is a very promising basis for understanding the physics behind the STL characteristics of aerogels.

In this work, the normal incidence STL of the light-weight eco-friendly synthesized PUA aerogels at different densities are measured and studied using a modified impedance tube technique. In order to study the sound wave propagation in the aerogels, two different modeling perspectives are considered. First, the aerogels are modeled with a conceptual linear monoatomic random mass-

spring system in which the identical masses are connected by varying linear elastic springs. Understanding the wave propagation in those 1D structures can shed light on exploring the fundamental mechanisms behind the acoustic attenuation of aerogels. Second, taking advantage of the continuum Biot's dynamic theory of poroelasticity, a quantitative framework on the sound insulating properties of the aerogels is provided to compare them with the experimental normal incidence STL values. The theoretical results and the experimental observations generate a qualitative/quantitative basis for the understanding of the effects of the nanoparticle solid network and its interaction with airflow on the overall acoustic properties of aerogels.

## 2.2. Experimental section

### 2.2.1. Material synthesis and characterizations

The PUA aerogels of this study were synthesized according to procedures developed and published by the co-authors previously [5]. PUA aerogels at different densities, porosities and morphologies were synthesized by varying the monomer concentration. Bulk densities ( $\rho_b$ ) were determined from the weight and the physical dimensions of the samples. Skeletal densities ( $\rho_s$ ) at different bulk density were previously measured and owing to the low variations, here we use the average reported value ( $1.24 \text{ g/cm}^3$ ) [5]. Porosities,  $h$ , were determined from  $\rho_b$  and  $\rho_s$  according to  $h = 100 \times [(\rho_s - \rho_b) / \rho_s]$ . SEM micrographs were obtained from Au-coated samples on a Hitachi model S-4700 field emission microscope.

### 2.2.2. Acoustic measurements

The normal incidence STL is the quantity of interest in this research. In order to increase the sensitivity of the standard impedance tube measurement, the three-microphone impedance tube methodology developed by Salissou et al. [23] was implemented here. For geometrically symmetrical specimens, as with our aerogel disks, the measurement technique is reduced to three-microphone one-load method with rigid backing, simplifying the measurement and increasing accuracy. Accordingly in this method, referring to Figure 2.1a, the test specimen (i.e., material) is mounted at one end of a long, narrow tube, with an acoustic source placed at the opposite end. In addition to two microphones (Mic 1 and 2) in the tube wall upstream, a third microphone (Mic 3)

is located in the downstream in a rigid termination directly behind the test sample (see Figure 2.1a). The characteristic impedance of the test sample can be determined by measuring the normal-incidence complex reflection coefficient of the material.

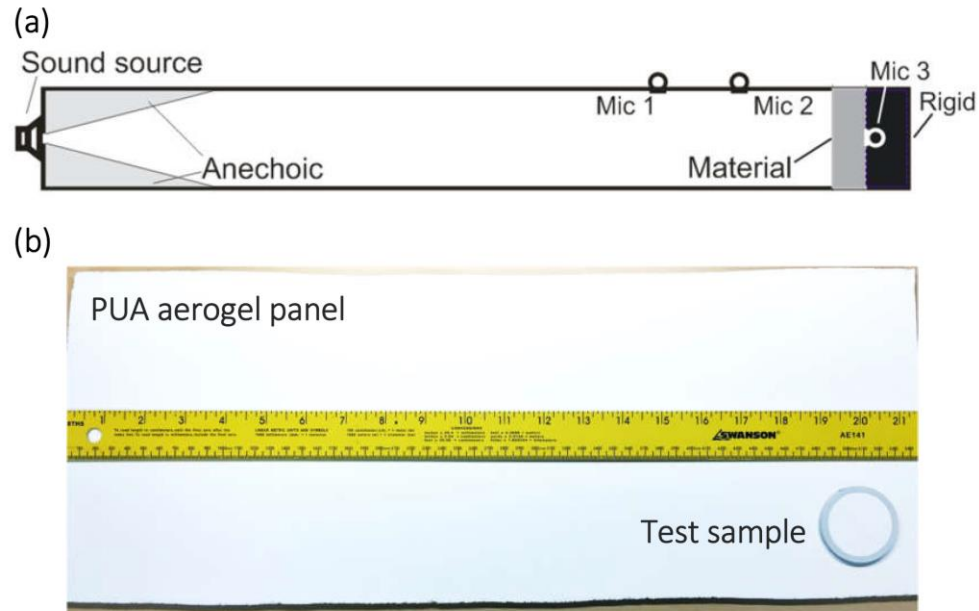


Figure 2.1. (a) Schematic of a three-microphone impedance tube for STL measurements; (b) The image of PUA aerogel sample ( $\rho_b = 0.1 \text{ g/cm}^3$ ) made in panel form (the test sample cut in a disk shape is shown in the corner).

For these measurements, the PUA aerogels are cut in a disk shape (thickness 5 mm and diameter 4 cm) fitted inside the sample holder (a PVC ring, see Figure 2.1b). The impedance tube can measure the acoustical properties within a range of frequencies 1 to 4 kHz.

## 2.3. Theoretical modeling

### 2.3.1. Random mass-spring model

The structural dynamics of aerogels inherently includes a high level of complexity and randomness due to the aerogel amorphous and hierarchical structure. Figure 2.2 shows such a candidate, whereas  $2 \mu\text{m}$  polyurea particles are connected by a nanofibrous polyurea web, forming a highly random and complex spring-mass system. The random structures can be efficiently abstracted with a lower-dimensional model with some random structural parameters.

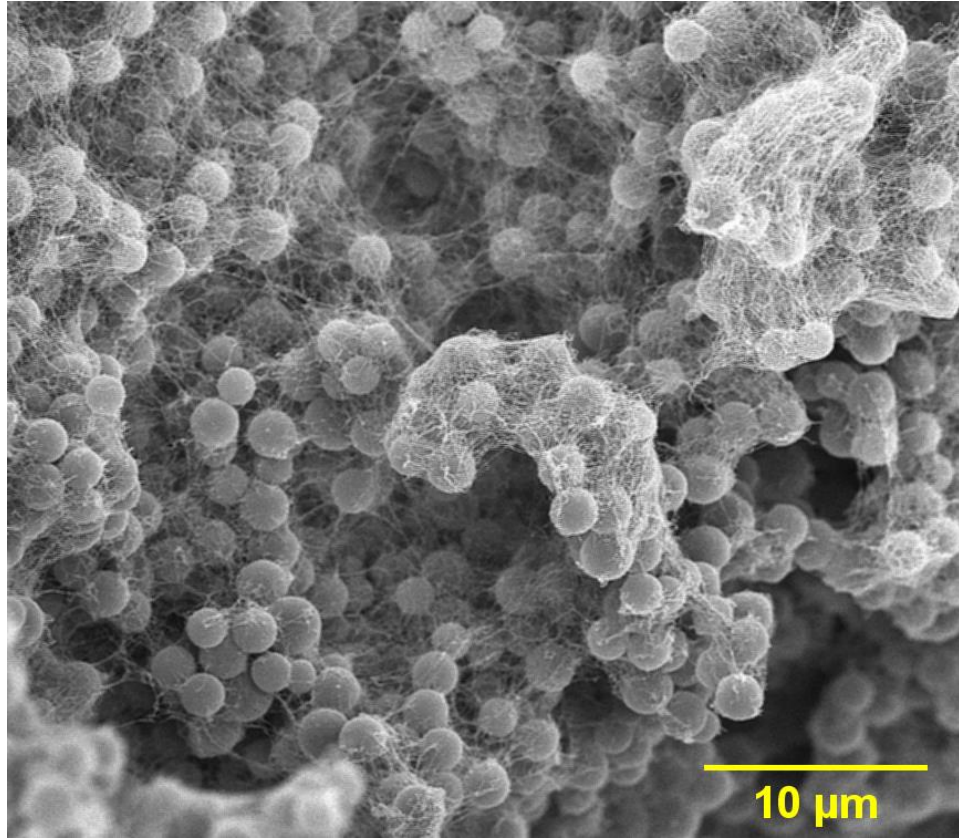


Figure 2.2. SEM image of a polyurea aerogel at  $0.25 \text{ g/cm}^3$  bulk density.

For the sake of simplicity, the aerogels are modeled with a 1D mass-spring system as shown in Figure 2.3a. The forced vibration of the system when a time-harmonic mechanical force with frequency  $\omega$  subjected to the left end is analyzed in order to calculate the displacement at the other end mass. The displacement amplitudes can be readily formulated using standard forced vibration analysis. The transmission loss ( $TL$ ) is then simply introduced as:

$$TL = 20 \log_{10} \left( \frac{X_n}{X_1} \right), \quad (2.1)$$

where  $X_1$  and  $X_n$  are the displacements for the first left mass and the last right mass respectively. The number of degree of freedom (DOF) is denoted here by  $n$ . In the particular case of a 2-DOF system, the transmission loss can be written as:

$$TL = 20 \log_{10} \left( \frac{\beta_1}{\beta_1 + \beta_2 - m\omega^2} \right), \quad (2.2)$$

where  $\beta_1$  and  $\beta_2$  are the spring constants, and  $m$  is the mass. Here, a 60-DOF system is considered. The value of the masses is set to  $4.02 \times 10^{-14}$  kg which is the mass of a solid polyurea particle with a 2  $\mu\text{m}$  radius. Two situations are taken into account. First, a homogenous system where all the spring constants are set equal to each other (i.e.,  $\beta = 7.8 \times 10^{-4}$  N/m), and second, a non-homogenous system with a Gaussian random distribution for the spring constants. Figures 3b and 3c show the spring constant history of the homogenous and random arrangements. Using the given material properties, the structural vibration transmission loss calculated by Eq. (2.1) can be analyzed.

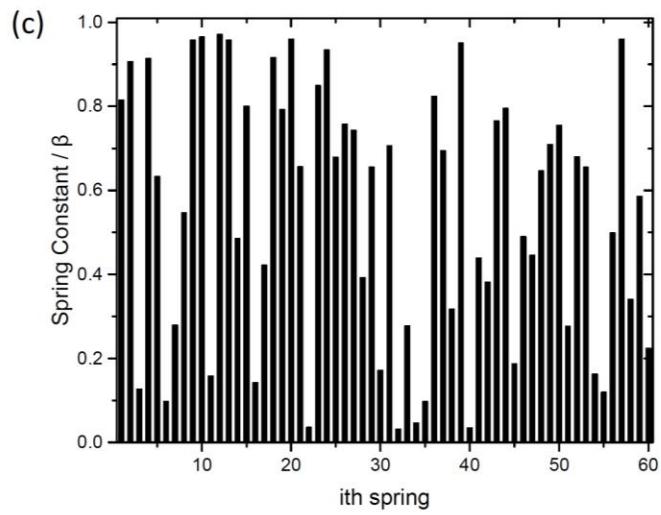
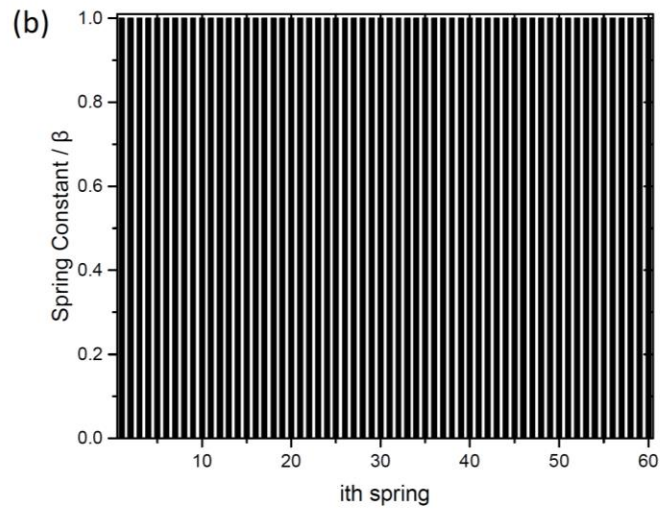
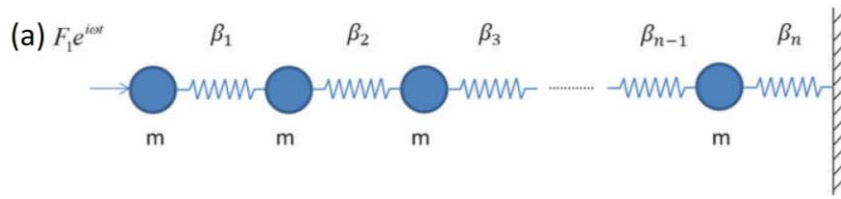


Figure 2.3. (a) One dimensional multi-DOF mass-spring system; (b) homogenous and (c) random distributions of the normalized spring constants.

### 2.3.2. Wave propagation in poroelastic aerogels

In order to consider the effects of airflow and fluid-solid structural interactions on the wave propagation properties of aerogels, a different approach from the discrete mass-spring aerogel model is required. In this research, following the standard techniques of acoustics wave propagation and the Biot's dynamic poroelasticity theory, the wave propagation properties of the porous organic aerogels are modeled and studied. The formulations and the implemented methodology are summarized below.

#### 2.3.2.1. Acoustic field equations

The Cartesian coordinate system,  $\{o; x, y, z\}$ , used in this work is shown in Figure 2.4. A plate is infinite in the  $xz$ -plane and submerged in an unbounded acoustic medium, and the  $y$  axis is normal to the plate boundary. An incident time-harmonic plane acoustic wave at an angle  $\theta$  with respect to the normal of the plate is impinging to the plate.

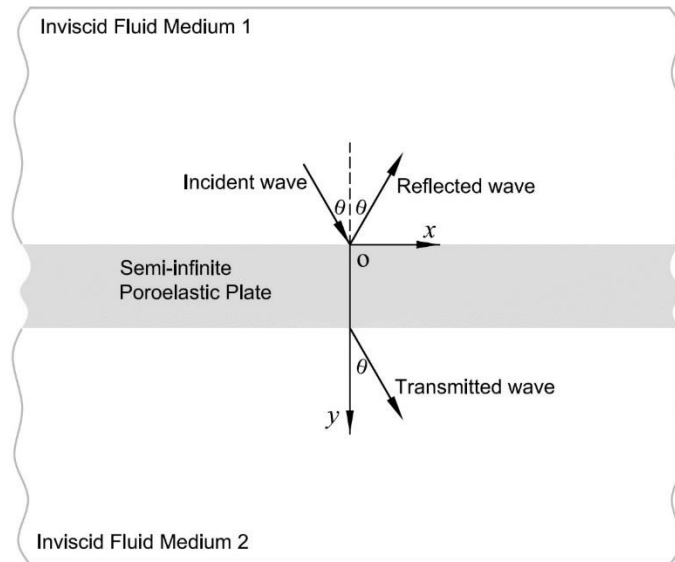


Figure 2.4. Two-dimensional wave problem geometry of an infinite poroelastic layer in contact with two semi-infinite fluid mediums impinged by plane harmonic acoustic waves.

The field equations for an inviscid ideal compressible fluid medium may be simply expressed in terms of a scalar velocity potential as [17]

$$\mathbf{v} = -\nabla \phi, \quad (2.3a)$$

$$p = \rho_0 \dot{\phi}, \quad (2.3b)$$

where  $\rho_0$  is the fluid density,  $\mathbf{v}$  is the fluid particle velocity vector,  $p$  is the acoustic pressure and  $\nabla$  is the gradient operator. The scalar velocity potential satisfies the classical wave equation [17],

$$\nabla^2 \phi = \frac{1}{c_0^2} \frac{\partial^2 \phi}{\partial t^2}, \quad (2.4)$$

in which  $c_0$  is the speed of sound in a fluid medium, and  $\nabla^2 = \partial^2/\partial x^2 + \partial^2/\partial y^2$  is the Laplacian. The normalized harmonic solution of Eq. (2.4) with respect to the incident wave amplitude in the upper and lower fluid mediums may respectively be written as [24],

$$\phi_1 = e^{-ik_x x} \left( e^{-ik_y y} + I_R e^{ik_y y} \right), \quad (2.5a)$$

$$\phi_2 = I_T e^{-i(k_x x + k_y y)}, \quad (2.5b)$$

where  $k_x = k \sin \theta$  and  $k_y = k \cos \theta$  are the wavenumbers in  $x$  and  $y$  directions,  $k = \omega / c_0$  is the acoustic wavenumber,  $I_R$  and  $I_T$  are the amplitudes of the reflected and transmitted waves respectively. Here we have assumed harmonic time variations throughout with the  $e^{i\omega t}$  dependence suppressed for simplicity.

Using the field equations in Eq. (2.3), the normal fluid velocity and the acoustic pressure in the upper and lower fluid mediums can be expressed as follows [24]:

$$v_{y1} = -\partial \phi_1 / \partial y = -i k_y e^{-ik_x x} \left( -e^{-ik_y y} + I_R e^{ik_y y} \right), \quad (2.6a)$$

$$v_{y2} = -\partial \phi_2 / \partial y = i k_y I_T e^{-i(k_x x + k_y y)}, \quad (2.6b)$$

and

$$p_1 = i\omega\rho_0\phi_1 = i\omega\rho_0 e^{-ik_x x} \left( e^{-ik_y y} + I_R e^{ik_y y} \right), \quad (2.7a)$$

$$p_2 = i\omega\rho_0\phi_2 = i\omega\rho_0 I_T e^{-i(k_x x + k_y y)}, \quad (2.7b)$$

where  $v_{y1}$  and  $v_{y2}$  are the normal fluid velocities and  $p_1$  and  $p_2$  are the acoustic pressures in the fluid mediums 1 (upper) and 2 (lower) respectively.

### 2.3.2.2. Poroelastic model

The presented theoretical model is based on Biot's dynamic theory of poroelasticity [29, 30] which is an efficient two-phase modeling method that can address several important physical properties such as wave speed, attenuation, and dispersion. Here the aerogel material is considered as an air-filled porous structure with comparable fluid and solid densities. This theory can formulate the appropriate constitutive equations and equations of motion for the poroelastic media and thus can predict the existence of two types of dilatational (compressional) waves along with one rotational (shear) wave in the coupled fluid-solid network. The theory is summarized below.

The Biot's stress-strain relationship between the fluid and solid strains and applied stress on the solid ( $\sigma_{ij}$ ) is written as [25]:

$$\sigma_{ij} = (Ae + Q\varepsilon)\delta_{ij} + 2Ne_{ij}, \quad (2.8)$$

where  $e = \nabla \cdot \mathbf{u}$  and  $\varepsilon = \nabla \cdot \mathbf{U}$  are the solid and fluid volumetric strains respectively,  $\mathbf{u}$  and  $\mathbf{U}$  are the vector solid and fluid displacement fields respectively,  $e_{ij} = (u_{i,j} + u_{j,i})/2$ , is the solid strain components,  $N = E_1/2(1+\nu)$ , is the solid bulk in-vacuo shear modulus,  $E_1$  is the solid bulk in-vacuo Young's modulus,  $\nu$  is the Poisson's ratio,  $A = \nu E_1 / (1+\nu)(1-2\nu)$ , is the Lamé constant of the solid phase,  $Q = (1-h)E_2$ , is the coupling between fluid and solid phases,  $h$  is material porosity and  $E_2$  is the bulk modulus of elasticity for the fluid in the pores. The mean pore fluid pressure ( $s$ ) can be also written as [25]:

$$s = R\varepsilon + Qe, \quad (2.9)$$

where  $R$  here is assumed to be  $hE_2$ . For air-filled cylindrical pores,  $E_2$  can be written in terms of air bulk modulus as [33, 34]:

$$E_2 = E_0 \left[ 1 + \frac{2(\gamma-1)J_1(\text{Pr}^{1/2} \lambda_c \sqrt{-i})}{\text{Pr}^{1/2} \lambda_c \sqrt{-i} J_0(\text{Pr}^{1/2} \lambda_c \sqrt{-i})} \right]^{-1}, \quad (2.10)$$

where  $E_0 = \rho_0 c_0^2$ ,  $\gamma$  is the ratio of specific heats,  $\text{Pr}$  is the Prandtl number,  $\lambda_c^2 = \frac{8\omega\rho_0\varepsilon'}{h\sigma}$ ,  $J_0$  and  $J_1$  are the first kind Bessel functions of zero and first orders respectively. Also  $\varepsilon'$  is the geometrical structure factor and  $\sigma$  is the steady-state macroscopic flow resistivity.

Following the standard methods of continuum mechanics, the equations of motion (linear momentum balance) governing the solid and interstitial fluid displacements under harmonic excitation can be written as [25],

$$N\nabla^2 \mathbf{u} + \nabla[(A+N)e + Q\varepsilon] = -\omega^2 (\rho_{11}^* \mathbf{u} + \rho_{12}^* \mathbf{U}) \quad (2.11a)$$

$$\nabla[Qe + R\varepsilon] = -\omega^2 (\rho_{12}^* \mathbf{u} + \rho_{22}^* \mathbf{U}) \quad (2.11b)$$

in which the effective complex mass coefficients ( $\rho_{11}^*$ ,  $\rho_{12}^*$  and  $\rho_{22}^*$ ) which are associated with the viscous energy dissipation in the porous material due to the relative motion between the phases are written as [25]:

$$\rho_{11}^* = \rho_1 + \rho_a + b/i\omega, \quad (2.12a)$$

$$\rho_{12}^* = -\rho_a - b/i\omega, \quad (2.12b)$$

$$\rho_{22}^* = \rho_2 + \rho_a + b/i\omega, \quad (2.12c)$$

where  $b$  is a viscous coupling factor related to the macroscopic flow resistivity of the porous material,  $\rho_1$  and  $\rho_2 = h\rho_0$  are the bulk densities of the solid and fluid phases respectively and  $\rho_a = \rho_2(\varepsilon' - 1)$  is the inertial coupling parameter between the fluid and solid phases. For

cylindrical pores, the coefficient  $b$  can be expressed as  $b = i\omega\varepsilon'\rho_2\left(\frac{\rho_c^*}{\rho_0} - 1\right)$  in which  $\rho_c^*$  can be defined as [26]:

$$\rho_c^* = \rho_0 \left[ 1 - \frac{2J_1(\lambda_c \sqrt{-i})}{\lambda_c \sqrt{-i} J_0(\lambda_c \sqrt{-i})} \right]^{-1}. \quad (2.13)$$

For an isotropic porous material, from the equations of motion, Eq. (2.11), one can derive a fourth-order wave equation for dilatational waves in the solid phase as [27]:

$$\nabla^4 e + A_1 \nabla^2 e + A_2 e = 0, \quad (2.14)$$

where  $A_1 = \omega^2 (\rho_{11}^* R - 2\rho_{12}^* Q + \rho_{22}^* P) / (PR - Q^2)$ ,  $A_2 = \omega^4 (\rho_{11}^* \rho_{22}^* - \rho_{12}^{*2}) / (PR - Q^2)$  and  $P = A + 2N$ . Equation 14 has two plane harmonic solutions associated with the two dilatational waves with the wavenumbers given by  $k_{1,2}^2 = (A_1 \pm \sqrt{A_1^2 - 4A_2}) / 2$ , [27]. Furthermore, the governing wave equation for the rotational wave in the solid can be written as [27]:

$$\nabla^2 \boldsymbol{\omega} + k_r^2 \boldsymbol{\omega} = 0, \quad (2.15)$$

where  $\boldsymbol{\omega} = \nabla \times \mathbf{u}$  is the solid rotational strain and  $k_r^2 = (\omega^2 / N) / (\rho_{11}^* - \rho_{12}^{*2} / \rho_{22}^*)$ . The volumetric and rotational strains of the fluid phase can be expressed as [27]:

$$\varepsilon = \nabla \cdot \mathbf{U} = \frac{(PR - Q^2) \nabla^2 e + \omega^2 (\rho_{11}^* R - \rho_{12}^* Q) e}{\omega^2 (\rho_{22}^* Q - \rho_{12}^* R)}, \quad (2.16a)$$

$$\boldsymbol{\Omega} = \nabla \times \mathbf{U} = -\frac{\rho_{12}^*}{\rho_{22}^*} \boldsymbol{\omega}. \quad (2.16b)$$

By solving wave equations, Eqs. (2.14) and (15), and subsequently Eq. (2.16), volumetric and rotational strain fields in fluid and solid phases can be obtained. Boltan et al. have previously shown the plane strain displacement fields for the solid and fluid phases as [27]:

$$\begin{aligned}
u_x = ik_x e^{-ik_x x} & \left[ \frac{C_1}{k_1^2} e^{-ik_{1y} y} + \frac{C_2}{k_1^2} e^{ik_{1y} y} + \frac{C_3}{k_2^2} e^{-ik_{2y} y} + \frac{C_4}{k_2^2} e^{ik_{2y} y} \right] \\
& - i \frac{k_{ty}}{k_t^2} e^{-ik_x x} \left( C_5 e^{-ik_{ty} y} - C_6 e^{ik_{ty} y} \right),
\end{aligned} \tag{2.17a}$$

$$\begin{aligned}
u_y = ie^{-ik_x x} & \left[ \frac{k_{1y}}{k_1^2} C_1 e^{-ik_{1y} y} - \frac{k_{1y}}{k_1^2} C_2 e^{ik_{1y} y} + \frac{k_{2y}}{k_2^2} C_3 e^{-ik_{2y} y} - \frac{k_{2y}}{k_2^2} C_4 e^{ik_{2y} y} \right] \\
& + i \frac{k_x}{k_t^2} e^{-ik_x x} \left( C_5 e^{-ik_{ty} y} + C_6 e^{ik_{ty} y} \right),
\end{aligned} \tag{2.17b}$$

$$\begin{aligned}
U_x = ik_x e^{-ik_x x} & \left[ b_1 \frac{C_1}{k_1^2} e^{-ik_{1y} y} + b_1 \frac{C_2}{k_1^2} e^{ik_{1y} y} + b_2 \frac{C_3}{k_2^2} e^{-ik_{2y} y} + b_2 \frac{C_4}{k_2^2} e^{ik_{2y} y} \right] \\
& - ig \frac{k_{ty}}{k_t^2} e^{-ik_x x} \left( C_5 e^{-ik_{ty} y} - C_6 e^{ik_{ty} y} \right),
\end{aligned} \tag{2.17c}$$

$$\begin{aligned}
U_y = ie^{-ik_x x} & \left[ b_1 \frac{k_{1y}}{k_1^2} C_1 e^{-ik_{1y} y} - b_1 \frac{k_{1y}}{k_1^2} C_2 e^{ik_{1y} y} + b_2 \frac{k_{2y}}{k_2^2} C_3 e^{-ik_{2y} y} - b_2 \frac{k_{2y}}{k_2^2} C_4 e^{ik_{2y} y} \right] \\
& + ig \frac{k_x}{k_t^2} e^{-ik_x x} \left( C_5 e^{-ik_{ty} y} + C_6 e^{ik_{ty} y} \right),
\end{aligned} \tag{2.17d}$$

where  $C_1$  to  $C_6$  are the unknown coefficients,  $b_{1,2} = a_1 - a_2 k_{1,2}^2$ ,  $a_1 = (\rho_{11}^* R - \rho_{12}^* Q) / (\rho_{22}^* Q - \rho_{12}^* R)$ ,  $a_2 = (PR - Q^2) / (\omega^2 [\rho_{22}^* Q - \rho_{12}^* R])$ ,  $k_{1,2}^2 = k_{1,2}^2 - k_x^2$  and  $g = -\rho_{12}^* / \rho_{22}^*$ . The stress components in solid and fluid phases can be determined using Eq. (2.17) substituted into Eqs. (2.8) and (9) as follows.

(2.18a)

$$\begin{aligned}
\sigma_y = e^{-ik_x x} & \left[ \left( 2N \frac{k_{1y}^2}{k_1^2} + A + b_1 Q \right) \left( C_1 e^{-ik_{1y} y} + C_2 e^{ik_{1y} y} \right) + \left( 2N \frac{k_{2y}^2}{k_2^2} + A + b_2 Q \right) \left( C_3 e^{-ik_{2y} y} + C_4 e^{ik_{2y} y} \right) \right] \\
& + 2N \frac{k_x k_{ty}}{k_t^2} \left( C_5 e^{-ik_{ty} y} - C_6 e^{ik_{ty} y} \right),
\end{aligned}$$

(2.18b)

$$\sigma_{xy} = e^{-ik_x x} N \left[ \frac{2k_x k_{1y}}{k_1^2} (C_1 e^{-ik_{1y} y} - C_2 e^{ik_{1y} y}) + \frac{2k_x k_{2y}}{k_2^2} (C_3 e^{-ik_{2y} y} - C_4 e^{ik_{2y} y}) \right] + \frac{(k_x^2 - k_{ty}^2)}{k_t^2} (C_5 e^{-ik_{ty} y} + C_6 e^{ik_{ty} y}),$$

(2.18c)

$$s = e^{-ik_x x} \left[ (Q + b_1 R) (C_1 e^{-ik_{1y} y} + C_2 e^{ik_{1y} y}) + (Q + b_2 R) (C_3 e^{-ik_{2y} y} + C_4 e^{ik_{2y} y}) \right].$$

### 2.3.3.3. Boundary conditions

The unknown Biot's coefficients are calculated by setting a set of appropriate boundary conditions at the interface of the porous layer with the surrounding fluid medium. The specific boundary conditions for this type of interface can be proposed in four conditions:

I. Compatibility of the mean pore fluid pressure ( $s$ ) with the acoustic pressure ( $p$ ) in the surrounding fluid:

$$s = -hp, \quad (2.19)$$

II. Compatibility of the normal stress in the solid phase ( $\sigma_y$ ) with the acoustic pressure in the surrounding fluid:

$$\sigma_y = -(1-h)p, \quad (2.20)$$

III. Vanishing of the tangential stress component:

$$\sigma_{xy} = 0, \quad (2.21)$$

IV. Compatibility of the normal volume velocities between the surrounding fluid and the porous material:

$$v_y = i\omega(1-h)u_y + i\omega h U_y. \quad (2.22)$$

Equations (19) to (22) can be readily written in a matrix form as:

$$[\mathbf{M}]_{8 \times 8} [\mathbf{X}]_{8 \times 1} = [\mathbf{B}]_{8 \times 1}, \quad (2.23)$$

in which

$$[\mathbf{X}]^T = [C_1 \ C_2 \ C_3 \ C_4 \ C_5 \ C_6 \ I_R \ I_T], \quad (2.24a)$$

$$[\mathbf{B}]^T = [-ih\rho_0\omega \ i(h-1)\rho_0\omega \ ik_y \ 0 \ 0 \ 0 \ 0 \ 0], \quad (2.24b)$$

where  $[\mathbf{X}]^T$  and  $[\mathbf{B}]^T$  are the transpose of  $\mathbf{X}$  and  $\mathbf{B}$ , respectively. The components of the matrix  $\mathbf{M}$  are listed in Appendix A. Therefore, by solving the matrix equation, we obtain the reflected ( $I_R$ ) and transmitted ( $I_T$ ) sound intensities as a function of incident angle and frequency.

#### 2.3.2.4. Sound transmission loss

The field quantity of interest in this problem is the sound transmission loss that can be determined as [28]:

$$\text{STL(dB)} = 10 \log_{10} (1/\tau), \quad (2.25)$$

where the sound transmission coefficient,  $\tau(\omega, \theta) = |I_T|^2 / |I_I|^2$ , is the ratio of the transmitted to the incident sound intensities. The incident sound intensity in this problem is assumed to be one. In the case of normal incidence STL, the angle is set to zero. This completes the necessary background required for the analysis of the problem.

#### 2.3.2.5. Material parameterization

For this application, PUA aerogels are considered as air-saturated porous materials. The air properties used in this chapter are listed in Table 2.1.

Table 2.1. The air properties used in the present calculations

Density ( $\rho_0$ , kg/m <sup>3</sup> )	0.909
Speed of sound ( $c_0$ , m/s)	328.6
Shear viscosity ( $\mu$ , Ns/m <sup>2</sup> )	$1.84 \times 10^{-5}$
Prandtl number (Pr)	0.715
Ratio of specific heats ( $\gamma$ )	1.2

The steady-state macroscopic airflow resistivity of the aerogels are estimated using the relation  $\sigma = 8\mu / \Gamma^2 h$  [25], where  $\Gamma$  is the average pore size diameter of the aerogel. The change in the average pore size diameter with aerogel bulk densities was found to be negligible and so its average value ( $\Gamma = 40.33$  nm) is considered in this study [5]. A similar scenario exists for the Poisson's ratio of the aerogels and therefore average Poisson's ratio of 0.22 is used here [5]. However, bulk Young's modulus significantly changes with bulk density. Experimental studies have shown a power-law relationship ( $E_1 = \alpha \rho^\kappa$ ) between aerogel Young's modulus and the aerogel bulk density [29]. Power law fitted parameters,  $\alpha$  and  $\kappa$ , for our PUA aerogels are obtained as 967.94 m<sup>2</sup>/s<sup>2</sup> and 2.004 respectively. In this study, a complex Young's modulus,  $E_1(1 + i\eta)$ , is considered where  $\eta$  is the solid phase loss factor in order to include the internal friction losses [17]. Typical loss factor at audio frequencies for polyurea ranges from 0.1 to 0.5 [30] and here we used 0.125. The last parameter is the geometrical structure factor of the aerogel ( $\varepsilon'$ ). This value is normally close to 1 for most of the porous materials [25]. All the parameters of the studied aerogels are listed in Table 2.2.

Table 2.2. The aerogel material parameters used in the present calculations

Bulk density ( $\rho_b$ , g/cm <sup>3</sup> )	0.11	0.25	0.45
Skeletal density ( $\rho_s$ , g/cm <sup>3</sup> )	1.24	1.24	1.24
Porosity ( $h$ )	0.91	0.80	0.64
Average pore size diameter ( $\Gamma$ , nm)	40.33	40.33	40.33
Static Young's modulus ( $E_1$ , MPa)	11.92	61.78	200.62
Average Poisson's ratio ( $\nu$ )	0.22	0.22	0.22
Loss factor ( $\eta$ )	0.125	0.125	0.125
Air flow resistivity (Ns/m <sup>4</sup> )	$9.93 \times 10^{10}$	$1.13 \times 10^{11}$	$1.42 \times 10^{11}$
Geometrical structure factor ( $\varepsilon'$ )	1	1	1

#### 2.4. Results and discussion

Figure 2.5 shows the morphology of the PUA aerogels at different bulk densities. The SEM images reveal that the morphology of the aerogels changes from a nanofibrous form at low bulk density (0.11 g/cc), gradually transitioning to a nano-particulate form in the medium bulk density (0.25 g/cc). In that range, nano-fibers evolve into strings of clusters and finally form a predominately nano-particulate pattern at higher bulk densities (0.45 g/cc). The structure of pores is highly random in all three samples.

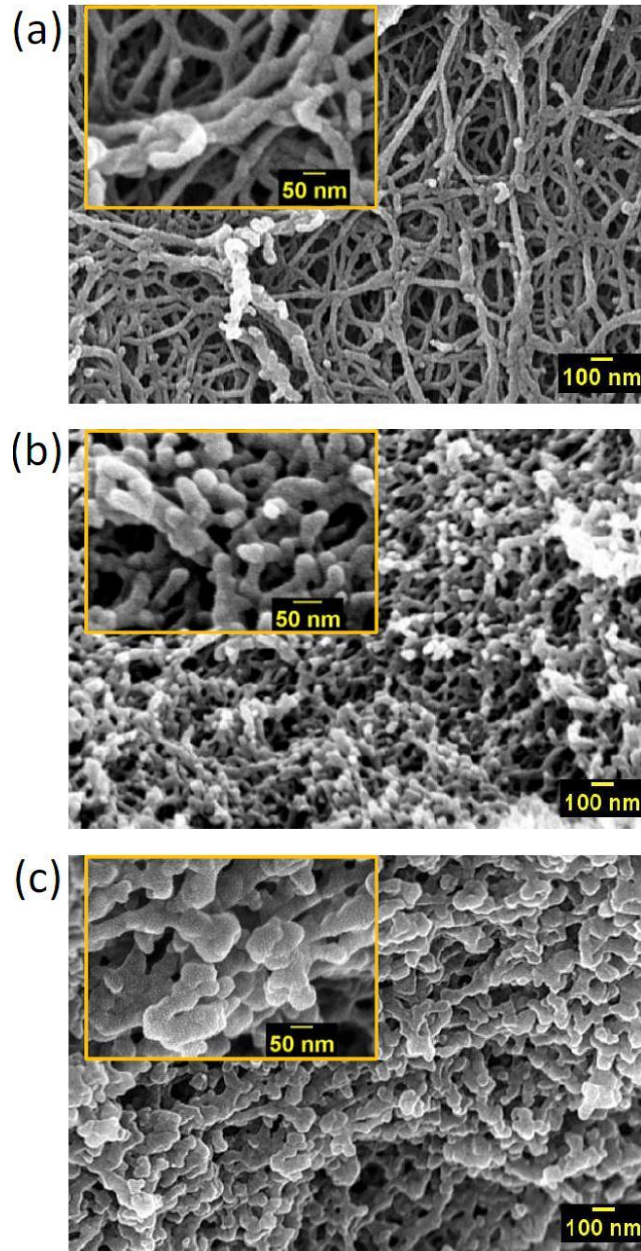


Figure 2.5. SEM images of PUA aerogels at different densities: (a)  $0.11 \text{ g/cm}^3$ , (b)  $0.25 \text{ g/cm}^3$  and (c)  $0.45 \text{ g/cm}^3$ . A higher resolution is given in the subset.

The normal incidence STL measurements of the PUA aerogels at three different bulk densities are shown in Figure 2.6. In order to compare the STL values of our aerogels with other relevant materials, we carried out the same experiments on a commercially available aerogel (Spaceloft® Blanket by Aspen Aerogels) consisting of a traditional silica aerogel monolith with embedded

glasswool fibers through its bulk, as well as on an acoustic foam (polyurethane-based) at similar densities. The STL values of our organic aerogels reached the 20-40 dB range, in contrast to other materials, which can only provide 5 dB or less (see Figure 2.6). All acoustical measurements were made in a very high-quality condition (i.e., high signal to noise ratio) over the entire frequency range and the repeated experiments on the same material had no significant uncertainty.

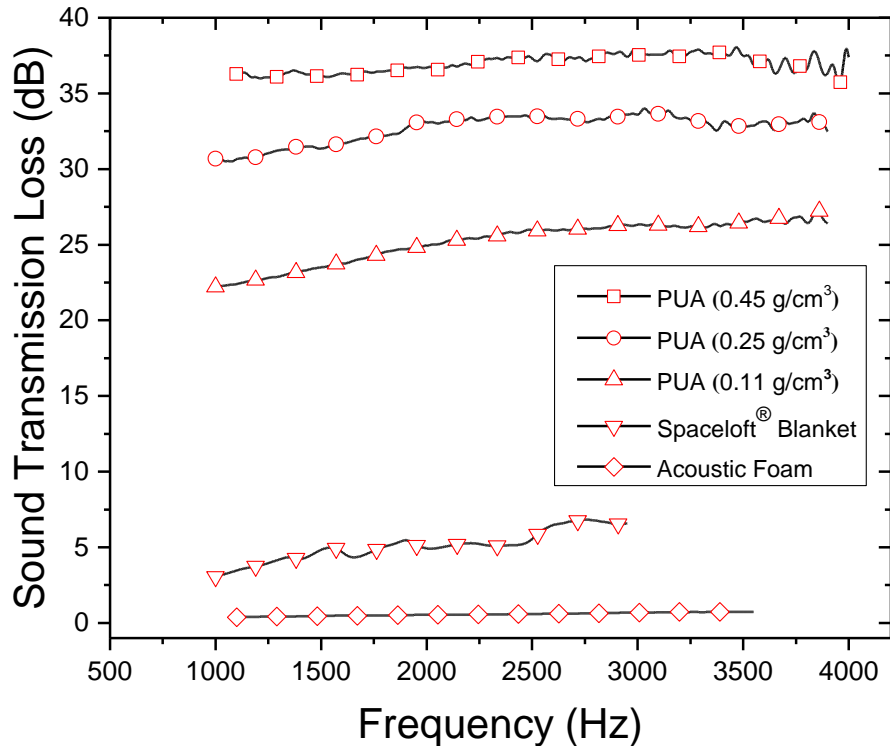


Figure 2.6. Experimental STL values of PUA aerogels in comparison with common commercial porous materials.

As mentioned earlier, in order to find the mechanisms behind this extraordinary sound insulation properties, at the first step, the forced vibration behavior of the aerogels are modeled via a linear mass-spring model. Figure 2.7 shows the comparison between the transmission losses as a function of the frequency for the monoatomic configuration when all the spring constants are identical and evenly distributed with the random arrangement when the spring constants are not identical and randomly distributed (see Figure 2.3). This result clearly reveals the idea that in a system with a

high level of structural randomness, as in our aerogels, there is indeed a super-gap in structural vibration transmission induced by a random distribution of the nanoparticles that can eventually lead to a significant reduction in sound transmission loss values. It is worth mentioning that no damping effect was introduced at this stage, thereby the super-gap did not originate from any damping energy mechanisms. On the contrary, by introducing viscous damping effects, it was found that the transmission loss resembled the undamped system with slight improvement at low frequencies.

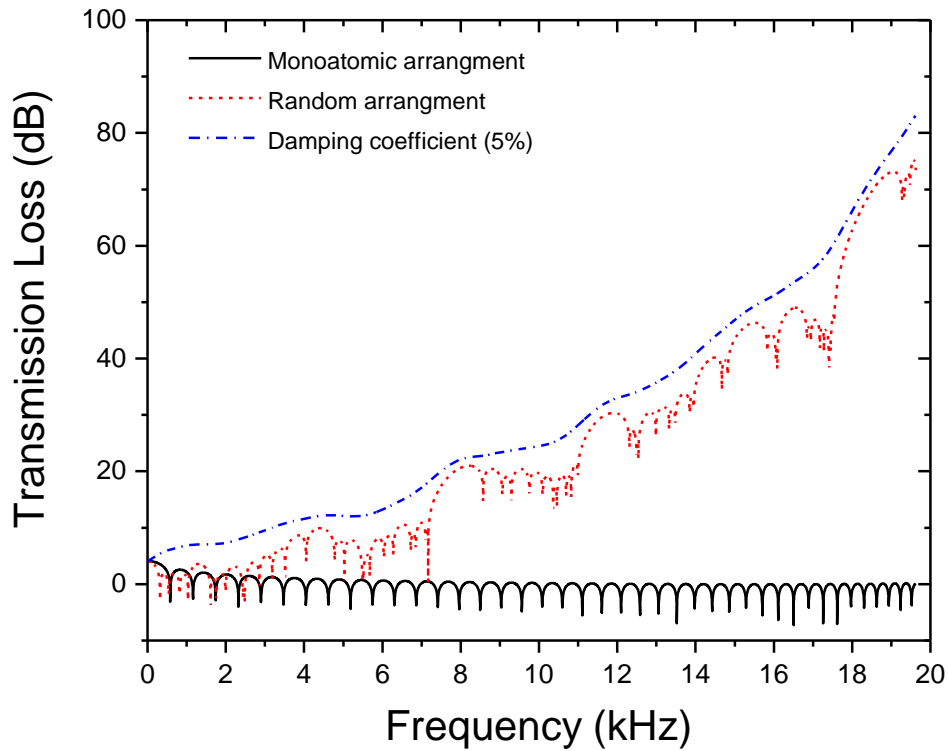


Figure 2.7. Vibration transmission loss as a function of frequency for the 60-DOF mass-spring system.

The band-gap that appeared in the random mass-spring system might have originated from the following two-wave attenuation mechanisms. First, backscattering might have been introduced by the differences between spring-constants, just as in phononic crystals. Phononic crystals have band gaps because of Bragg scattering due to their periodicity, and acoustic metamaterials due to their

local resonant modes. In our 1D model, none of those conditions exist, and thus the randomly distributed system can be identified as a new potential approach to introducing stopbands. Another reason for the existence of a super-gap is the so-called evanescent wave effect, which generates a wave propagation cut-off frequency above the highest natural frequency [31]. Having a high disparity in spring constants of the randomly distributed system, the evanescent wave effects induced by the soft springs (smaller spring constants) will dominate and thus attenuate the wave propagation at higher frequencies. For aerogels, the material contains relatively soft springs, and therefore the evanescent wave effects induced by them can be amplified tremendously, especially at high frequencies in high DOF systems, by working synergistically with stopbands (backscattering) effect introduced by the disparity in spring constants. All those mechanistic details render aerogels capable of having a super band-gap for acoustic wave propagations.

Although the mechanisms related to the mass-spring model are very interesting, that model is not predictive in terms of providing a quantitative comparison with actual experimental STL results. In order to rectify that issue, aerogels were considered at face-value, namely as air-filled porous materials, and the STL of a thin aerogel layer was calculated using Biot's dynamic theory of poroelasticity.

For three 5-mm thick PUA aerogel disks at different bulk densities, Figure 2.8 compares the experimental normal incidence STL values with those predicted by Biot's theory for an infinite aerogel layer in plane strain condition with similar density. Biot's theory, despite all the complexities in the molecular structure of the aerogels, has an overall agreement with the experimental results. This agreement is very good at the high-frequency range of the results (2500 Hz and above), while an increasing deviation exists at lower frequencies. For all samples, the average percent error between the experimental results and the theoretical predictions over the entire high-frequency range (2500 Hz and above) is about 1% while this error is about 18% at lower frequencies (2500 Hz and below). The reason for that deviation can be attributed to low-frequency airborne sound waves, which are directly related to the airflow properties of the aerogel. Therefore, material parameters such as the flow resistivity, and a structure factor should be calibrated more precisely for that range of frequencies. However, the very good agreement in the

high-frequency region supports sufficiently the applicability of Biot's dynamic theory to the study of sound wave propagation through ductile (i.e., polymeric) aerogels.

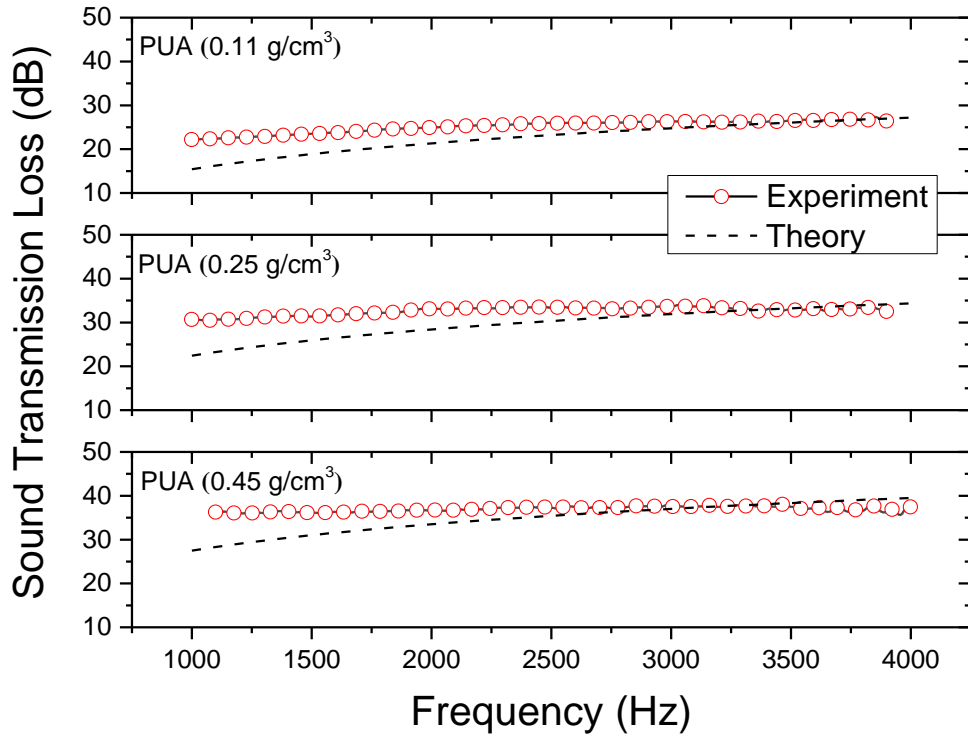


Figure 2.8. Experimental and theoretical STL values of PUA aerogels at different densities.

In order to illustrate the sensitivity of the STL values to changes in the bulk density of the aerogel, all parameters required by Biot's theory are determined as a function of the bulk density. Figure 2.9 shows the contour plot for the normal incidence STL values of a 5-mm thick ductile aerogel infinite plate as a function of bulk density and frequency. It is revealed that the transmission loss gradually increases with aerogel densifying through the whole frequency range. This rate of increase is higher at high frequencies. The variation of STL with the bulk density is very important in the process of the design and manufacturing of potential aerogel-based sound barriers and structures.

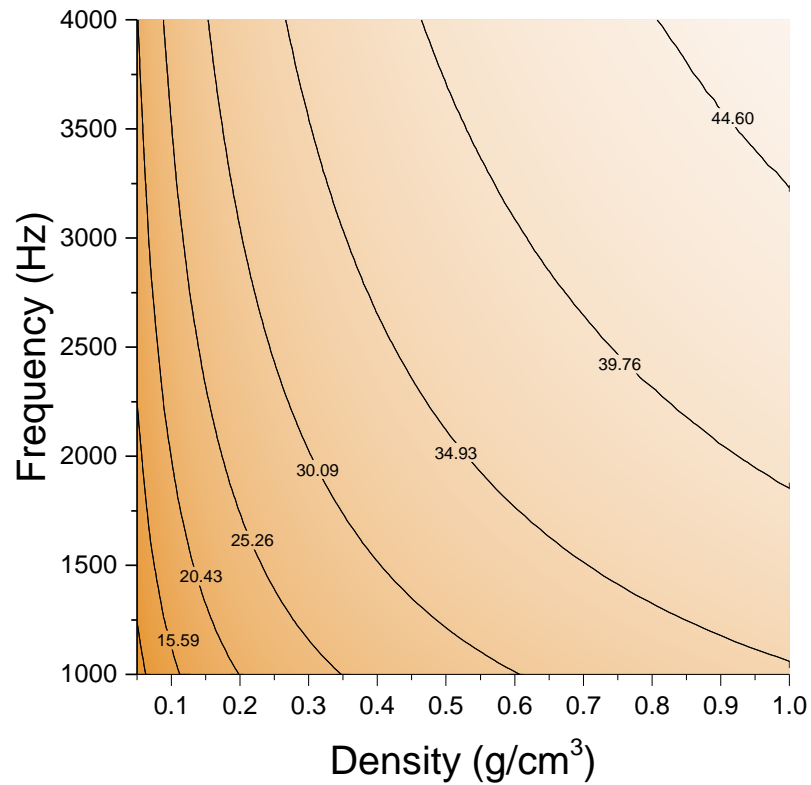


Figure 2.9. Contour plot of STL in dB as a function of frequency and bulk density at a constant thickness (5 mm).

Furthermore, the effect of aerogel panel thickness on the normal incidence STL values are studied and the results for the constant bulk density of  $0.25 \text{ g/cm}^3$  are shown in Figure 2.10. The STL values initially increase by thickening the aerogel panel, but later, they are affected by a resonance feature, which leads to a decrease in STL values. This resonance area is highlighted by white contour lines in Figure 2.10.

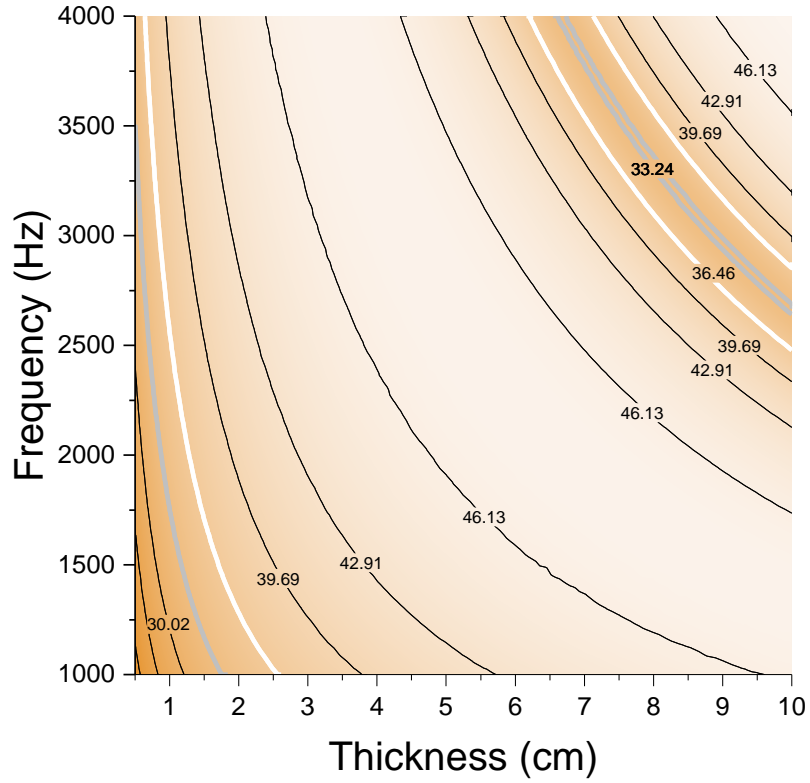


Figure 2.10. Contour plot of STL in dB as a function of frequency and thickness at constant bulk density ( $0.25 \text{ g/cm}^3$ ).

The nature of that resonance feature can be related to the longitudinal resonance characteristics of the aerogel panel. Considering only the solid phase, the fundamental longitudinal resonance frequency of an infinite porous layer can be approximated as:

$$f_r = \sqrt{\frac{E_1(1-h)}{\rho_s L^2}}, \quad (2.26)$$

where  $L$  is the panel thickness. Eq. (2.26) can predict the fundamental longitudinal resonance frequency of the aerogel consistent with the results in Figure 2.10. For the three different aerogel thicknesses of 7, 8 and 9 cm, Eq. (2.26) estimates the fundamental longitudinal resonance frequencies to be 3175.93 Hz, 2778.94 Hz, and 2470.17 Hz, respectively.

## 2.5. Conclusion

In this chapter, we have reported an extraordinary sound transmission loss for a family of polyurea aerogels. The goal of this work was to present some preliminary analytical models on the porous aerogel materials with nanoscale morphologies, in order to help us understand their significant acoustical behavior. Using a one-dimensional mass-spring system with a random spring constant distribution, the aerogel random and amorphous structure was modeled. The vibration transmission loss results revealed a broadband vibration gap feature for such systems originated mainly from their structural randomness. This simple model clearly indicates that a nanostructured random and amorphous material (i.e., aerogels) can act as a wave transmission attenuator for a certain frequency range. Then, the acoustic wave propagation in aerogels was modeled based on Biot's theory of dynamic poroelasticity. The theoretical normal incidence sound transmission loss values were compared with the experimental results at different aerogel bulk densities. An overall good agreement was obtained for all densities, which supports the feasibility of the Biot's theory based implementation on the aerogel wave propagation modeling applications. The effects of bulk density and panel thickness on the sound transmission loss behavior were studied. Some longitudinal resonance features were obtained in the sound transmission loss results of the aerogel panels.

Lastly, we should mention that there is still a need to establish a direct connection between the true micro/nanostructure of each synthesized aerogel sample with the theoretical model. The presented models and methodologies are only able to model a general picture of this complex and hierarchical problem. Despite the acceptable Biot's performance, for instance, the low-frequency deviation between the theory and the experiment needs to be fully understood. Either more detailed and accurate Biot's based material characterizations or generating micro and nanoscale simulation results based on MD or first-principle based models can expand our understanding and lead us to a better and more clear picture of the wave propagation properties of aerogels.

## CHAPTER 3

### SOUND TRANSMISSION LOSS ENHANCEMENT IN AN INORGANIC-ORGANIC LAMINATED COMPOSITE PANEL USING MULTIFUNCTIONAL LOW-DENSITY NANOPOROUS POLYUREA AEROGELS

Recently, we have reported an exceptional normal incidence sound transmission loss characteristic for a class of low density, highly porous and mechanically strong polyurea aerogels. Herein, a laminated composite comprising the organic low-density aerogels bonded with an inorganic compound (e.g., gypsum materials) is considered to investigate the constrained damping effects of the aerogels on the airborne sound insulation behavior of the composite using the standard chamber-based diffuse sound field measurements. Huge improvement in the sound transmission loss was obtained due to the use of aerogel without a significant increase in the overall weight and thickness of the composite panel (e.g., more than 10 dB increase by reaching 40 dB sound transmission loss at 2 kHz after the implementation of only two 5 mm-thick aerogel layers at bulk densities 0.15 and 0.25 g cm<sup>-3</sup>). This uncommon behavior breaks the empirical “Mass Law” nature of the most conventional acoustic materials. In addition, an exact analytical time-harmonic plane-strain solution for the diffused wave propagation through the multilayered structure is provided using theories of linear elasticity and Biot’s dynamic poroelasticity. The theoretical results were well supported by the experiments which can be utilized for the design of the future light-weight multifunctional composite structures.

#### 3.1. Introduction

Multifunctional composites have become tremendously important in recent years in the pursuit of simultaneous improvements in various properties such as ductility, vibro-acoustical damping, load-bearing capacity, fracture toughness and thermal conductivity [32], [33]. For instance, fiber/nanotube-reinforced polymer and ceramic-matrix composites have been widely used in different roles mainly in load-bearing applications [34]. However, in various engineering circumstances (e.g., light structure engineering applications, aeronautical and aerospace technologies), the required multifunctional materials should be also lightweight and at

the same time mechanically strong [35]. Aerogel materials are among the multifunctional materials that can accomplish the stated requirements.

Aerogels are known as very low density and extremely high porous materials [2]. Conventional aerogels have primarily been made from supercritical drying of a wet silica gel [2,36]. Silica aerogels, due to their very attractive attributes such as extremely low thermal conductivity, mesoporosity, and useful chemical and physical properties, have been successfully implemented in different applications (e.g., thermal insulation and space exploration through NASA's Stardust Program) [37], [38]. However, despite their great potentials, they suffer from extreme structural fragility, hydrophilicity and the need for supercritical drying. These limitations have been addressed by introducing polymer cross-linked silica aerogels (known as X-aerogels) [4] and/or emerging purely organic aerogels [39]. All major polymeric classes such as polyureas [5], polyurethanes [6], polyimides [7] and polyamides (Kevlar<sup>TM</sup>-like) [8] have been investigated in this new material concept. Indeed, new applications that were previously unrelated to aerogels, as in ballistic protection (armor), have now become feasible [9].

Focusing on polyurea (PUA) aerogels, co-authors previously reported a class of mechanically strong and ductile formulas derived from isocyanate and water, yielding to highly porous (up to 98.6% v/v) with a broad density ranged (0.016–0.55 g cm<sup>-3</sup>) PUA aerogels [5]. The reported mechanical properties of the aerogels (e.g., up to 300 MPa, 631 MPa, and 88% for Young's modulus, ultimate stress, and strain, respectively, at densities lower than 0.5 g cm<sup>-3</sup>) indicate a high level of ductility and load-bearing capacity for a very low-density material [5]. Recently, we also discovered exceptionally high normal incidence sound transmission loss (STL) properties for these PUA aerogels [12,20]. The STL values were reached up to 40 dB, in contrast to traditional acoustics materials, such as polyurethane foam, which can only reach up to 5 dB [12]. Furthermore, despite most passive materials (e.g., open-celled materials), which have weak acoustic performance in sonic absorption at low-frequency range (i.e., less 5 kHz) [40], the aerogels showed remarkably high acoustic absorption and attenuation over the entire low-frequency range. Such a great attribute originates from the random multiscale heterogeneous structural elements and hierarchical porosities of the aerogels which provide highly tortuous flow streams for air molecules. All these synergistic dynamic mechanisms would eventually yield a broadband

acoustic attenuation which makes the aerogels unique for soundproofing applications. Due to these vast and various interesting behaviors and characteristics, we can outline the PUA aerogels to be named as a truly “Multifunctional Material”.

Excitingly enough, it is natural now to investigate the aerogels in a composite arrangement (e.g., a laminated composite configuration) to have further analysis towards more advanced engineering application purposes. Accordingly, aerogel materials (i.e., in the form of thin sheets) were synthesized at different dimensions, bulk densities, and porosities. The thin aerogel sheets were then integrated between two gypsum wallboards which are used commonly in soundproofing applications. Standard field acoustic measurements were carried out to study the effects of aerogel constraint properties on the airborne sound insulation characteristics of the sandwich structures. Finally, the experimental results were further studied by comparing with theoretical predictions obtained from an exact analytical wave propagation approach based on Biot’s dynamic poroelasticity and linear elasticity.

## 3.2. Materials and methods

### 3.2.1. Preparation and characterization of PUA aerogels

Here, the PUA aerogels were prepared according to the previous procedures published by the co-authors [5]. Bulk density ( $\rho_b$ ) of the aerogels were measured from the weight and the physical dimensions of the samples. Primarily for this study, the aerogels were synthesized at two different bulk densities of 0.15 and 0.25 g cm<sup>-3</sup>. The skeletal densities ( $\rho_s$ ) of the aerogels were considered to be 1.24 g cm<sup>-3</sup> at all bulk densities [5]. The aerogel porosities ( $h$ ) were estimated using  $h = 100 \times [(\rho_s - \rho_b) / \rho_s]$  to be approximately 88% and 80% at bulk densities 0.15 and 0.25 g cm<sup>-3</sup>, respectively. The morphology of the aerogels was characterized using SEM images taken from Au-coated samples on a Hitachi model S-4700 field emission microscope.

### 3.2.2. Preparation of laminated composites

The general layer-by-layer approach was used for the preparation of the composite samples. The polyurea gel panels were dried in ambient conditions to form 5 mm-thick aerogel sheets. Two aerogel materials with different densities were then bonded together and the combination was later

integrated between two gypsum wallboards of uniform thickness of 10 mm. The bulk density of the gypsum material was  $1 \text{ g cm}^{-3}$ . All layers were glued together using a thin layer of green glue material. The acoustical properties of this arrangement were compared with a reference sample including only two similar gypsum wallboards of same thickness and density, bonded together using the same green glue. Two sets of samples were prepared at two different dimensions. The first and second sample sets were prepared with incidence areas of  $1 \text{ m}^2$  and  $10 \text{ m}^2$ , respectively. The larger samples were prepared by consolidating of the smaller sized samples (see Fig. 3.1).

### 3.2.3. Airborne sound transmission loss measurements

The measurements were carried out in compliance with ASTM standard E90 [41] (similar to ISO 140 [42]). In this experiment, the test sample is placed at the opening of two adjacent reverberation rooms. The sample is excited by a diffuse incident sound field from one side and the radiated sound pressure levels in the other room are measured. The airborne sound transmission loss is then calculated based on the sound pressure levels in both rooms, the sound absorption in the receiving room and the incidence area of the sample. The measurement frequency range was set to 100-5000 Hz. The experiments were arranged in a way that the main sound transmission path is through the test samples. Therefore, in the case of  $1 \text{ m}^2$  test sample, the rooms were only connected with an open window area where the test sample was located. While, for the  $10 \text{ m}^2$  test sample, the rooms were separated by the test sample itself generating a wall between the two rooms. Figs. 1a-f show the process of experimental sample and setup preparations.

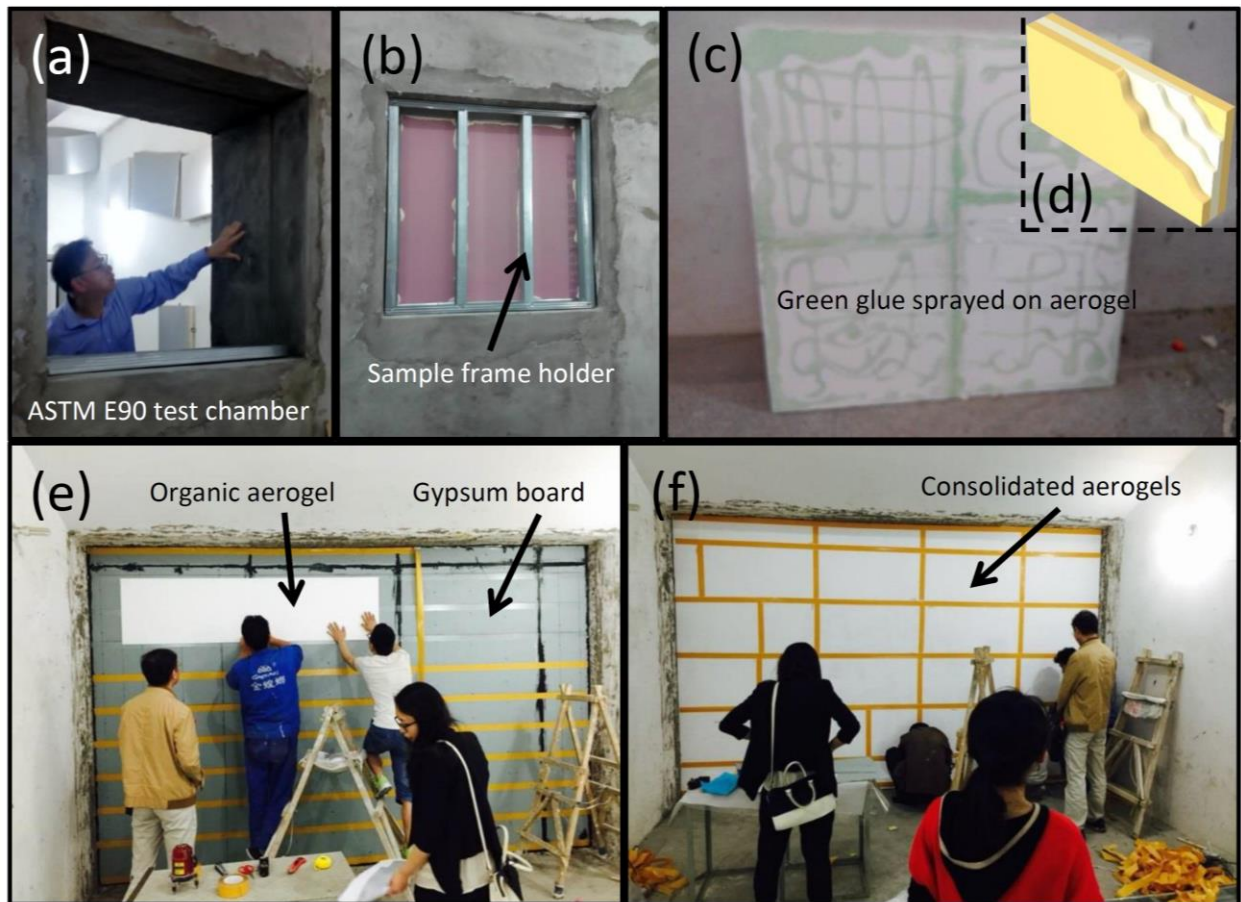


Figure 3.1. (a) A view from the connecting window of the ASTM E90 test chamber prepared for a  $1 \text{ m}^2$  test specimen; (b)  $1 \text{ m}^2$  test sample installation with using sample frame holders in compliance with ASTM E90; (c) A view from an aerogel panel sprayed with green glue before bonding to the another layer; (d) A schematic for the final configuration of the composite sample including two gypsum skin layers (shown in yellow color) accompanied with two core aerogel layers (shown in white color); (e)  $10 \text{ m}^2$  composite sample preparation by consolidating several smaller aerogel samples using double-sided tapes and green glue; (f) A view from a  $10 \text{ m}^2$  aerogel layer.

### 3.3. Analytical modeling

The 3D coupled structural-acoustic problem can be simplified with a 2D plane strain problem in order to construct an analytical framework for the STL characteristics of the layered structure. Therefore, in this section, the required essential core formulations in the context of the standard theoretical acoustics coupled with the theories of linear elasticity and Biot's dynamic poroelasticity will be summarized.

The problem geometry is depicted in Fig. 3.2 where the Cartesian coordinate system is  $\{o; x, y, z\}$ . A semi-infinite multilayered plate is submerged in an unbounded inviscid acoustic medium and  $y$ -axis is normal to the plate boundary. The multilayered plate contains two isotropic linear elastic layers at the top and the bottom, and two poroelastic interlayers in between. Here it is assumed that all layers are perfectly bonded together and a time-harmonic incident plane acoustic wave at an angle  $\theta$  with respect to  $y$ -axis is impinging to the plate. The time dependency term (i.e.,  $e^{i\omega t}$ ) is suppressed throughout for simplicity.

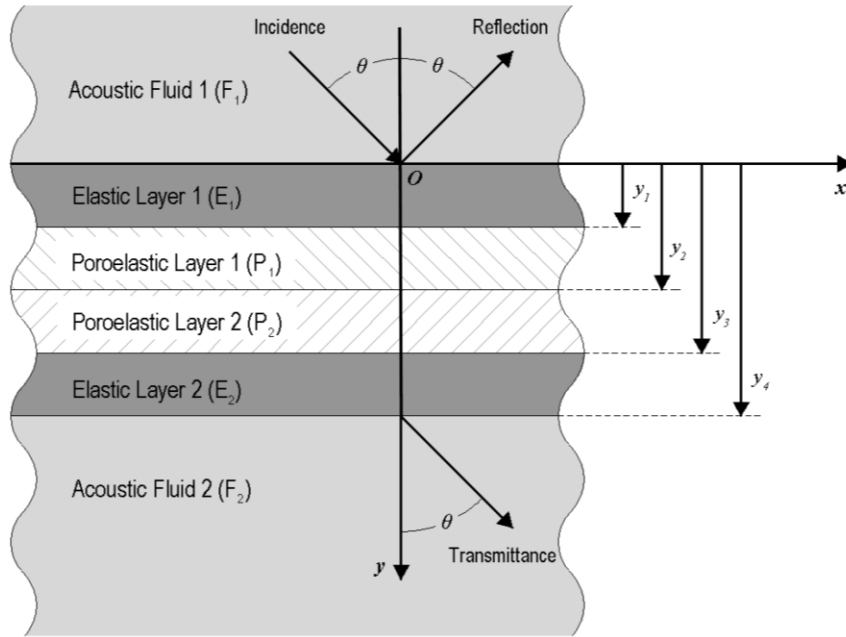


Figure 3.2. The schematic diagram for the laminated composite lay-up and sound transmission problem model.

### 3.3.1. Acoustic fluid medium

Using standard acoustic field equations, the normal fluid velocity and the acoustic pressure in the fluid mediums 1 and 2 can be expressed in terms of the incident, reflected and transmitted acoustic wave amplitudes (i.e.,  $I_I$ ,  $I_R$  and  $I_T$  respectively), as follows [17]:

$$v_y^{(F_1)} = ik_y e^{-ik_y x} (I_I e^{-ik_y y} - I_R e^{ik_y y}), \quad (3.1)$$

$$v_y^{(F_2)} = i k_y I_T e^{-i(k_x x + k_y y)}, \quad (3.2)$$

and

$$p^{(F_1)} = i \omega \rho_F e^{-i k_x x} \left( I_L e^{-i k_y y} + I_R e^{i k_y y} \right), \quad (3.3)$$

$$p^{(F_2)} = i \omega \rho_F I_T e^{-i(k_x x + k_y y)}, \quad (3.4)$$

where  $v_y^{(F_1)}$  and  $v_y^{(F_2)}$  are the normal fluid velocities,  $p^{(F_1)}$  and  $p^{(F_2)}$  are the acoustic pressures in the fluid mediums 1 and 2, respectively,  $\rho_F$  is the fluid density,  $k_x = k \sin \theta$  and  $k_y = k \cos \theta$  are the wavenumbers in  $x$ - and  $y$ -directions,  $k = \omega / c_0$  is the acoustic wave number,  $\omega$  is the circular frequency and  $c_0$  is the speed of sound in the fluid mediums.

### 3.3.2. Isotropic linear elastic medium

Using elastic wave potential technique following from the Helmholtz theorem, the wave propagation in homogenous isotropic linear elastic mediums can be analytically characterized [43]. In this context, considering the plane strain condition, the displacements (i.e.,  $u_x^{(E)}$  and  $u_y^{(E)}$ ) and stresses (i.e.,  $\sigma_{yy}^{(E)}$  and  $\sigma_{xy}^{(E)}$ ) for an isotropic linear elastic medium can be written in terms of the propagated P- and S- wavenumbers along the  $y$ -direction (i.e.,  $K_p^{(E)}$  and  $K_s^{(E)}$ ) [43]:

$$u_x^{(E)} = i e^{-i k_x x} \left[ -k_x \left( C_1^{(E)} e^{i K_p^{(E)} y} + C_2^{(E)} e^{-i K_p^{(E)} y} \right) + K_s^{(E)} \left( C_3^{(E)} e^{i K_s^{(E)} y} - C_4^{(E)} e^{-i K_s^{(E)} y} \right) \right], \quad (3.5)$$

$$u_y^{(E)} = i e^{-i k_x x} \left[ K_p^{(E)} \left( C_1^{(E)} e^{i K_p^{(E)} y} - C_2^{(E)} e^{-i K_p^{(E)} y} \right) + k_x \left( C_3^{(E)} e^{i K_s^{(E)} y} + C_4^{(E)} e^{-i K_s^{(E)} y} \right) \right], \quad (3.6)$$

and

$$\begin{aligned} \sigma_{yy}^{(E)} = & -e^{-i k_x x} \left[ 2\mu^{(E)} k_x K_s^{(E)} \left( C_3^{(E)} e^{i K_s^{(E)} y} - C_4^{(E)} e^{-i K_s^{(E)} y} \right) \right. \\ & \left. + \left( \lambda^{(E)} k_x^2 + (\lambda^{(E)} + 2\mu^{(E)}) (K_p^{(E)})^2 \right) \cdot \left( C_1^{(E)} e^{i K_p^{(E)} y} + C_2^{(E)} e^{-i K_p^{(E)} y} \right) \right], \end{aligned} \quad (3.7)$$

$$\begin{aligned} \sigma_{xy}^{(E)} = & \mu^{(E)} e^{-ik_x x} \left[ \left( (k_x)^2 - (K_p^{(E)})^2 \right) \left( C_3^{(E)} e^{iK_s^{(E)} y} + C_4^{(E)} e^{-iK_s^{(E)} y} \right) \right. \\ & \left. - 2k_x K_p^{(E)} \left( C_1^{(E)} e^{iK_p^{(E)} y} - C_2^{(E)} e^{-iK_p^{(E)} y} \right) \right], \end{aligned} \quad (3.8)$$

in which  $\lambda^{(E)}$  and  $\mu^{(E)}$  are the Lamé constant and shear modulus of the elastic medium, respectively,  $K_p^{(E)} = \sqrt{(\omega/c_p^{(E)})^2 - k_x^2}$ ,  $K_s^{(E)} = \sqrt{(\omega/c_s^{(E)})^2 - k_x^2}$ ,  $c_p^{(E)} = \sqrt{(\lambda^{(E)} + 2\mu^{(E)})/\rho^{(E)}}$  and  $c_s^{(E)} = \sqrt{\mu^{(E)}/\rho^{(E)}}$  are the wavenumbers and velocities of primary and secondary waves, respectively,  $\rho^{(E)}$  is the elastic solid material density and  $C_1^{(E)}$  to  $C_4^{(E)}$  are the elastic unknown coefficients. For the top elastic layer, the superscript (E) will be changed to  $(E_1)$  and for the bottom one to  $(E_2)$ .

### 3.3.3. Linear poroelastic medium

Elastic wave propagations in porous media are here analyzed using Biot's theory of dynamic poroelasticity [44–46]. According to this theory, the porous material is considered as a macroscopically homogeneous and isotropic two-phase solid/fluid material. The dilatational wave propagation in the solid phase can be expressed by a fourth-order wave equation in terms of solid volumetric strain (i.e.,  $e^{(P)}$ ) as [25,47]:

$$\nabla^4 e^{(P)} + A_1^{(P)} \nabla^2 e^{(P)} + A_2^{(P)} e^{(P)} = 0, \quad (3.9)$$

where

$$A_1^{(P)} = \omega^2 \left( \rho_{11}^{*(P)} R^{(P)} - 2\rho_{12}^{*(P)} Q^{(P)} + \rho_{22}^{*(P)} P^{(P)} \right) / \left( P^{(P)} R^{(P)} - (Q^{(P)})^2 \right), \quad (3.9a)$$

$$A_2^{(P)} = \omega^4 \left( \rho_{11}^{*(P)} \rho_{22}^{*(P)} - (\rho_{12}^{*(P)})^2 \right) / \left( P^{(P)} R^{(P)} - (Q^{(P)})^2 \right) \quad (3.9b)$$

$$P^{(P)} = A^{(P)} + 2N^{(P)} \quad (3.9c)$$

$$\rho_{11}^{*(P)} = \rho_1^{(P)} + \rho_a^{(P)} + b^{(P)}/i\omega, \quad (3.9d)$$

$$\rho_{12}^{*(P)} = -\rho_a^{(P)} - b^{(P)}/i\omega, \quad (3.9e)$$

$$\rho_{22}^{*(P)} = \rho_2^{(P)} + \rho_a^{(P)} + b^{(P)}/i\omega, \quad (3.9f)$$

in which  $A^{(P)}$  and  $N^{(P)}$  are the bulk in-vacuo Lamé constant and the shear modulus of the solid phase, respectively,  $Q^{(P)} = (1-h^{(P)})E_2^{(P)}$ , is the coupling between fluid and solid phases,  $h^{(P)}$  is the material porosity and  $E_2^{(P)}$  is the bulk modulus of elasticity for the fluid in the pores.  $R^{(P)}$ , here is assumed to be  $h^{(P)}E_2^{(P)}$  and  $b^{(P)}$  is a viscous coupling factor related to the macroscopic flow resistivity of the porous material,  $\rho_1^{(P)}$  and  $\rho_2^{(P)} = h^{(P)}\rho_0^{(P)}$  are the bulk densities of the solid and fluid phases respectively and  $\rho_a^{(P)} = \rho_2^{(P)}[(\varepsilon')^{(P)} - 1]$  is the inertial coupling parameter between the fluid and solid phases. For cylindrical pores, the coefficient  $b^{(P)}$  can be expressed as

$b^{(P)} = i\omega\varepsilon^{(P)'}\rho_2^{(P)}\left(\frac{\rho_c^{*(P)}}{\rho_0^{(P)}} - 1\right)$  in which  $\rho_c^{*(P)}$  can be defined as [25]:

$$\rho_c^{*(P)} = \rho_0^{(P)} \left[ 1 - \frac{2J_1(\lambda_c^{(P)}\sqrt{-i})}{\lambda_c^{(P)}\sqrt{-i}J_0(\lambda_c^{(P)}\sqrt{-i})} \right]^{-1}. \quad (3.10)$$

where  $(\lambda_c^{(P)})^2 = \frac{8\omega\rho_0^{(P)}(\varepsilon')^{(P)}}{h^{(P)}\sigma^{(P)}}$ ,  $J_0$  and  $J_1$  are the first kind Bessel functions of zero and first orders respectively. Also  $(\varepsilon')^{(P)}$  is the geometrical structure factor and  $\sigma^{(P)}$  is the steady-state macroscopic flow resistivity of the porous material.

Two plane harmonic solutions for the Eq. (3.9) can be obtained associated with the wavenumbers given by  $(k_{1,2}^{(P)})^2 = \left(A_1^{(P)} \pm \sqrt{(A_1^{(P)})^2 - 4A_2^{(P)}}\right)/2$ . The rotational wave in the solid phase can be also expressed by another wave equation in terms of solid rotational strain (i.e.,  $\omega^{(P)}$ ) as [25]:

$$\nabla^2\omega^{(P)} + (k_t^{(P)})^2\omega^{(P)} = 0, \quad (3.11)$$

where the wavenumber  $(k_t^{(P)})^2 = (\omega^2/N^{(P)})/(\rho_{11}^{*(P)} - (\rho_{12}^{*(P)})^2/\rho_{22}^{*(P)})$ . In Biot's theory, the volumetric and rotational strains in the fluid phase of the porous medium are determined in terms of the volumetric and rotational strains in the solid phase and therefore by solving wave equations,

Eqs. (9) and (10), the strain fields in the fluid and solid phases both can be obtained (for more details, check [25]). Consequently, by having the strain fields, the plane strain displacements for the solid (i.e.,  $u_x^{(P)}$  and  $u_y^{(P)}$ ) and fluid (i.e.,  $U_x^{(P)}$  and  $U_y^{(P)}$ ) phases can be obtained as follows [25,27]:

$$u_x^{(P)} = ik_x e^{-ik_x x} \left[ \frac{C_1^{(P)}}{(k_1^{(P)})^2} e^{-ik_{1y}^{(P)} y} + \frac{C_2^{(P)}}{(k_1^{(P)})^2} e^{ik_{1y}^{(P)} y} + \frac{C_3^{(P)}}{(k_2^{(P)})^2} e^{-ik_{2y}^{(P)} y} + \frac{C_4^{(P)}}{(k_2^{(P)})^2} e^{ik_{2y}^{(P)} y} \right] - i \frac{k_{ty}^{(P)}}{(k_t^{(P)})^2} e^{-ik_x x} \left( C_5^{(P)} e^{-ik_{ty}^{(P)} y} - C_6^{(P)} e^{ik_{ty}^{(P)} y} \right), \quad (3.12-1)$$

$$u_y^{(P)} = ie^{-ik_x x} \left[ \frac{k_{1y}^{(P)}}{(k_1^{(P)})^2} C_1^{(P)} e^{-ik_{1y}^{(P)} y} - \frac{k_{1y}^{(P)}}{(k_1^{(P)})^2} C_2^{(P)} e^{ik_{1y}^{(P)} y} + \frac{k_{2y}^{(P)}}{(k_2^{(P)})^2} C_3^{(P)} e^{-ik_{2y}^{(P)} y} - \frac{k_{2y}^{(P)}}{(k_2^{(P)})^2} C_4^{(P)} e^{ik_{2y}^{(P)} y} \right] + i \frac{k_x}{(k_t^{(P)})^2} e^{-ik_x x} \left( C_5^{(P)} e^{-ik_{ty}^{(P)} y} + C_6^{(P)} e^{ik_{ty}^{(P)} y} \right), \quad (3.12-2)$$

$$U_x^{(P)} = ik_x e^{-ik_x x} \left[ \frac{b_1^{(P)} C_1^{(P)}}{(k_1^{(P)})^2} e^{-ik_{1y}^{(P)} y} + \frac{b_1^{(P)} C_2^{(P)}}{(k_1^{(P)})^2} e^{ik_{1y}^{(P)} y} + \frac{b_2^{(P)} C_3^{(P)}}{(k_2^{(P)})^2} e^{-ik_{2y}^{(P)} y} + \frac{b_2^{(P)} C_4^{(P)}}{(k_2^{(P)})^2} e^{ik_{2y}^{(P)} y} \right] - ig^{(P)} \frac{k_{ty}^{(P)}}{(k_t^{(P)})^2} e^{-ik_x x} \left( C_5^{(P)} e^{-ik_{ty}^{(P)} y} - C_6^{(P)} e^{ik_{ty}^{(P)} y} \right), \quad (3.12-3)$$

$$U_y^{(P)} = ie^{-ik_x x} \left[ \frac{b_1^{(P)} k_{1y}^{(P)} C_1^{(P)}}{(k_1^{(P)})^2} e^{-ik_{1y}^{(P)} y} - \frac{b_1^{(P)} k_{1y}^{(P)} C_2^{(P)}}{(k_1^{(P)})^2} e^{ik_{1y}^{(P)} y} + \frac{b_2^{(P)} k_{2y}^{(P)} C_3^{(P)}}{(k_2^{(P)})^2} e^{-ik_{2y}^{(P)} y} - \frac{b_2^{(P)} k_{2y}^{(P)} C_4^{(P)}}{(k_2^{(P)})^2} e^{ik_{2y}^{(P)} y} \right] + ig^{(P)} \frac{k_x}{(k_t^{(P)})^2} e^{-ik_x x} \left( C_5^{(P)} e^{-ik_{ty}^{(P)} y} + C_6^{(P)} e^{ik_{ty}^{(P)} y} \right), \quad (3.12-4)$$

where

$$(k_{1,2y}^{(P)})^2 = (k_{1,2}^{(P)})^2 - k_x^2, \quad (3.12a)$$

$$(k_{ty}^{(P)})^2 = (k_t^{(P)})^2 - k_x^2, \quad (3.12b)$$

$$b_{1,2}^{(P)} = a_1^{(P)} - a_2^{(P)} (k_{1,2}^{(P)})^2, \quad (3.12c)$$

$$a_1^{(P)} = (\rho_{11}^{*(P)} R^{(P)} - \rho_{12}^{*(P)} Q^{(P)}) / (\rho_{22}^{*(P)} Q^{(P)} - \rho_{12}^{*(P)} R^{(P)}), \quad (3.12d)$$

$$a_2^{(P)} = (P^{(P)} R^{(P)} - (Q^{(P)})^2) / (\omega^2 [\rho_{22}^{*(P)} Q^{(P)} - \rho_{12}^{*(P)} R^{(P)}]), \quad (3.12e)$$

$$g^{(P)} = -\rho_{12}^{*(P)} / \rho_{22}^{*(P)}, \quad (3.12f)$$

and  $C_1^{(P)}$  to  $C_6^{(P)}$  are the unknown coefficients. The plain-strain stress components in the solid phase (i.e.,  $\sigma_{yy}^{(P)}$  and  $\sigma_{xy}^{(P)}$ ) and the fluid pressure (i.e.,  $s^{(P)}$ ) in the fluid phase of the porous medium can be obtained from the Biot's stress-strain relationships as [25,27]:

$$\begin{aligned} \sigma_{yy}^{(P)} = e^{-ik_x x} & \left[ \left( 2N^{(P)} \frac{(k_{1y}^{(P)})^2}{(k_1^{(P)})^2} + A^{(P)} + b_1^{(P)} Q^{(P)} \right) \left( C_1^{(P)} e^{-ik_{1y}^{(P)} y} + C_2^{(P)} e^{ik_{1y}^{(P)} y} \right) \right. \\ & + \left. \left( 2N^{(P)} \frac{(k_{2y}^{(P)})^2}{(k_2^{(P)})^2} + A^{(P)} + b_2^{(P)} Q^{(P)} \right) \left( C_3^{(P)} e^{-ik_{2y}^{(P)} y} + C_4^{(P)} e^{ik_{2y}^{(P)} y} \right) \right] \\ & + 2N^{(P)} \frac{k_x k_{ty}^{(P)}}{(k_t^{(P)})^2} \left( C_5^{(P)} e^{-ik_{ty}^{(P)} y} - C_6^{(P)} e^{ik_{ty}^{(P)} y} \right), \end{aligned} \quad (3.13-1)$$

$$\begin{aligned} \sigma_{xy}^{(P)} = e^{-ik_x x} N^{(P)} & \left[ \frac{2k_x k_{1y}^{(P)}}{(k_1^{(P)})^2} \left( C_1^{(P)} e^{-ik_{1y}^{(P)} y} - C_2^{(P)} e^{ik_{1y}^{(P)} y} \right) + \frac{2k_x k_{2y}^{(P)}}{(k_2^{(P)})^2} \left( C_3^{(P)} e^{-ik_{2y}^{(P)} y} - C_4^{(P)} e^{ik_{2y}^{(P)} y} \right) \right] \\ & + \frac{(k_x^2 - (k_{ty}^{(P)})^2)}{(k_t^{(P)})^2} \left( C_5^{(P)} e^{-ik_{ty}^{(P)} y} + C_6^{(P)} e^{ik_{ty}^{(P)} y} \right), \end{aligned} \quad (3.13-2)$$

$$\begin{aligned} s^{(P)} = e^{-ik_x x} & \left[ \left( Q^{(P)} + b_1^{(P)} R^{(P)} \right) \left( C_1^{(P)} e^{-ik_{1y}^{(P)} y} + C_2^{(P)} e^{ik_{1y}^{(P)} y} \right) \right. \\ & \left. + \left( Q^{(P)} + b_2^{(P)} R^{(P)} \right) \left( C_3^{(P)} e^{-ik_{2y}^{(P)} y} + C_4^{(P)} e^{ik_{2y}^{(P)} y} \right) \right]. \end{aligned} \quad (3.13-3)$$

Similar to the elastic layers, the superscript (P) will be changed to  $(P_1)$  for the top porous layer, and to  $(P_2)$  for the bottom one.

### 3.3.4. Boundary conditions

The unknown coefficients can be determined from appropriate boundary conditions imposed at the interfaces of each layer. These conditions are stated below [25]:

I. Fluid-Solid interfacial interactions at  $y = 0$  and  $y_4$  :

$$i \omega u_y^{(E_{1,2})} = v_y^{(F_{1,2})}, \quad (3.14-1)$$

$$\sigma_{yy}^{(E_{1,2})} = -p^{(F_{1,2})}, \quad (3.14-2)$$

$$\sigma_{xy}^{(E_{1,2})} = 0, \quad (3.14-3)$$

II. Solid-Porous interfacial interactions at  $y = y_1$  and  $y_3$  :

$$u_x^{(E_{1,2})} = u_x^{(P_{1,2})}, \quad (3.15-1)$$

$$u_y^{(E_{1,2})} = u_y^{(P_{1,2})}, \quad (3.15-2)$$

$$u_y^{(E_{1,2})} = U_y^{(P_{1,2})}, \quad (3.15-3)$$

$$\sigma_{yy}^{(E_{1,2})} = (1-h^{(P_{1,2})})\sigma_{yy}^{(P_{1,2})} - h^{(P_{1,2})}s^{(P_{1,2})}, \quad (3.15-4)$$

$$\sigma_{xy}^{(E_{1,2})} = (1-h^{(P_{1,2})})\sigma_{xy}^{(P_{1,2})}, \quad (3.15-5)$$

III. Porous-Porous interfacial interaction at  $y = y_2$  :

$$u_x^{(P_1)} = u_x^{(P_2)}, \quad (3.16-1)$$

$$u_y^{(P_1)} = u_y^{(P_2)}, \quad (3.16-2)$$

$$h^{(P_1)}(u_y^{(P_1)} - U_y^{(P_1)}) = h^{(P_2)}(u_y^{(P_2)} - U_y^{(P_2)}), \quad (3.16-3)$$

$$\sigma_{yy}^{(P_1)} - s^{(P_1)} = \sigma_{yy}^{(P_2)} - s^{(P_2)}, \quad (3.16-4)$$

$$\sigma_{xy}^{(P_1)} = \sigma_{xy}^{(P_2)}, \quad (3.16-5)$$

$$h^{(P_1)} s^{(P_1)} = h^{(P_2)} s^{(P_2)}.$$

Eqs. (14) to (16) can be readily written in a matrix form as:

$$[\mathbf{M}]_{22 \times 22} [\mathbf{X}]_{22 \times 1} = [\mathbf{B}]_{22 \times 1}, \quad (3.17)$$

in which

$$[\mathbf{X}]^T = [C_1^{(E_1)} \dots C_4^{(E_1)} C_1^{(E_2)} \dots C_4^{(E_2)} C_1^{(P_1)} \dots C_6^{(P_1)} C_1^{(P_2)} \dots C_6^{(P_2)} I_R I_T], \quad (3.18)$$

where  $[\mathbf{X}]^T$  is the transpose of  $\mathbf{X}$ . Therefore, the reflected ( $I_R$ ) and transmitted ( $I_T$ ) sound intensities as a function of incident angle and frequency can be obtained by solving Eq. (3.18).

### 3.3.5. Diffuse sound transmission loss

Sound transmission loss is defined as [17]:

$$\text{STL(dB)} = 10 \log_{10} (1 / \tau), \quad (3.19)$$

where the sound transmission coefficient,  $\tau(\omega, \theta) = |I_T|^2 / |I_I|^2$ , is the ratio of the transmitted intensity to the incident intensity. Here the incident sound wave is considered to have a unit amplitude. In a diffuse field, it is required to consider an angle-averaged diffuse-field transmission coefficient (i.e.,  $\tau_d$ ), which the angular characteristics of the incident wave energy are taken into account, defined as [48]:

$$\tau_d = \frac{\int_0^{\pi/2} G(\theta) \tau(\omega, \theta) \cos \theta \sin \theta d\theta}{\int_0^{\pi/2} G(\theta) \cos \theta \sin \theta d\theta}, \quad (3.20)$$

where  $G(\theta) = e^{-\beta\theta^2}$  is the normalized Gaussian weighting function. For a perfect diffuse field,  $\beta = 2$  [49]. The integral equation in Eq. (3.20) can be numerically evaluated. Here, it should be

noted that the transmission loss cannot be determined exactly at  $\theta = \pi/2$  due to a singularity in the theory of elasticity [50].

### 3.3.6. Materials parameterization

A systematic approach for the aerogel material parameterization has been previously proposed and validated by the authors [12]. In this approach, all required material parameters for this class of PUA aerogels are estimated mainly based on the aerogel bulk density. Some physical characteristics such as skeletal density, average pore size diameter ( $L$ ) and Poisson's ratio ( $\nu$ ) of the aerogels are considered to remain unchanged with the variation of the aerogel bulk density. This assumption is mainly the outcome of the previous co-author's investigations on the physical behavior of the PUA aerogels at different bulk densities [5]. Table 3.1 lists the aerogel physical parameters that were used in this study.

Table 3.1. The PUA aerogel material parameters used in the present calculations.

Bulk density ( $\rho_b$ , g/cm <sup>3</sup> )	0.15	0.25
Skeletal density ( $\rho_s$ , g/cm <sup>3</sup> )	1.24	1.24
Porosity ( $h = (\rho_s - \rho_b) / \rho_s$ )	0.88	0.80
Average pore size diameter ( $\Gamma$ , nm)	40.33	40.33
Static Young's modulus ( $E_1 = 967.94\rho_b^{2.004}$ , MPa) <sup>1</sup>	22.20	61.78
Average Poisson's ratio ( $\nu$ )	0.22	0.22
Young's modulus loss factor ( $\eta$ ) <sup>2</sup> i.e., $E_1(1+i\eta)$	0.125	0.125
Geometrical structure factor ( $\varepsilon'$ ) <sup>2</sup>	1	1
Air flow resistivity ( $\sigma = 8\mu/\Gamma^2h$ , Ns/m <sup>4</sup> ) <sup>3</sup>	$1.03 \times 10^{11}$	$1.13 \times 10^{11}$

<sup>1</sup>Ref. [20]

<sup>2</sup>Ref. [30]

<sup>3</sup>Ref. [47]

The remaining material parameters are related to the gypsum and air. The gypsum material parameters and air properties are listed in Table 3.2.

Table 3.2. The gypsum and air material parameters used in the present calculations.

Gypsum bulk density ( $\text{g/cm}^3$ )	1
Gypsum Young's modulus (GPa)	2
Gypsum Poisson's ratio	0.33
Air density ( $\rho_0$ , $\text{kg/m}^3$ )	0.909
Speed of sound in air (m/s)	328.6
Shear viscosity ( $\mu$ , $\text{Ns/m}^2$ )	$1.84 \times 10^{-5}$
Prandtl number of air (Pr)	0.715
Ratio of air specific heats ( $\gamma$ )	1.2

### 3.4. Results and discussion

The morphology and the size distribution of the PUA aerogels are shown in Fig. 3.3. The SEM images reveal a nano-fibrous structure for both  $0.15 \text{ g/cm}^3$  (Fig. 3.3a) and  $0.25 \text{ g/cm}^3$  (Fig. 3.3c). The pore structures are highly random in both samples. However, the structure for higher bulk density aerogel is relatively more packed in comparison with the lower density sample. This leads to a lower porosity for a higher bulk density sample in agreement with our previous porosity estimations using skeletal and bulk densities. Higher resolution images are also provided as onsets of the SEM images. The fiber diameter distributions are also obtained for both samples as shown in Figs. 3b and 3d. The average diameter for the higher bulk density sample is lower and more uniformly distributed over the sample which indicates the consistency of the synthesis protocol.

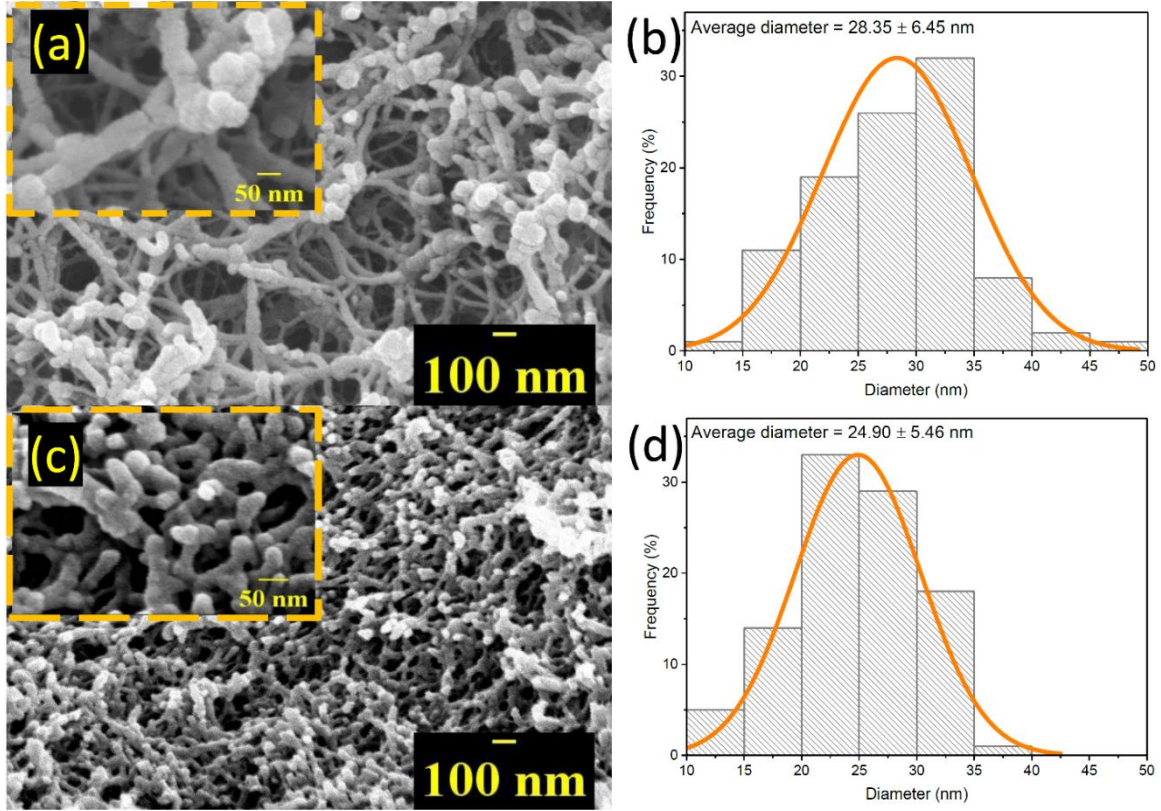


Figure 3.3. (a) and (c) The SEM images of the PUA aerogels at bulk densities  $0.15 \text{ g/cm}^3$  and  $0.25 \text{ g/cm}^3$ , respectively; (b) and (d) The fiber diameter size distributions of the PUA aerogel networks at bulk densities  $0.15 \text{ g/cm}^3$  and  $0.25 \text{ g/cm}^3$ , respectively.

The airborne STL values for the two sets of samples at the frequency range of 100 to 5000 Hz are obtained within an ASTM E90 test chamber. The results for the  $1 \text{ m}^2$  sample set are shown in Fig. 3.4. A significant increase can be seen over the entire frequency range, remarkably at 4 kHz with more than 15 dB, due to the aerogel constraint layers. The dip in the STL values of the gypsum-only panel at 4 kHz can be explained using thin plate theory [28]. According to this theory, for an unbounded flexible partition, at a certain frequency, the incident wave is coincident with the bending wave in the partition. This coincidence frequency ( $f_c$ ) is approximated as [28]:

$$f_c = \frac{c_0^2}{2\pi \sin^2 \theta} \sqrt{\frac{\rho t_0}{D}}, \quad (3.21)$$

where  $D = E_0 t_0^3 / 12(1 - \nu_0^2)$ , is the partition's bending stiffness with  $E_0$ ,  $\nu_0$  and  $t_0$  being Young's modulus, the Poisson's ratio and the thickness of the partition, respectively. Using Eq. (3.21), the estimated coincidence frequencies for an unbounded gypsum panel at incident angles less than  $90^\circ$  are entirely above 2000 Hz. Consequently, the dip at 4 kHz in the experimental values of the STL can be correlated to the lowest coincidence frequency of the gypsum only partition. Therefore, one can say that the aerogel implementation not only caused the corresponding coincidence effect to be disappeared but also increased the STL values from 30 dB to 45 dB at this frequency. It should be also emphasized that this unusual enhancement was obtained only with a 20% increase in the overall mass of the test sample. The STL enhancements at different frequencies are listed in Table 3.3. This finding opens a door to various applications where high STL is required.

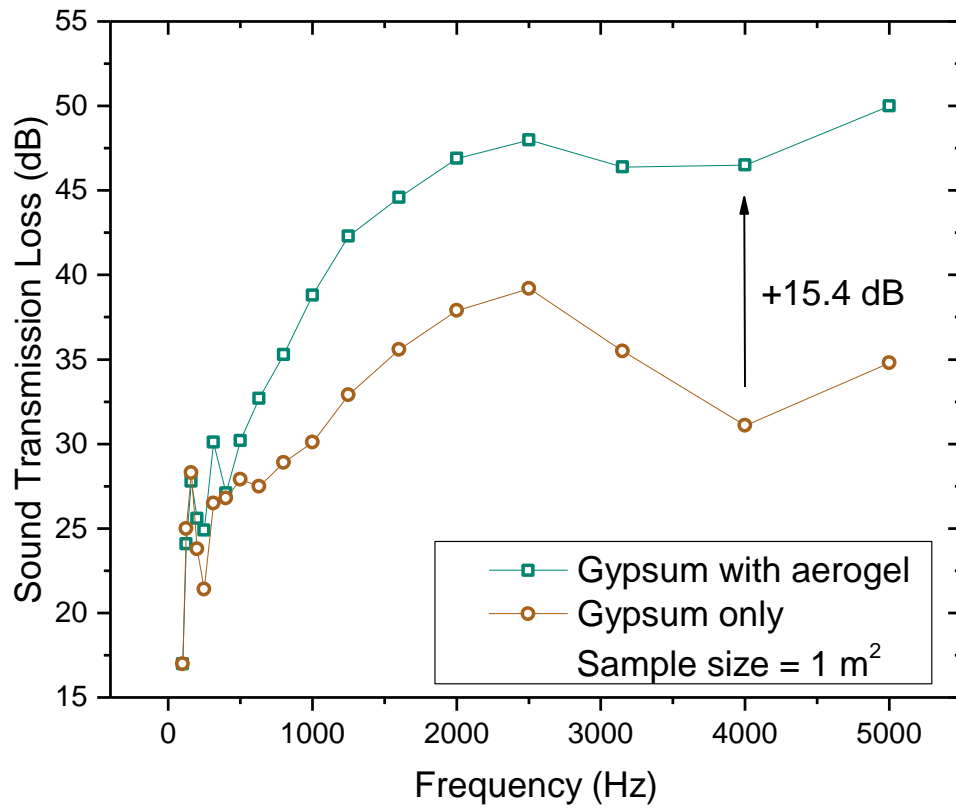


Figure 3.4. The effect of PUA aerogels on the airborne STL values of 1 m<sup>2</sup> sample as a function of frequency.

Table 3.3. The STL values and enhancements (STL-E) at different frequencies and the sound transmission classes (STC) of gypsum and gypsum-aerogel composite panels, all in dB, at different sizes.

<b>Freq. (Hz)</b>	<b>STL</b>		<b>STL-E<sup>1</sup></b>	<b>STL</b>		<b>STL-E</b>
1000	30.1	38.8	8.7	27.7	39.9	12.2
2000	37.9	46.9	9.0	35.6	47.3	11.7
3150	35.5	46.4	10.9	34.2	45.1	10.9
4000	31.1	46.5	15.4	31.7	44.9	13.2
5000	34.8	50	15.2	35.2	47.4	12.2
<b>STC<sup>2</sup></b>	31	36	-	28	34	-
<b>Panel</b>	Gypsum (1 m <sup>2</sup> )	Composite (1 m <sup>2</sup> )	-	Gypsum (10 m <sup>2</sup> )	Composite (10 m <sup>2</sup> )	-

<sup>1</sup>STL-E = STL (Composite) - STL (Gypsum)

<sup>2</sup>In compliance with ASTM E413; [51].

In order to further validate and better capture the actual physical effects of the aerogels, the finite boundary effects including sample in-place mounting mechanisms and sample frame holder effects must be minimized. One way to accomplish this is to provide a bigger test sample. Therefore, through a systematically consistent experiment with previous trials, another experiment was carried out to measure the airborne STL values of a 10 m<sup>2</sup> test sample. Since the incidence area of this set is 10 times bigger than the first set, we can expect that all boundary effects should be minimized and therefore we can capture the true core effects and obtain a more realistic environmental test situation. The obtained STL results of the 10 m<sup>2</sup> gypsum-only and gypsum-aerogel composite samples are depicted in Fig. 3.5. Interestingly, the results for both 1 m<sup>2</sup> and 10 m<sup>2</sup> test sets are containing very similar trends that prove the consistency and high reproducibility

of the executed material preparation and acoustic test methods. The size insensitivity of the STL enhancement due to the low-density aerogel layers confidently provides several potential advanced engineering applications for these hierarchical class of materials (check Table 3.3).

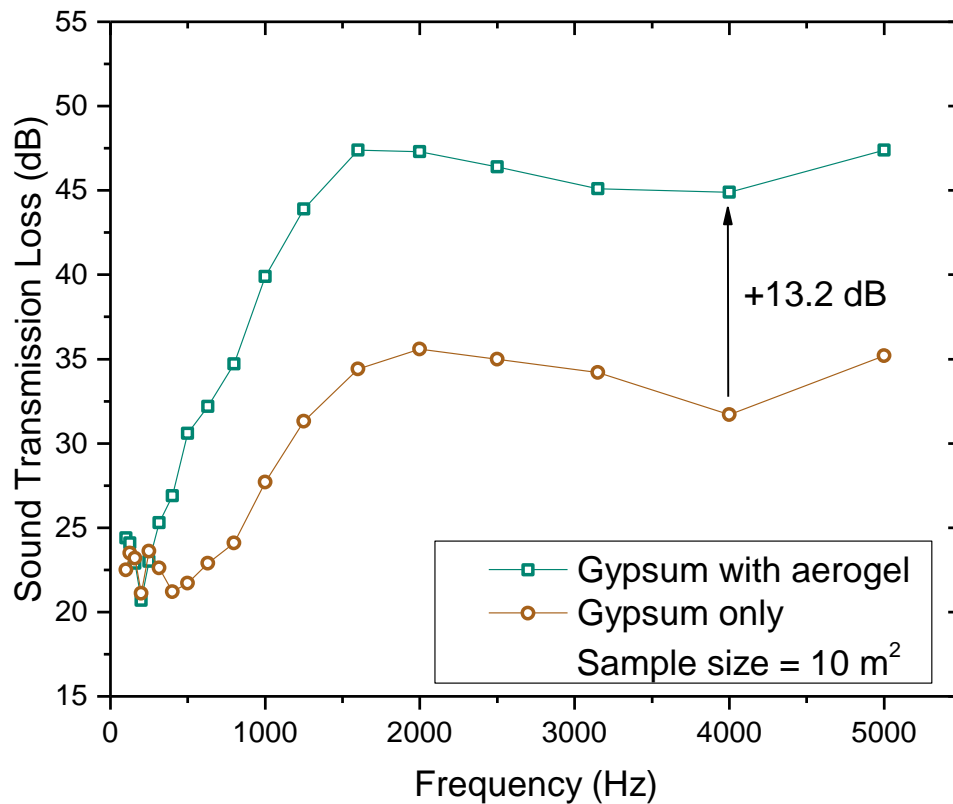


Figure 3.5. The effect of PUA aerogels on the airborne STL values of 10 m<sup>2</sup> samples as a function of frequency.

We have previously shown the feasibility of the Biot’s dynamic poroelasticity on the modeling of the normal incidence STL of the single-layer PUA aerogels at different bulk densities [12]. In order to recheck the applicability of Biot’s theory on the wave propagation problems including the aerogel materials, here the modeling methodology was extended to a multilayered composite material with the help of the theory of elasticity and acoustics field theory. The two-dimensional plane strain analytical solution along with the experimental airborne STL values for both 1 and 10 m<sup>2</sup> layered composite samples are shown in Fig. 3.6. The analytical results provide an excellent

agreement with the experimental results over the entire frequency range, reassuring the feasibility of this technique to model the aerogel-based dynamic systems and structures. It is worth mentioning that the typical porous material parameterizations are rigorously experimentally involved in order to reach meaningful results in comparison with experiments, However, in this research, a relatively simple and straightforward material parameterization approach has been taken into account which was mainly limited to the bulk density and Young’s modulus measurements. Therefore, the theory-experiment agreement in this work on the wave propagation properties of the layered composites can be considered as a parameter sensitivity analysis for other material parameterization techniques.

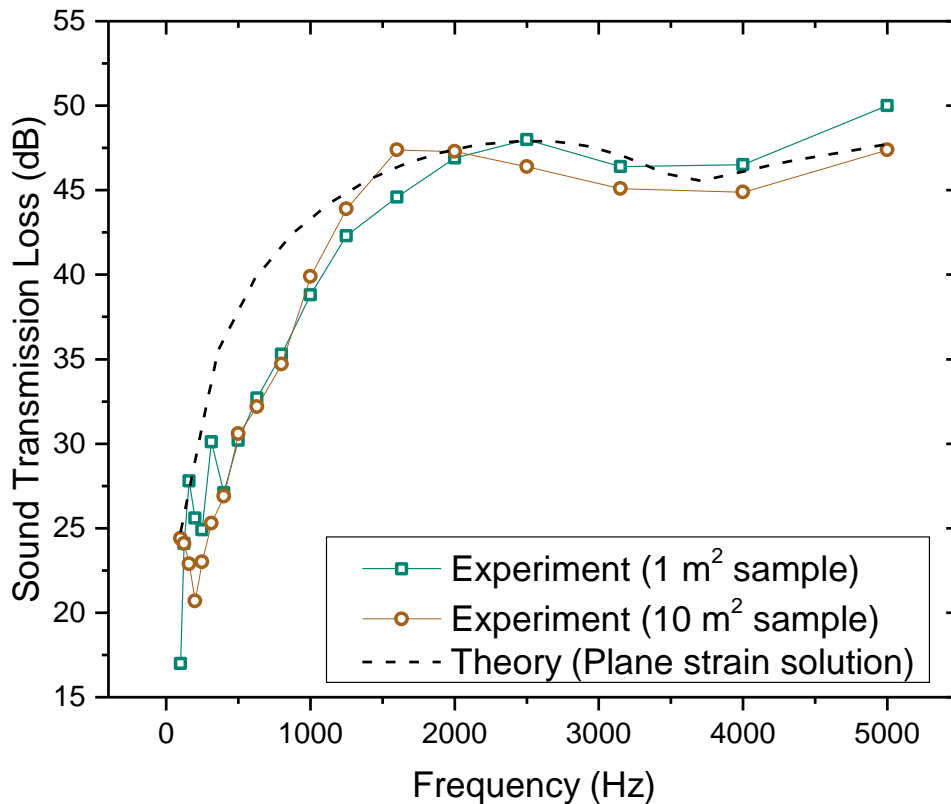


Figure 3.6. The comparison between the plane strain theoretical solution with experimental airborne STL values of gypsum-aerogel composite samples as a function of frequency at different sizes.

Relying on the predicted analytical results, the effects of average core bulk density on the insulation properties of the layered composites were investigated and results are shown in Fig. 3.7. The bulk density ratio of the two aerogel layers was kept to 1.5 for all calculations and results are depicted as a function of frequency at different average aerogel bulk density. Such calculation is necessary for the purpose of design and optimizations. The average core density was effective on the low-frequency range while significant variations can be seen at frequencies above 1 kHz. The most noticeable effect is the change in the position of the coincidence frequency. By increasing the core density, the coincidence frequency is decreasing. This decrease is associated with the increase in the overall bending stiffness of the composite with increasing the core bulk density, check Eq. (3.21).

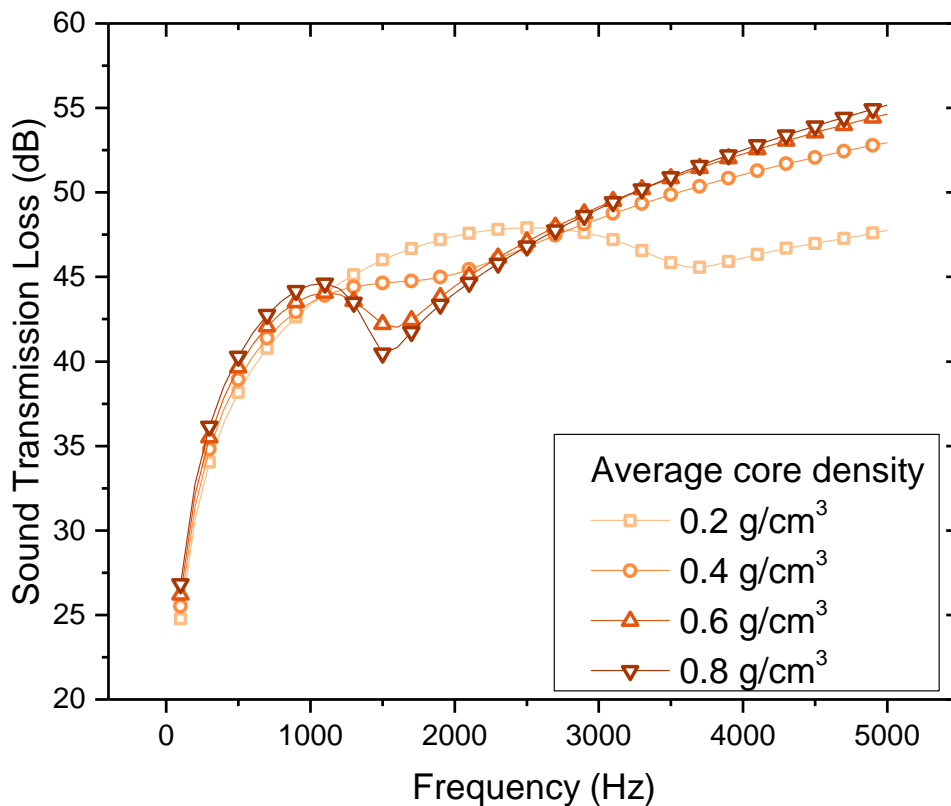


Figure 3.7. Airborne STL of an unbounded aerogel-gypsum layered composite as a function of frequency at different average core bulk densities (the ratio of the two aerogel bulk densities was kept to 1.5).

### 3.5. Conclusions

In this work, an inorganic-organic layered composite comprising low-density nanoporous PUA aerogels with gypsum material was considered. Within two independent sets of experiments, the chamber-based airborne STL of the composite samples were measured. The constraint effects of the aerogel layers were studied in both experiments and the results demonstrated consistently a significant increase in the airborne STL of the layered composite structures. Due to the slight structural weight change by applying the low-density multifunctional PUA aerogels, this uncommon STL enhancement clearly breaks the empirical mass law in the sound insulation behavior of conventional acoustics materials. Owing to their low thermal conductivity, low-cost

and facile molding and machining of this type of organic aerogel materials, it is envisioned that they will become attractive at several advanced engineering scenes where extreme sound and/or heat insulations are required. Finally, a 2D plane strain analytical solution was provided to model the wave propagations through the layered composite material. Excellent agreement with the experimental observations was obtained that shows the applicability of the proposed methodology for the aim of design and optimization of similar hierarchical and future low-density aerogel based dynamic applications and technologies.

## CHAPTER 4

### SCALABLE, HYDROPHOBIC AND HIGHLY-STRETCHABLE

#### POLY(ISOCYANURATE-URETHANE) AEROGELS

Scalable, low-density and flexible aerogels offer a unique combination of excellent mechanical properties and scalable manufacturability. Herein, we report the fabrication of a family of low-density, ambient-dried and hydrophobic poly(isocyanurate-urethane) aerogels derived from a triisocyanate precursor. The bulk densities ranged from 0.28 to 0.37 g/cm<sup>3</sup> with porosities above 70% v/v. The aerogels exhibit a highly stretchable behavior with a rapid increase in Young's modulus with bulk density (slope of log-log plot > 6.0). In addition, the aerogels are very compressible (more than 80% compressive strain) with a high shape recovery rate (more than 80% recovery in 30 sec). Under tension even at high strains (e.g., more than 100% tensile strain), the aerogels at lower densities do not display a significant lateral contraction and have a Poisson's ratio of only 0.22. Under dynamic conditions, the properties (e.g., complex moduli and dynamic stress-strain curves) are highly frequency- and rate-dependent, particularly in the Hopkinson pressure bar experiment where in comparison with quasi-static compression results, the properties such as mechanical strength were three orders of magnitude stiffer. The attained outcome of this work supports a basis on the understanding of the fundamental mechanical behavior of a scalable organic aerogel with potentials in engineering applications including damping, energy absorption, and substrate for flexible devices.

#### 4.1. Introduction

Aerogels are low-density nanoporous solids containing hierarchical three-dimensional networks of nanoparticles pursued primarily for thermal and acoustic insulations and often for functionalization purposes [2]. Typically, they are prepared from a sol-gel process by supercritical drying of a suitable wet gel [36]. Silica aerogel, as a classical example of a nanostructured porous material, is the most common type of aerogels [38]. However, silica aerogel is suffering from severe structural fragility and high production cost (some attempts have been made to reduce its synthesis cost, e.g., [52]), which limits its applications [38]. The problem of fragility has been

successfully addressed with introducing polymer cross-linked silica aerogels, known as X-aerogels, which contains a post-gelation cross-linking of the silica nanoparticles with a thin polymeric coating [37]. This technology could dramatically improve the mechanical properties of X-aerogels such as mechanical strength and fracture toughness, by a factor of 100 and more with respect to the pristine silica aerogel.

However, this post-gelation process is further adding to the overall production cost of the aerogels. Owing to the substantial improvement in the mechanical properties of X-aerogels with a small amount of polymeric cross-linking agent, it was postulated and later confirmed to consider purely polymeric aerogels with similar X-aerogel nanostructures. For that reason, various polymeric aerogels from different polymeric sources such as polyurea[5], polyurethane [6], polyimide [7] and polyamide (Kevlar<sup>TM</sup>-like) [8] have been synthesized. Pure polymeric aerogels resulted in the emergence of new applications such as ballistic armor protection[9].

Another major obstacle to the aerogel commercialization is the need for supercritical drying. Adopting a scalable nano-manufacturing process to make a balanced combination between the low-density and good mechanical properties without any limitation on the size and dimensions of the product is necessary. Accordingly, the primary intent of this work is to emphasize on the low density nanoporous *ambient pressure-dried* polymeric aerogels, which would have a lower production cost than their supercritical-dried counterparts due to their scalability. Moreover, the mechanical properties of X-aerogels are well investigated (e.g., [53–61]) while the polymeric aerogels, specifically those that were prepared under ambient conditions, are less studied (e.g., [5,62,63]).

Recently, our co-author has studied a family of supercritical-dried poly(isocyanurate-urethane) aerogels with shape memory capability using a triisocyanate derivative of aliphatic hexamethylene diisocyanate (N3300A) and variable-length derivatives of ethylene glycol (EG) diols[64]. Using longer EG-derived diols (e.g., triethylene glycol or tetraethylene glycol), it was shown that the molecular slippage and macroscopic creep for the obtained aerogels are noticeably reduced due to higher hydrogen bonding possibilities between the neighboring urethane branches. Specifically, the triethylene glycol (TEG) based aerogel samples showed an excellent super-elasticity over a

wide range of tensile strains. This promising behavior can be exploited at different engineering applications, where high material recovery and vibration damping are required.

Therefore, in this work, using N3300A as precursor and TEG as diol, the poly(isocyanurate-urethane) aerogels are synthesized at low-density with hydrophobic surface properties under ambient conditions to contribute on the synthesis scalability. Subsequently, the thermo-mechanical properties of the obtained aerogels are systematically characterized under both quasi-static (uniaxial tensile and compression testing and dynamic mechanical analysis) and high strain-rate (split Hopkinson pressure bar) loading conditions to consider the realistic service life situations for the synthesized aerogels.

## 4.2. Results and discussion

### 4.2.1. Synthesis and chemical characterization

The general protocol of the synthesis is adopted from our co-author's recent publication[64]. Fig. 4.1 shows the synthesis protocol and the reaction pathway to the isocyanurate cross-linking urethane aerogels. Monomers were used at their stoichiometric amounts (triisocyanate:diol = 2:3 mol/mol). Sols were prepared in pure  $\text{CH}_3\text{CN}$  at room temperature. The total monomer concentration was varied between 12% and 15% w/w. The urethane formation was catalyzed by dibutyltin dilaurate (DBTDL) in different amounts varied from 1:22 to 1:38 mol/mol ratios relative to N3300A. The exact chemical amounts are tabulated in Table S.1 in [14]. Prior to gelation, the sols were stirred for 15 min at room temperature. After stirring, the sols were poured into an aluminum mold, coated with a thin layer of silicon rubber, and covered for gelation followed by aging processes, all at room conditions. The samples were monitored every 10-15 min in order to determine the gelation times, and then all samples were aged for 24 h. After aging, wet gels were removed from the molds and washed with a stirred mixture of acetone and a small amount of hexylamine (0.3% v/v) for 8 h. Then, the wet gels were washed with pure acetone for 5 times, each for 8 h and finally washed with pentane for another 8 h. The washed wet gels were then dried under ambient conditions. Finally, the samples (i.e., PU aerogels) were heated up in the oven at 40 °C for 3 h for further stabilization.

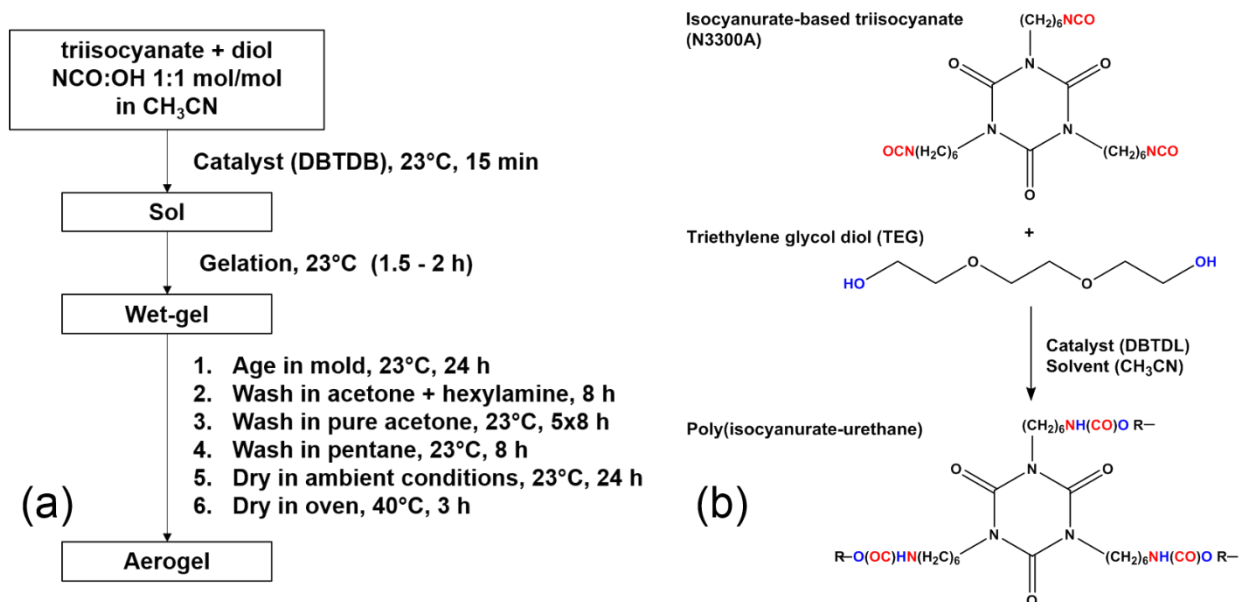


Figure 4.1. (a) Synthetic protocol of the PU aerogels; (b) Reaction pathway to isocyanurate cross-linking urethane aerogels.

The chemical compositions of the synthesized samples were confirmed with solid-state CPMAS  $^{13}\text{C}$  NMR (Fig. 4.2). It is worth mentioning that the expected  $\text{N}^{13}\text{CO}$  resonance peak of the isocyanate at 122 ppm is missing at the NMR spectrum which indicates the completeness of the reaction. The resonance peaks at 149.3 and 156.3 ppm were associated with the isocyanurate and the urethane carbonyl ( $-\text{NH}(\text{C}=\text{O})\text{O}-$ ), respectively. The next two peaks at 61.3 and 70.2 ppm were associated with the aliphatic carbons of the diol. The remaining peaks at 27.5 and 42.6 ppm were associated with the  $-\text{CH}_2-$  groups of N3300A.

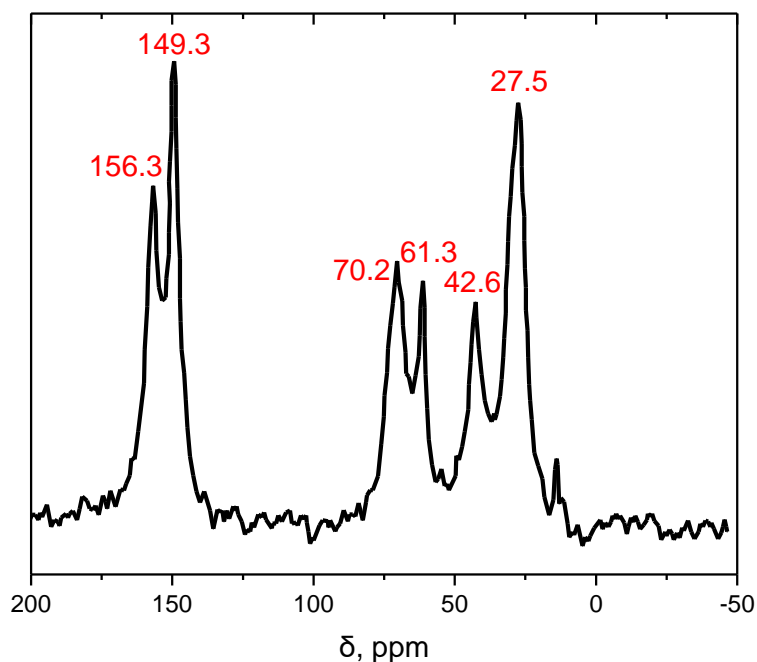


Figure 4.2. Typical solid-state CPMAS  $^{13}\text{C}$  NMR spectrum of the aerogel.

#### 4.2.2. General material properties

The general material properties are summarized in Table 4.1. Different monomer concentrations led to four distinct densities, ranging from 0.28 to 0.37 g/cm<sup>3</sup>. The linear shrinkage of the samples relative to the mold size (i.e., the diagonal of the rectangular mold) is between 21 to 25%. All samples' shrinkage happened only during the drying process, which dismisses any probable post polymer reorganization assumptions during the solvent exchanges. The BET surface areas show a drop with an increase in bulk density, which agrees with the increase in the aerogel particle sizes. The samples' quality in shape recovery from a sudden contraction was studied by measuring the recovery speed of a cylindrical sample (same dimensions as the compression samples). All samples approximately expanded on a similar quality with an approximate recovery speed of ~1 mm/s for 80% of the initial contraction.

Table 4.1. The bulk density, porosity, linear shrinkage, recovery speed and glass transition temperature ( $T_g$ ) data of the synthesized aerogel samples.

Name	Bulk Density ( $\rho_b$ , g/cm <sup>3</sup> )	Porosity (%) <sup>a</sup>	Linear Shrinkage (%) <sup>b</sup>	BET Surface Area, (m <sup>2</sup> g <sup>-1</sup> ) <sup>c</sup>	Recovery Speed (mm/s) <sup>d</sup>	DSC T <sub>g</sub> (°C) <sup>e</sup>
PU 1	0.28 ± 0.01	77.20 ± 0.95	24.54 ± 0.56	0.86	0.91	17
PU 2	0.30 ± 0.01	75.58 ± 0.94	23.64 ± 0.60	0.45	0.99	22
PU 3	0.35 ± 0.02	71.50 ± 1.69	22.02 ± 0.55	0.35	1.33	22
PU 4	0.37 ± 0.02	69.88 ± 1.69	22.48 ± 0.71	0.30	1.33	23

Five measurements were made unless otherwise indicated. Skeletal Density ( $\rho_s$ ) is considered to be  $1.23 \pm 0.005$  gcm<sup>-3</sup> [64]. <sup>a</sup>Porosity =  $100 \times [(\rho_s - \rho_b) / \rho_s]$ . <sup>b</sup>Linear Shrinkage =  $100 \times [(\text{Mold diagonal} - \text{Sample diagonal}) / \text{Mold diagonal}]$ . <sup>c</sup>Single measurement. <sup>d</sup>80% shape recovery; single measurement. <sup>e</sup>Single measurement.

The obtained rectangular-shape samples were highly flexible. Fig. 4.3a-c show the typical bending flexibility for one of the samples at 0.28 g/cm<sup>3</sup> density. The morphology of the samples was also studied with SEM and the images are shown in Fig. 4.3d and e. Due to the similar trend, morphologies at only two densities (0.28 and 0.37 g/cm<sup>3</sup>) are shown here (check Figure S.1 in [14] for SEM images at all densities). The microstructural evolution with density (i.e., with more concentrated sols) was attributed to spinodal decomposition in combination with slower vs. faster gelation: lower concentration sols (yielding aerogels with densities at 0.28 g/cm<sup>3</sup>) gelled in longer times, 120 min, giving time to the phase-separated polymer to undergo spheroidization. Higher concentrations sols (yielding aerogels with densities at 0.37 g/cm<sup>3</sup>) gelled faster (90 min) and the observed microstructures were closer to bicontinuous. To induce hydrophobicity, the surfaces of the gels were modified by including a low concentration of hexylamine in the first wash in acetone. Waterdrop contact angles at different hexylamine concentrations were measured using a

goniometer (check Figure S.2 in [14]). It was found that the contact angle of a water droplet with the gel surface (i.e.,  $\sim 78^\circ$  without modification) was increased to  $130^\circ$  with 0.3% v/v concentration as shown in Fig. 4.3f. Hydrophobicity in aerogels is crucial at the full commercialization phase. It should be noted that the low concentration for the hexylamine is also important since it might affect the gel permeability in solvent exchange followed by drying phases.

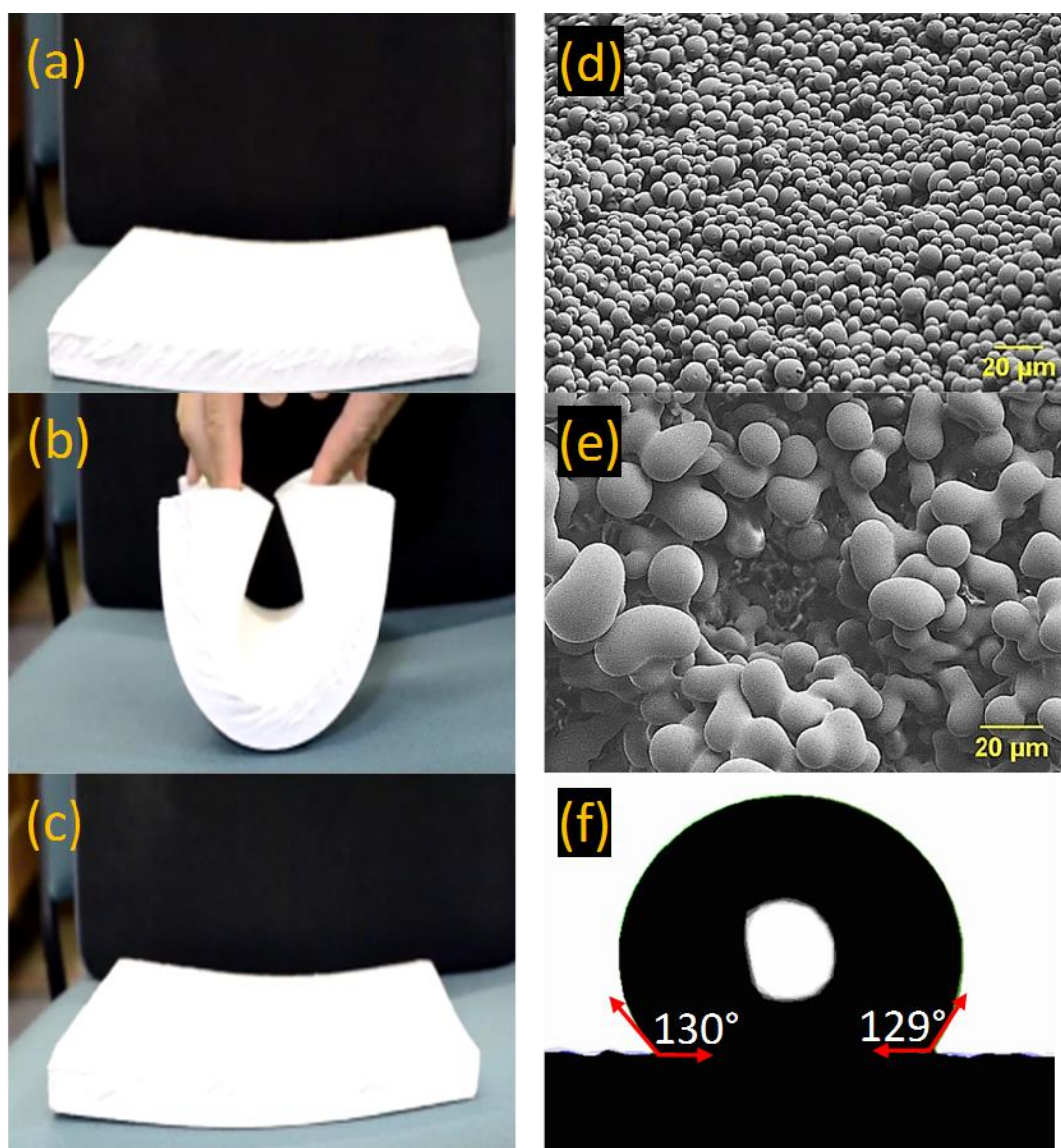


Figure 4.3. Typical flexible PU aerogel panel at (a) original, (b) deformed and (c) final shapes at bulk density  $0.28 \text{ g/cm}^3$ ; (d) and (e) SEM images of the PU aerogels at bulk densities  $0.28 \text{ g/cm}^3$  and  $0.37 \text{ g/cm}^3$ , respectively; (f) Waterdrop contact angles on the surface of the PU aerogel at bulk density  $0.28 \text{ g/cm}^3$ .

Glass transition temperatures ( $T_g$ ) and material degradation with respect to heat in the PU aerogel samples were then studied through Differential Scanning Calorimetry (DSC) and Thermogravimetric (TGA) analyses and the results for the lowest and highest densities are plotted in Fig. 4.4 (check Figs. S.3 and 4 in the [14] for all densities). The  $T_g$  of all samples (which are

also tabulated in Table 4.1) are either at or below the room temperature (i.e.,  $\sim 23\text{ }^{\circ}\text{C}$ ). Therefore, as expected, all samples are at their rubbery states, which boost their room temperature super-elasticity. Meantime, the TGA results show that all samples are equally resistant to heat and starting to lose mass at about  $350\text{ }^{\circ}\text{C}$ . Up to  $350\text{ }^{\circ}\text{C}$ , only less than 5% mass-loss, at maximum, was observed for the aerogels. The main decomposition (i.e., more than 90%) occurs between  $350$  to  $500\text{ }^{\circ}\text{C}$ .

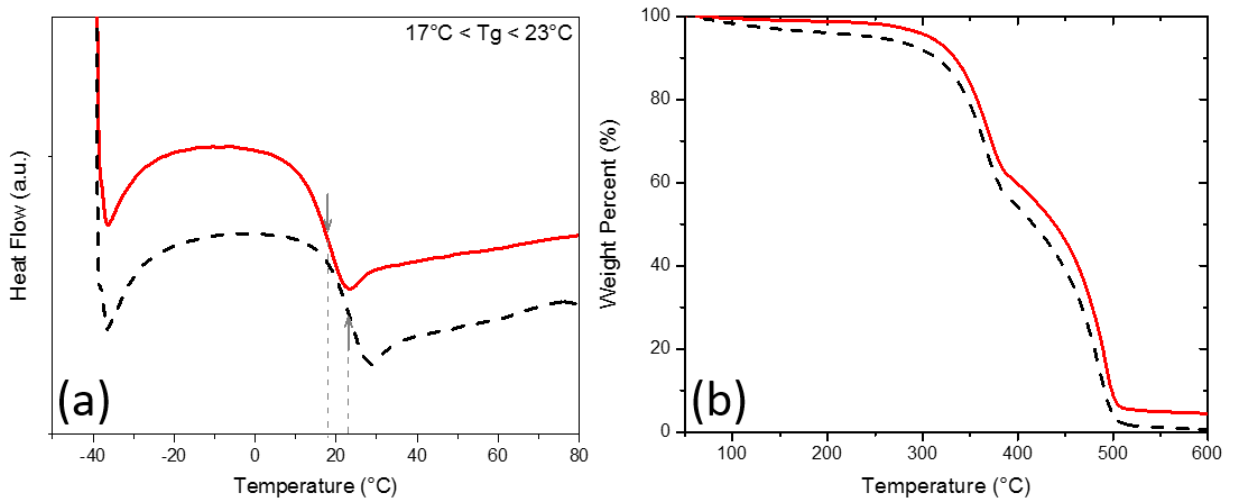


Figure 4.4. (a) Differential scanning calorimetry and (b) Thermogravimetric analysis of PU aerogels at bulk densities  $0.28\text{ g/cm}^3$  (solid line) and  $0.37\text{ g/cm}^3$  (dash line).

#### 4.2.3. Mechanical characterization

Mechanical behavior of the obtained aerogels was investigated through different configurations including quasi-static (e.g., tensile, compression and dynamic mechanical analysis) and high strain-rate loading conditions (i.e., a split Hopkinson pressure bar experiment). Under quasi-static loading conditions (i.e., strain rate was set less than  $0.001\text{ s}^{-1}$ ), Fig. 4.5a shows the typical quasi-static uniaxial tensile test data at room temperature for the aerogel samples at different densities. Linear-elastic behavior is observed for all samples over a wide-range of uniaxial strain (i.e., up to 120% strain). Due to the limited gauge length of the uniaxial tensile test setup (i.e., MTI tensile tester), higher strains than 120% strain was not possible. The variation of Young's modulus versus bulk density at room temperature is shown in Fig. 4.5b. The slope of the log-log trend line (i.e.,

dash line) is calculated to be more than 6, which shows a rapid increase in the modulus with the increase in the density. Digital Image Correlation (DIC) technique concurrent with the tensile tests has been also carried out to measure the 2D displacement and strain fields to obtain the Poisson's ratios of the aerogels. The real-time strain fields along X and Y directions of the aerogel at 0.28 g/cm<sup>3</sup> are demonstrated as an example in [14] (i.e., Movie S.1 in [14]). The Young's moduli and Poisson's ratios of the aerogels are tabulated in Table 4.2. It is worth mentioning that the aerogels at lower densities have low Poisson's ratio of 0.22, which is indicative of a small lateral contraction during the tension process. In contrast, at higher densities, the Poisson's ratio is also higher to its ultimate value of 0.48 at a bulk density of 0.37 g/cm<sup>3</sup>. Also, the wave speed in the aerogels has been estimated using Young's modulus and bulk density data. The estimated values (11 – 27 m/s) are much lower than the speed of sound in open dry air at 20 °C (343 m/s), inferring that the aerogels are expected to be also a good sound attenuator.

Table 4.2. Room temperature quasi-static Young's modulus, Poisson's ratio and speed of wave propagation data of the synthesized aerogel samples.

Name	Young's Modulus (kPa)	Poisson's Ratio	Wave Speed (m/s) <sup>a</sup>
PU 1	37.86 ± 5.24	0.22 ± 0.01	11.63
PU 2	100.90 ± 18.82	0.22 ± 0.01	18.34
PU 3	163.02 ± 11.54	0.35 ± 0.01	21.58
PU 4	265.19 ± 13.40	0.48 ± 0.02	26.31

$$^a\text{Wave speed} = \sqrt{\text{Young's Modulus/Bulk Density}}.$$

In addition to the tensile test, different cyclic compression scenarios have been tested on the aerogels. Due to similar behaviors, only the lowest and highest density samples were considered for these tests. At first, in order to assess the aerogels' stability and resilient property under cyclic loadings, cyclic loading-unloading compression test at 50% strain was conducted and results for two densities are shown in Figs. 4.5c and d. For each cycle, the starting point is the same and equal to the initial sample length. Therefore, for both densities, a decent strain recovery can be shown

after finishing a cycle and before starting of the next one. The main drop in the stress at both densities occurs after the first cycle mainly due to possible crack initiations. The remaining drops can be associated to the dissipations due to microstructural buckling, adhesion, and friction between polymeric branches and further crack formation. Quantitatively, energy dissipation and maximum stress at each cycle can be considered as the key functions for the aerogels' energy absorption capabilities (see Figs. 4.5e and f). The patterns of maximum stress at both densities are very similar, where after five consecutive cycles, the values are nearly 10 and 45 kPa for low and high-density aerogels, respectively. The normalized absorption energies with respect to the first cycle absorption energy are shown in Fig. 4.5f. Similar to the maximum stress behavior, the energy dissipation behavior at consecutive loading cycles for both densities are fairly similar. The low-density sample stays at ~60% of its initial dissipation capability, after five consecutive cycles, while the high-density sample at ~80% of its first cycle. It is worth mentioning that the first cycle dissipation energy was tripled with only a 25% increase in the bulk density of the aerogels (see Fig. 4.5f).

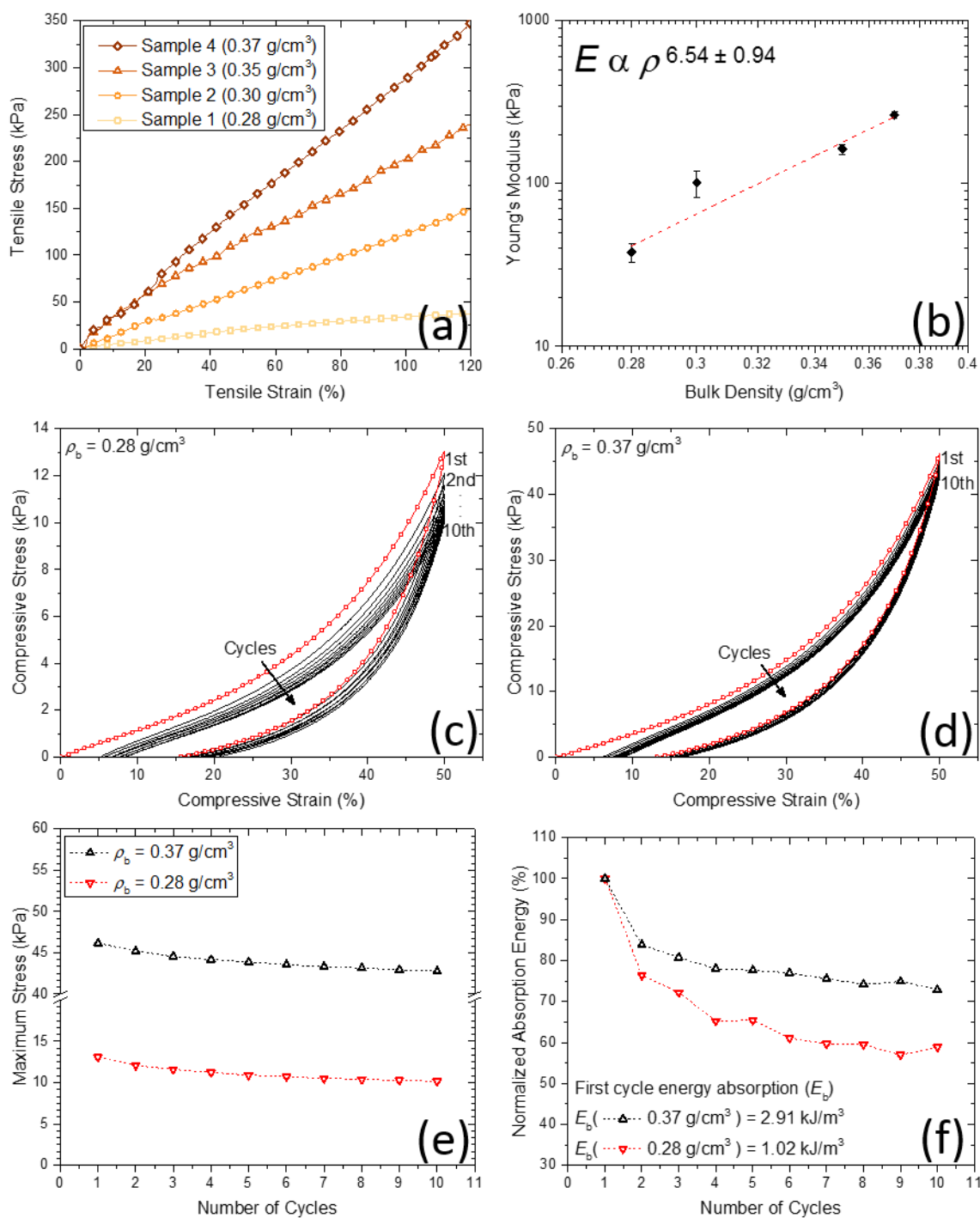


Figure 4.5. (a) Typical quasi-static uniaxial tensile stress-strain responses of PU aerogels at different bulk densities; (b) Power-law relationship of Young's modulus with bulk density of the PU aerogels ; (c) and (d) Cyclic quasi-static load-unload compression testing at 50% strain of PU aerogels at bulk densities 0.28 and 0.37

$\text{g/cm}^3$ , respectively; (e) Maximum stress and (f) Normalized absorption energy during 10 consecutive cycles for PU aerogels at bulk densities 0.28 and 0.37  $\text{g/cm}^3$ .

In the next compression experiment, the samples are compressed at four-stepped cycles at different strain amplitudes of 20, 40, 60 and 80% in sequence. In contrast with the previous compression test, the starting point of each cycle is at the end of the unloading part of the pervious cycle. Figure 4.6 shows the stress-strain curves of the PU aerogels with loading-unloading-reloading cycles at bulk densities 0.28 and 0.37  $\text{g/cm}^3$ . A nonlinear recovery can be shown for all unloading curves. A decent recovery even at 80% strain exists for the PU aerogels especially at bulk density 0.37  $\text{g/cm}^3$ , which indicates a high level of compressibility for this class of aerogels. Each succeeding loading curve rises back to the maximum stress point of the preceding cycle, indicating a strong strain memory effect in the aerogels. Additionally, due to this memory effect, a negative slope (stiffness) for the stress-strain curve at the beginning of each unloading zone can be observed. The reloading curves do not follow the loading curves, resulting in a hysteresis loop for each cycle. Both samples started to experience the densification effects at higher strain levels (i.e., ~ above 70% strain).

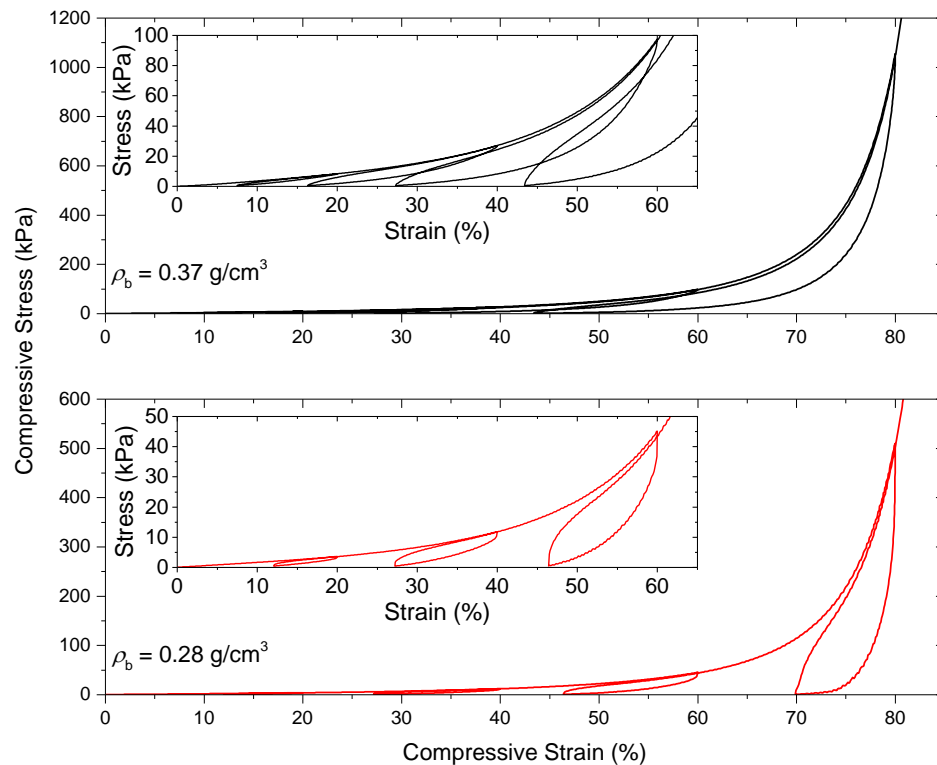


Figure 4.6. Quasi-static load–unload-reload compression testing of PU aerogels at bulk densities of 0.28 and 0.37 g/cm<sup>3</sup>.

Complex modulus and loss tangent of the PU aerogels using Dynamic Mechanical Analysis (DMA) in compression mode were studied at different temperatures and frequencies (Fig. 4.7). As it is expected, the high-density sample has a higher complex modulus than the low-density sample. The modulus difference is more noticeable at low temperatures, where the materials are stiff (e.g., high-density storage and loss moduli are about 3 and 10 times higher than low-density corresponding values at -50°C, respectively). At low temperatures, both storage and loss moduli are about 1000 times higher than their respective high-temperature values for both densities. Also, storage moduli are about 100 times bigger than the loss moduli at all temperatures for both densities. Moreover, Fig. 4.7c indicates the loss tangent (i.e., the ratio of loss modulus to storage modulus) behavior of the samples at different temperatures and frequencies with a peak corresponding to the glass transition temperature (i.e., DMA T<sub>g</sub>). Here, multi-frequency analysis allows one to study the glass transition shift in the aerogel samples. Generally, the DMA T<sub>g</sub>s are in agreement with DSC T<sub>g</sub>s. The DMA T<sub>g</sub>s are shifting to higher temperatures with increasing

frequency. At higher frequencies, the molecular relaxations can only occur at higher temperatures, which means glass transition should start at higher temperatures as well. The  $T_g$  has increased by about  $5^\circ\text{C}$  at both densities with a frequency increase from 1 to 10 Hz.

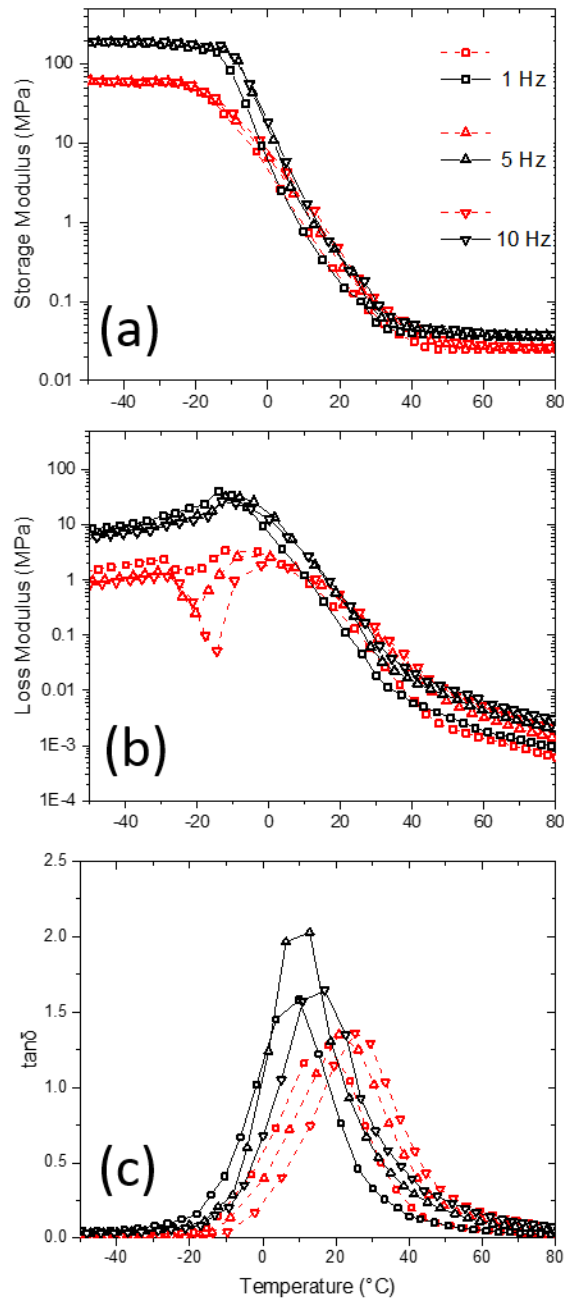


Figure 4.7. Dynamic mechanical analysis in compression mode (a: storage modulus, b: loss modulus, and c: tan delta) of PU aerogels at bulk densities 0.28 (dash line) and 0.37 (solid line) g/cm<sup>3</sup> at different temperatures and frequencies.

High strain-rate mechanical properties of the aerogels have been also studied by means of a long split-Hopkinson pressure bar (SHPB) under ambient conditions. Specifically, the effects of different strain rates on the stress-strain curves of aerogels at two different densities were considered. Fig. 4.8 shows the compressive stress-strain curves of PU aerogels at high strain rates. It is notable that each stress-strain curve in Fig. 4.8 represents the mean value of six experiments at strain rates close to the target strain rates (a reproducible identical strain rate is a very difficult task in SHPB experiment). The actual experimental data at different strain rates are depicted in Fig. S5 of [14]. A dramatic change in the stress-strain relationships of the aerogels at both densities is observed at different strain-rates. The general compressive behavior contains an initial linear elastic region, followed by yielding (which does not exist at the quasi-static responses) and hardening associated with the compaction of material pores. The aerogel's Young's modulus, strength and maximum strain reached in each experiment are listed in Table 4.3. The materials are showing strong strain-rate sensitivity especially in comparison with quasi-static compression tests (i.e., Figs. 4.5c,d and 4.6), where mechanical properties are orders of magnitude smaller. At the high strain-rates, all samples failed at 50-80% strain levels with an enhancement in the stiffness with an increase in the strain-rate.

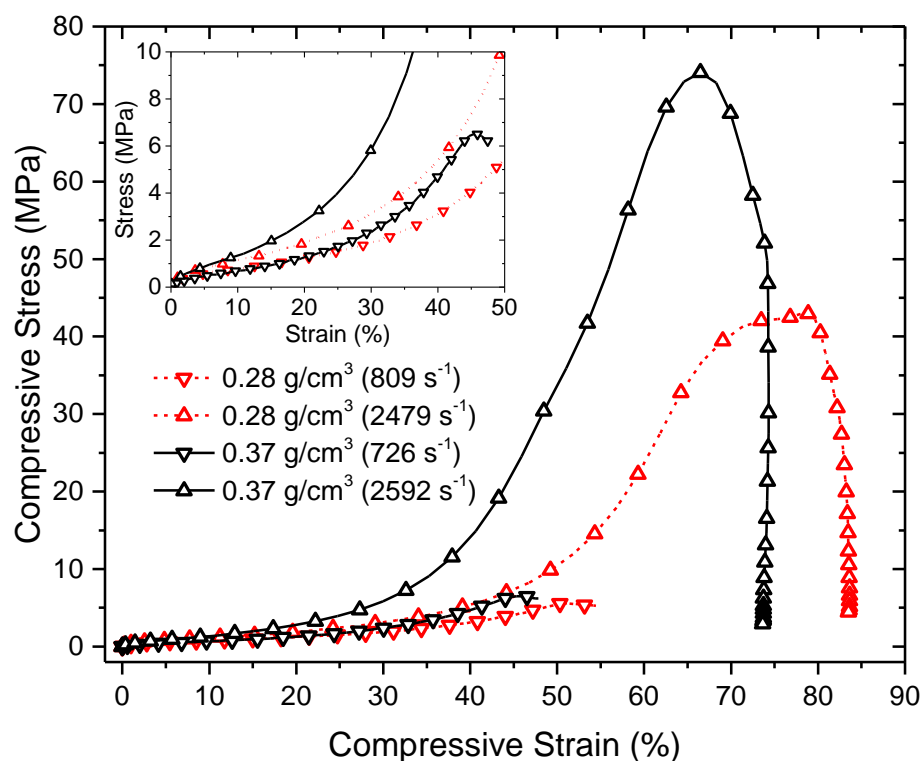


Figure 4.8. Room temperature compressive behavior of PU aerogels at bulk densities 0.28 (dash line) and 0.37 (solid line)  $\text{g/cm}^3$  at high strain rates.

### 4.3. Experimental

#### 4.3.1. Materials

All materials were commercially sourced and used without further processing. The isocyanurate node (i.e., Desmodur N3300A) was generously donated by Covestro LLC (Pittsburg, PA). The diol, triethylene glycol (TEG), and the solvents (anhydrous acetone and anhydrous acetonitrile) were sourced from Fisher Scientific (Hampton, NH). The catalyst, dibutyltin dilaurate (DBTDL), was purchased from Acros Organics. An aluminum container with dimensions of 70 cm  $\times$  70 cm  $\times$  5 cm coated with a thin layer of silicon rubber was used as the mold.

#### 4.3.2. Synthesis of Poly(isocyanurate-urethane) aerogels

In a typical synthesis, 30 mmol of N3300A with 45 mmol of TEG was dissolved in anhydrous acetonitrile (exact amounts are listed in Table S.1 in [14]). The solution was stirred for 10 min at

room conditions. Then the catalyst (DBTDL) was added to the solution. The resulting solution was stirred for another 15 min and poured into an aluminum mold. The mold was covered tightly with aluminum foil for the entire gelation and aging processes. For different densities, the gelation time was varied between 1.5 to 2 h. The aging time was set to 24 h. After aging, the wet gel was washed with a mixture of anhydrous acetone and a small amount of hexylamine (0.3% v/v) for 8 h. Then, the hexylamine modified wet gel was washed with pure anhydrous acetone for 5 times (each for 8 h) and finally washed with pentane for another 8 h. The amount of solvent at each washing step was equal to four times the volume of the wet gel. The washed wet gel was dried under ambient conditions for 24 h. Finally, the samples, which are called PU aerogel, were heated up in the oven at 40 °C for 3 h for further stabilization.

### 4.3.3. Methods

#### 4.3.3.1. Chemical characterization

Solid-state CPMAS  $^{13}\text{C}$  NMR spectra were obtained with samples cut into small pieces on a Bruker Avance III 400 MHz spectrometer with a carbon frequency of 100 MHz using a 7 mm Bruker MAS probe at a magic angle spinning rate of 5 kHz with broad-band proton suppression and the CP TOSS pulse sequence. The Total Suppression of Spinning Sidebands (TOSS) pulse sequence was applied by using a series of four properly timed  $180^\circ$  pulses on the carbon channel at different points of a cycle before the acquisition of the FID, after an initial excitation with a  $90^\circ$  pulse on the proton channel. The  $90^\circ$  excitation pulse on the proton and the  $180^\circ$  excitation pulse on carbon were set to 4.2 and 10  $\mu\text{s}$ , respectively. A contact time of 2 ms was used for cross-polarization.

#### 4.3.3.2. Physical characterization

Bulk densities ( $\rho_b$ ) were determined from the weight and the physical dimensions of the samples. Skeletal Density ( $\rho_s$ ) is considered to be  $1.23 \pm 0.005 \text{ g/cm}^3$  according to our co-author previous measurements [64]. Hydrophobicity of the aerogel surfaces was studied by means of static contact angle measurements, through a drop shape analysis system, using a goniometer (KRUSS, DSA30) and water droplets of 11.5  $\mu\text{L}$  volume. Surface areas by the Brunauer-Emmett-Teller (BET)

method were determined by nitrogen sorption porosimetry using a Micromeritics ASAP 2020 surface area and pore distribution analyzer.

#### *4.3.3.3. Structural characterization*

SEM images were taken using ZEISS SUPRA-40 FE-SEM (Carl Zeiss Microscopy GmbH, Germany) with EHT set to 3kV and occasionally 5kV. Samples for SEM images were fixed onto a copper tape. In order to reduce the charging artifact, prior to SEM imaging, samples were coated with ~7 nm Gold using Hummer-VI sputtering tool (Anatech USA, Union City, CA).

#### *4.3.3.4. Thermal characterization*

DSC was performed on a Mettler Toledo (Columbus, OH) DSC 1 in a 40  $\mu$ L aluminum crucible. Samples were heated from room temperature to 130  $^{\circ}$ C, cooled to  $-40$   $^{\circ}$ C, and subsequently heated to 200  $^{\circ}$ C. All heating and cooling rates were fixed at 10  $^{\circ}$ C  $\text{min}^{-1}$ . Tests were conducted in an  $\text{N}_2$  atmosphere. Only the last heating ramp is shown in data, and the  $T_g$  is denoted as the midpoint of the transition. TGA analysis was performed on a TGA/DSC 1 STARe System (Mettler Toledo AG Analytical, Switzerland) with a temperature range of 30–700  $^{\circ}$ C and a ramp rate of 10  $^{\circ}$ C  $\text{min}^{-1}$  under an  $\text{N}_2$  atmosphere.

#### *4.3.3.5. Mechanical characterization*

Quasi-static uniaxial tensile properties were measured using an MTI microtensile stage (MTI Instruments, Inc., Albany, NY) with a 50 lb load cell (0.2% load accuracy) and 20 nm resolution for linear scale accuracy. Dogbone-shaped samples were prepared with 3 mm thickness, 4 mm reduced section width and 11 mm gauge length. The strain rate was set to 0.001  $\text{s}^{-1}$ . The samples were then sanded to remove all sharp edges or cracks that might cause stress concentrations. Three samples at each density were tested. In order to measure the Poisson's ratios of the aerogels, a random speckle pattern was generated on the surface under the observation of the tensile test sample (which is naturally synthesized in white color) using a quick-drying black ink. DIC technique, a non-contact full-field deformation measurement method, was used to measure the surface deformations using commercially available 2D SpeckleTrack software (Framingham,

MA). During the tensile tests, a series of digital images were taken every 6 s using a Nikon camera (Model D7100) kept at a fixed position and normal to the samples.

Quasi-static compression tests were performed on an Instron mechanical testing system (Instron Inc., Model 5969, Norwood, MA) with a 500 N load cell (with an accuracy of 0.5% of the reading). The compression rate was set to 0.5 mm/min. Cylindrical-shaped samples with 20 mm diameter and 20 mm height were drilled out from a larger PU aerogel sample.

DMA was performed on a Mettler Toledo (Columbus, OH) DMA/SDTA861e. Cylindrical-shaped samples with 17 mm diameter and 4 mm thickness were prepared. The deformation mode was in compression. Samples were inserted at room temperature and cooled to  $-50\text{ }^{\circ}\text{C}$ . The sample was then heated to  $100\text{ }^{\circ}\text{C}$  at a rate of  $2\text{ }^{\circ}\text{C min}^{-1}$  while undergoing deformation at 1, 5 and 10 Hz. The deformation was force limited to 5 N, with a 200  $\mu\text{m}$  offset (5% strain) and oscillating deformation amplitude of 20  $\mu\text{m}$  (0.5% strain).

Compression experiments at high strain rates ( $800 - 2500\text{ s}^{-1}$ ) were conducted on a long split-Hopkinson pressure bar (SHPB) under ambient conditions. The SHPB consists of 304 L stainless steel striker bar, a 304 L stainless steel incident bar (8.810 mm length, 19 mm outer diameter), a solid 7075-T651 aluminum transmission bar (3660 mm long, 19 mm in diameter), and a strain data acquisition system. Disk-shaped PU samples (5–7 mm in thickness and 9.6–10 mm in diameter) were sandwiched between the incident and transmission bars. The use of an aluminum transmission bar took advantage of the low Young's modulus of aluminum ( $\sim 1/3$  of steel) to reach high signal-to-noise ratios for the weak transmitted signal through aerogels [6,65,66] and attain similar functions to those accessible with hollow transmission steel tubes [9,56] and [67]. A Cu disk pulse shaper (1.6-mm-thick, 7.4 mm in diameter) was used to reach a dynamic stress equilibrium state and constant strain rates, which is necessary for a valid SHPB experiment [59,68]. The working principle of SHPB has been well documented in the literature, including formulas for the stress, strain, and strain rate for a valid experiment [69–71].

#### 4.4. Conclusions

Herein, a mass-producible synthetic protocol for the preparation of a hydrophobic polymeric aerogel with rubber-like elasticity has been examined from the polymerization of an isocyanurate precursor (N3300A). Large patches of aerogels with densities as low as  $0.28 \text{ g/cm}^3$  and porosities as high as  $\sim 77\%$  were prepared and their mechanical properties were systematically characterized at different loading and environmental conditions. These aerogels showed high thermal stability up to  $300 \text{ }^\circ\text{C}$  with only less than 3% mass-loss while the glass transition was below or at room temperature at all densities. Notable dependencies in the mechanical behavior of the obtained aerogels have been observed with respect to bulk density and strain-rate. For instance, the aerogels were linear-elastically stretchable without any yielding up to at least 120% tensile strain. Also, the stiffness of the aerogels in the quasi-static uniaxial tension tests was significantly increased with respect to the increase in the bulk density, an increase that to our knowledge is not common among other similar aerogel counterparts. Furthermore, the aerogels were studied under cyclic loading-unloading compression tests, which pointed to a very repeatable and stable behavior with a negligible drop in maximum stresses and absorption energies after the second cycle. Dynamic properties of the aerogels have been also measured using multiple-frequency dynamic mechanical analysis at various temperatures and a split Hopkinson pressure bar system. The compressive properties at high strain rates were increased by orders of magnitude with respect to the quasi-static counter-results, indicating high strain rate dependency in this class of aerogels. Finally, it is anticipated that these materials, due to their exciting physical and mechanical properties (e.g., super-elasticity at low density), can be mass-produced with a minimum technical difficulty at a reasonable price (e.g., no need for supercritical drying) to be used for different multifunctional applications in a near future.

## CHAPTER 5

# LOW-COST, AMBIENT DRIED, SUPERHYDROPHOBIC, HIGH STRENGTH, THERMALLY INSULATING AND THERMALLY RESILIENT POLYBENZOXAZINE AEROGELS

A family of ambient-dried polybenzoxazine aerogels is prepared with a facile and scalable process as a *high-performance* polymeric aerogel with *strong and robust* thermo-mechanical properties at elevated temperatures. Those materials are *inherently flame-retardant and superhydrophobic* over the entire bulk density range (0.24-0.46 g cm<sup>-3</sup>). In addition, they are *mechanically strong* with strengths (e.g., 1 MPa at 0.24 g cm<sup>-3</sup> at room temperature) higher than those of other high-performance aerogels of similar density including polyimide, and polyamide (Kevlar-like) aerogels, as well as polymer-crosslinked X-silica, and X-vanadia aerogels, at a *significantly lower cost*. Furthermore, unlike most other glassy polymeric materials, the maximum strength of the synthesized aerogels occurs at service temperatures slightly higher than room temperature (about 50 °C), which eliminates the possibility of any drop in strength with respect to the room temperature strength up to 150 °C at all densities. At higher temperatures (up to 250 °C), the overall performance of those aerogels is also stable and robust without any significant drop in Young's modulus or strength levels, which makes them suitable for various industrial applications including high-performance structural and thermal protection applications as an alternative to the significantly more expensive polyimides.

### 5.1. Introduction

The quest for ever lighter and stronger high-performance structural materials has been continuously pursued throughout human civilization. With the advent of modern technology, that quest is fundamentally driven by three factors: microstructure (e.g., hierarchical and nanoporous structures), length-scale (e.g., size-dependent strengthening), and intrinsic material composition (e.g., the use of metal alloys) [72]. However, the limited scalability of nanostructure fabrication processes and the compromised mechanical performance of the resulting materials under harsh environmental conditions are among the main real challenges that affect practical applications [73–

75]. Scalable nano-manufacturing approaches such as sol-gel based synthesis along suitable molding are among the most highly promising methodologies for the preparation of large, low-density, mechanically strong nanostructured materials [76]. In this context, aerogels set amid the low-density materials with synergistic properties such as high specific surface areas and the hierarchical random assembly of nanoparticles [2]. It should be noted that recent novel aerogel synthetic methodologies including nanofiber-based assemblies led to low density and large specific surface area aerogels; however, these technologies also rely on several other techniques including sonication-induced gelation, electrospinning, or thermal-based cross-linking, which essentially increase the manufacturing costs and hinder the scalability [77,78]. These materials can become even more attractive through *ambient-drying* based sol-gel approaches to reach desirable scalability at low cost [12–14,20,79,80]. Over the past two decades, the mechanical properties of traditional oxide aerogels, e.g., silica, have been dramatically improved using polymer-crosslinking technologies. The resulting materials are referred to as X-aerogels [37,54,56,61,81–84].

X-aerogels bear a conformal polymer coating over their entire skeletal framework; the bulk density of the native materials may increase by a factor of three, but the mechanical properties increase by a factor of 300. Following the success of polymer-crosslinked aerogels, it was reasoned that purely polymeric aerogels with the same nanostructure as X-aerogels should have similar properties. Thus, a new class of purely polymeric aerogel has emerged. Those include aerogels based on most major polymeric classes such as polyurea [5,12,13,85–87], polyurethane [6,14,88–92], polyimide [93] and polyamide (Kevlar<sup>TM</sup>-like) [94–96], among many others. The impressive mechanical properties of those aerogels have led to a host of new applications, unthinkable for such low-density materials before, including ballistic armor protection [9,10].

As phenolic resins, polybenzoxazines (PBOs) are sturdy with low water retention, and exceptionally high glass transition and decomposition temperatures, which make them an important inexpensive alternative to engineering plastics like polyimides for high-temperature applications [97]. Previous attempts on making PBO aerogels are either accomplished through a high-temperature gelation process (e.g., PBO aerogels synthesized by Lorjai et al. [98,99]) or prepared after a supercritical drying process (e.g., PBO aerogels synthesized by Mahadik-

Khanolkar et al. [100,101]) which in both cases, scalability and commercialization are hindered. It is worth mentioning that in the Mahadik-Khanolkar et al.'s approach, the PBO aerogels have been synthesized at room temperature, which is a great advantage for commercialization [100]. Therefore, motivated by their approach, we first became interested in exchanging their PBO aerogel room-temperature supercritical-drying synthetic protocol with a room-temperature ambient-drying approach to contribute further on the scalability of the PBO aerogels. Moreover, on the aspect of mechanical properties, the previously-reported PBO aerogels have not been fully characterized by different environmental and loading conditions. Thus, we systematically studied the fundamental mechanical properties (i.e., both uniaxial and shear properties) of the ambient-dried PBO aerogels under uniaxial compression and pure torsional loading modes with various loading-unloading scenarios at elevated temperatures and different frequencies. To the best of our knowledge, this is the first study on the preparation of room-temperature ambient-dried PBO aerogels with full mechanical characterizations. These investigations will open up the route to the full commercialization of scalable and low-cost PBO aerogels.

## 5.2. Results and discussion

### 5.2.1. Materials synthesis

The benzoxazine (BO) monomer was synthesized according to our co-author's previous approach.<sup>39</sup> The BO monomer was prepared from the condensation of bisphenol A, aniline, and formaldehyde (Figure 5.1a). At room temperature, the PBO wet-gels were prepared using our co-author's reported HCl-catalyzed process in DMF solvent.<sup>39</sup> However, in this work, the gelation solvent was exchanged repeatedly, from DMF to acetone and then to acetonitrile and finally to pentane. This solvent exchange influences on the inner surface of the gel network which will eventually minimize the capillary forces of the liquid meniscus inside the pore. Then, the wet-gels were dried directly from pentane at room temperature under ambient pressure [102]. Three sets of PBO samples at three different BO monomer concentrations (i.e., 7, 10 and 12 % w/w) were prepared. The xx in PBO-xx denotes the monomer concentration. All as-prepared PBO samples were brown (darker at higher monomer concentrations), monolithic, and sturdy. In order to complete the curing process, all samples were further processed for 24 h at 200 °C in air. As it has

been shown previously, that step induces ring fusion of the aniline and the phenolic rings. The PBO sample preparation protocol is summarized in Figure 5.1b.

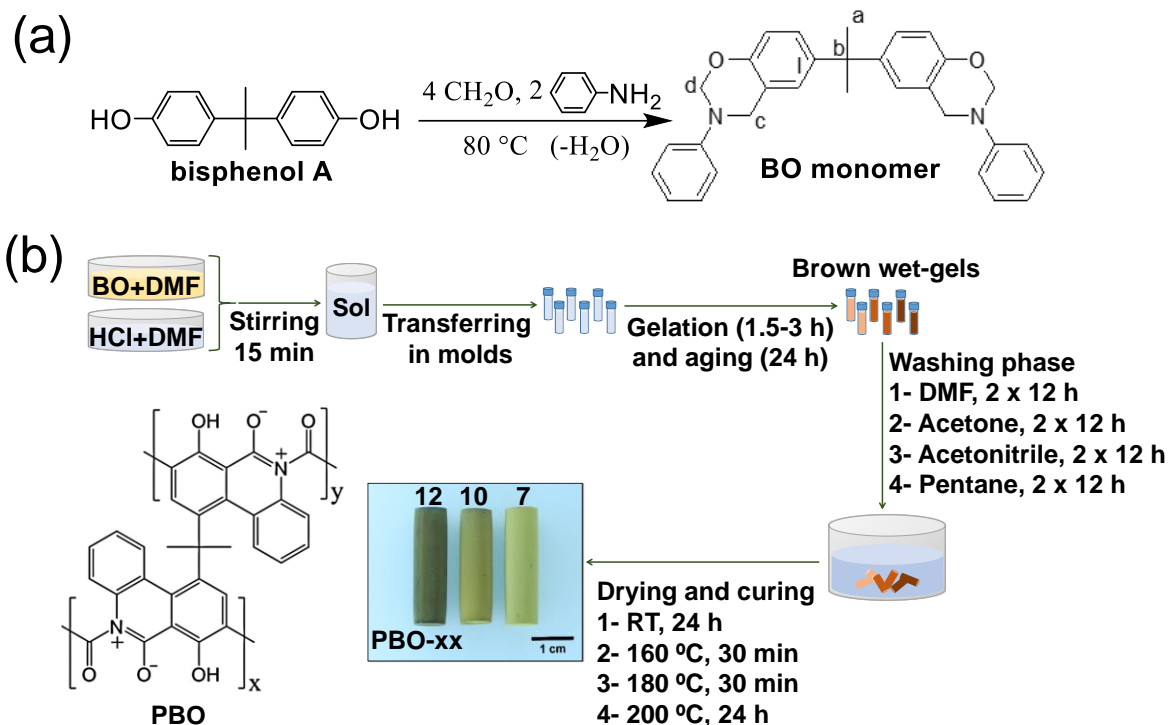


Figure 5.1. (a) The chemical synthesis of the benzoxazine (BO) monomer, and (b) The synthetic protocol of the ambient-dried polybenzoxazine (PBO) aerogels.

### 5.2.2. Chemical characterization

Ring-fusion aromatization of the aniline moiety with the phenolic moiety caused complete disappearance from the FTIR spectra of PBO-xx (Figure 5.2) of both strong absorptions at  $747 \text{ cm}^{-1}$  and  $690 \text{ cm}^{-1}$  of the BO monomer, which were attributed to the C-H out-of-plane (OOP) bending vibrations of dangling aniline. The Ph-O-C stretches at  $1229 \text{ cm}^{-1}$  for the BO monomer and the stretches of the cyclic mixed acetal/aminal at  $939 \text{ cm}^{-1}$  were replaced with a new absorption near  $1266 \text{ cm}^{-1}$ , which was attributed to the C-O stretching of the dangling phenolic moieties [100,103]. The C-N stretching of the Mannich bridges in the BO monomer, which was observed at  $1111 \text{ cm}^{-1}$ , became extremely weak in the PBO-xx aerogel samples. The absorption at  $1183 \text{ cm}^{-1}$  corresponded to the Ar-C-Ar stretching in the Bisphenol A moiety and it is also present

in the cured sample as expected. The 1700–1750  $\text{cm}^{-1}$  region could be related to C=O stretches of carbonyls.

Figure 5.3 shows the  $^{13}\text{C}$  NMR spectra of the BO monomer and of a representative PBO-10 aerogel sample. All the aromatic carbons were observed from 110 ppm to 160 ppm. As expected, the resonances of the  $\text{C}(\text{CH}_3)_2$  bridges between the phenolic moieties survived in the cured polymer, but the resonances of the carbons corresponding to the cyclic mixed acetal-aminal (marked c and d) had disappeared. Those two carbons were oxidized and either became part of a new aromatic phenoxide whose resonances overlap with the rest of the aromatic resonances, or a brand-new carbonyl that gave rise to the weak resonance at around 193 ppm.

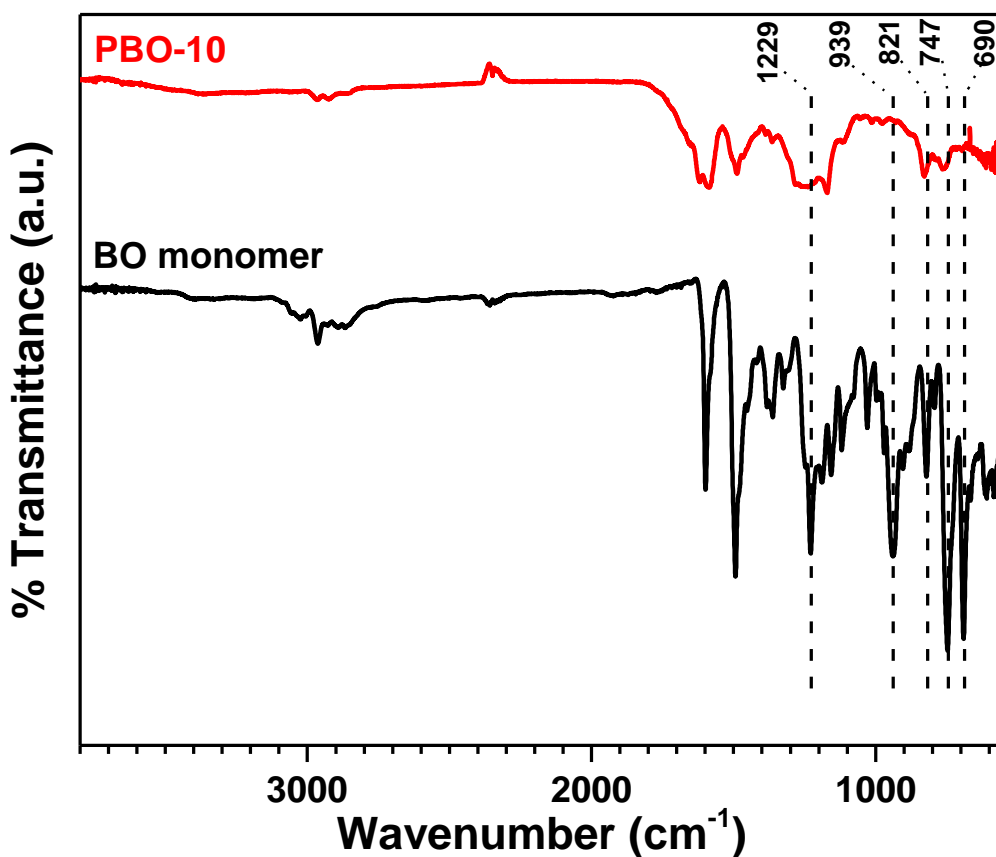


Figure 5.2. Infrared (FTIR) spectra of the BO monomer and of representative PBO-10 aerogel sample.

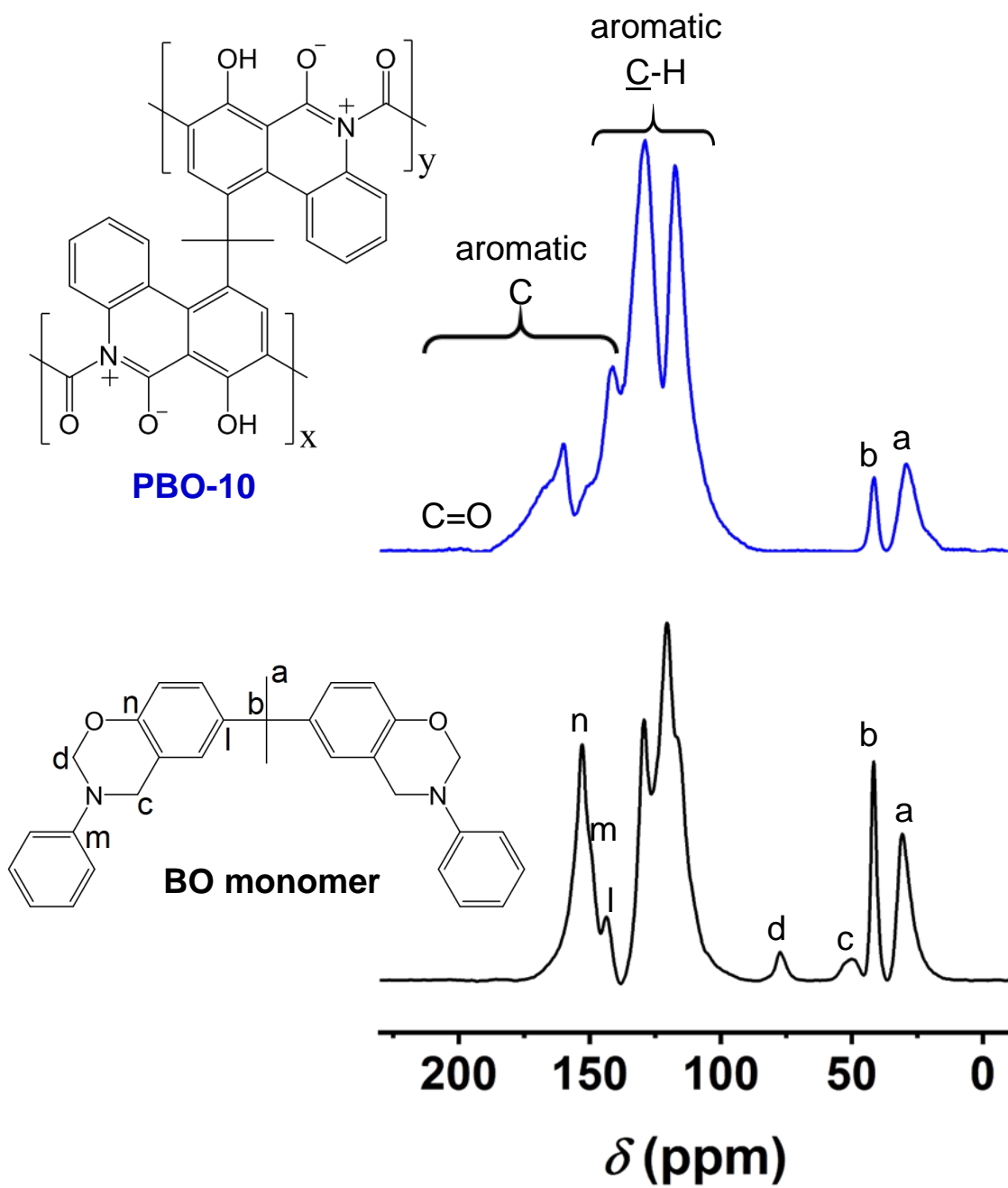


Figure 5.3. Solid-state CPMAS  $^{13}\text{C}$  NMR spectra of the BO monomer and of representative PBO-10 aerogel sample.

### 5.2.3. Physical characterization

#### 5.2.3.1. General material properties

The total linear shrinkage of the fully-cured PBO aerogels relative to their molds was about 40%. Shrinkage of traditional silica gels during aging is caused by dissolution and re-precipitation processes, which are referred to as Ostwald ripening. The latter is not relevant in the case of PBO wet-gels, which, therefore, showed zero aging shrinkage. Upon solvent exchange, polymeric gels may swell or de-swell, depending on the solvent, by phenomena akin to osmosis [66]. In the case of PBO wet-gels, no shrinkage was observed during solvent exchange from the gelation solvent (DMF) to the drying solvent (pentane). The shrinkage during ambient-pressure drying was also negligibly small (2%). Therefore, consistent with the definition of aerogels [104,105], our dry PBO monoliths are referred to as aerogels. Finally, the major part of the total shrinkage (38%) occurred during the curing process (at 200 °C in the air), which is well understood to cause oxidative ring-fusion aromatization along the polymeric backbone [100]. That process decreases the degrees of freedom along the polymeric chain and brings aromatic rings closer together inducing molecular compaction, and macroscopic shrinkage akin to what is observed in all materials classified as carbon aerogels. Bulk densities ( $\rho_b$ ) of the aerogel samples were monotonically increasing with the increase of monomer concentration. However, skeletal densities ( $\rho_s$ ) were constant and invariant of monomer concentration. For direct comparison, the density of the ambient-dried PBO samples of the present work was compared with the reported supercritically dried samples. Thus, the bulk densities obtained from the ambient-dried PBO-10 and PBO-12 samples were either equal or lower than their similar previously-reported supercritical dried samples (see Table S2 in Supporting Information). The bulk density of the ambient-dried PBO-7 was also only about 10% higher than its supercritical dried counterpart, which proves the effectiveness of our ambient pressure drying approach and justifies referring to PBO-xx as aerogels rather than xerogels.

The porous structure of the PBO aerogels was studied through N<sub>2</sub>-sorption measurements (see Figure 5.4) at all three densities. No signs of microporosity can be found in N<sub>2</sub>-sorption isotherms, which points to the fact that the PBO aerogels are partly mesoporous and mainly macroporous materials. It is worth mentioning that the hysteresis loops become wider and reach shorter saturation plateaus at higher densities, which means that the mesoporous portion of the materials

at higher densities is larger than that at lower densities samples. Quantitatively, the open pore volume and the average pore diameter of the aerogels were also calculated. As the density increases, the open pore volume ( $V_{\text{Total}}$ ), which accounts for the entire open porosity of the samples, decreases. The pore sizes calculated via the  $4V/\sigma$  are widely different from  $V = V_{\text{Total}}$  and the  $V$  from the single-point adsorption method. However, the pore sizes calculated from the BJH method are converging, especially at the highest density samples.

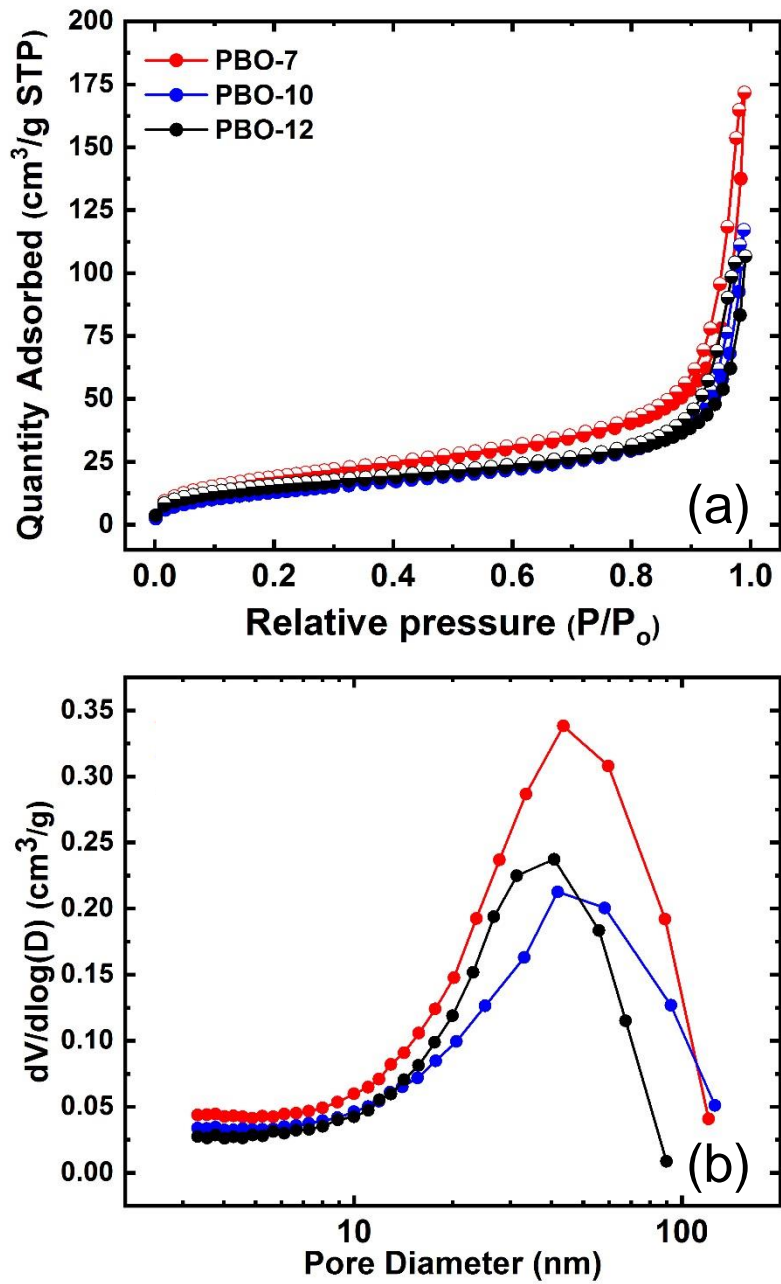


Figure 5.4.  $\text{N}_2$ -sorption measurements of the PBO aerogels; (a) Isotherm and (b) BJH plots.

### 5.2.3.2. Structural properties

SEM images of the PBO aerogel samples are shown in Figure 5.5. PBO-xx aerogel samples consisted of ~60 to 100 nm particles in agreement with N<sub>2</sub>-sorption based calculations. This cross-agreement is inherently remarkable. The aerogel microstructure formation mechanism is the result of a random secondary particle aggregation mechanism (i.e., random cluster-like models) which remained essentially the same at different densities. Water contact angles on smooth and sanded PBO aerogel surfaces were also measured at room temperature (see Figure 5.5). Practically, all aerogel samples were *superhydrophobic* with contact angles reaching  $159.0 \pm 1.6^\circ$ . Upon submerging the PBO samples in water, the silver mirror effect can be observed on these superhydrophobic surfaces due to the light reflection from the trapped water layer at both ends of the samples. It should be mentioned that these effects cannot be seen on the circumferential surface of the sample as a result of the surface re-modifications by molding. Movie S1 in the supporting [15] shows the silver mirror effect for PBO-10 in water. This kind of hydrophobicity (i.e., with contact angles above  $120^\circ$ ) is attributed to texture and renders PBO-xx aerogels suitable as an alternative low-cost, multifunctional hydrophobic coating, or for environmental remediation applications as an oil-removing material [106].

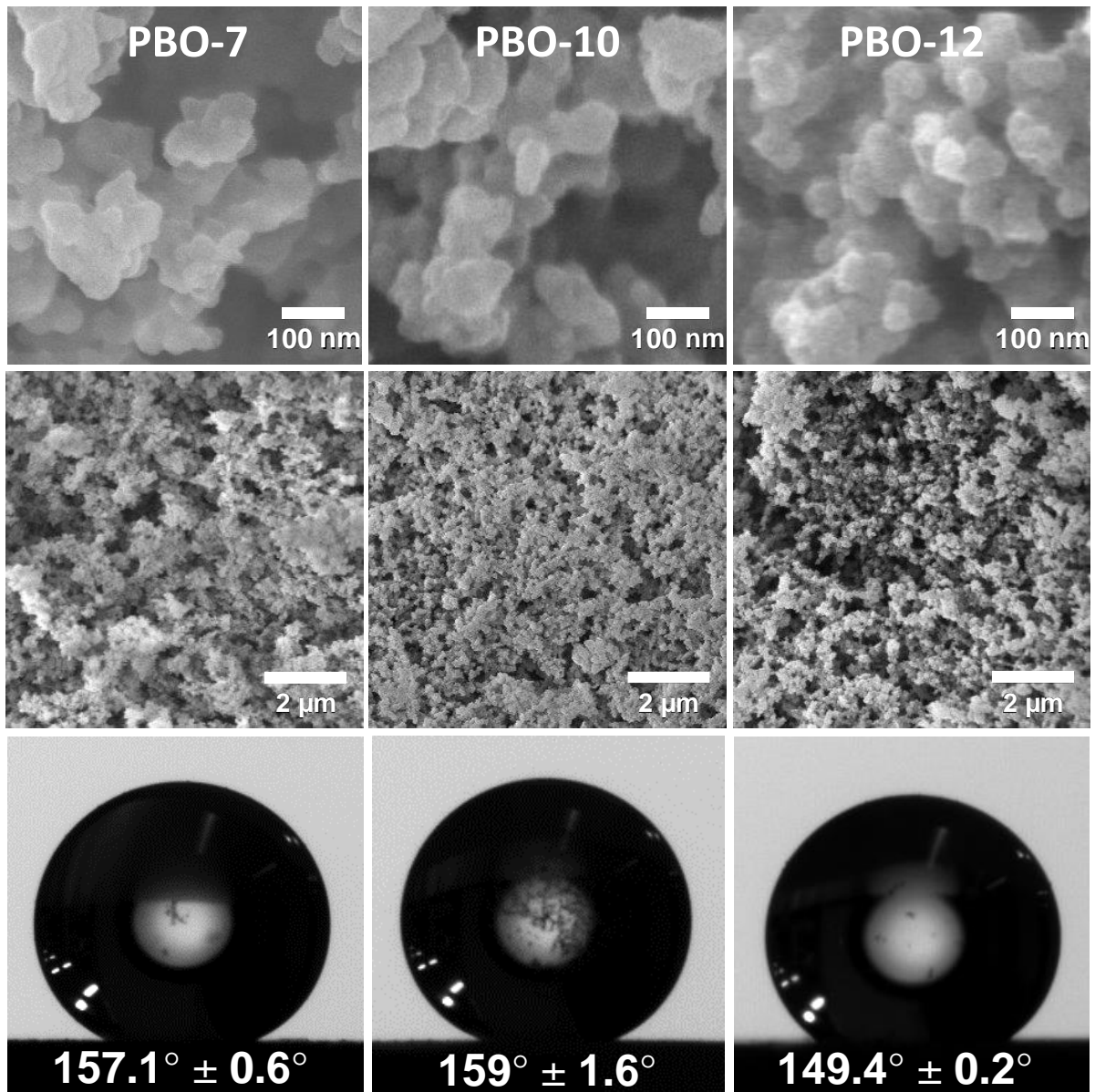


Figure 5.5. SEM micrographs at two magnifications of the PBO aerogels and the water drop (5 mL) average contact angles on the smooth and sanded PBO-xx aerogel surfaces, pointing to a superhydrophobic state.

## 5.2.4. Thermo-mechanical characterization

### 5.2.4.1. *Quasi-static uniaxial and shear properties at room temperature*

The fundamental mechanical properties of the aerogels at a low strain rate (i.e.,  $0.001 \text{ s}^{-1}$ ) were studied at room temperature (Figure 5.6). The typical stress-strain curves of the PBO samples in compression are depicted in Figure 5.6a. The compression behavior of the PBO aerogels follows three stages of elastic deformation, compaction, and densification. No buckling was observed during the compression experiments. It can be noted that the ratio of the collapse strain (i.e., strain level at the failure) to the sample's porosity is about 0.8 and remains constant at different densities. Therefore, the overall compressibility of the samples can be controlled by the sample's porosity. Furthermore, the density dependencies of Young's modulus and the yield strength (i.e., stress at 0.2% offset) of the PBO samples were studied (Figure 5.6b). Both the Young's moduli and the yield strengths of the PBO samples are clearly higher than those of polyimide [93] and polyamide (Kevlar-like) aerogels [94], as well as classical X-silica, and X-vanadia (obtained from Table 3 in [107]) aerogels over the entire density range of this study. The scaling relationship with respect to density (i.e.,  $\rho^m$ ) leads to the exponents of 3.2 and 3.6 for the Young's modulus and the yield strength, respectively. The Poisson's ratios of the PBO aerogels were also measured using a 3D Digital Image Correlation (DIC) technique concurrent with the compression tests. The strain fields along the X and Y directions of the PBO-10 aerogel sample are demonstrated as an example in the supporting information (Figure S1 in [108]). The PBO aerogels have low Poisson's ratios (0.23) even at higher densities ( $0.46 \text{ g/cm}^3$ ; the PBO-12 samples), which is an indication of only a small expansion during the compression process. The low Poisson's ratio observation is also in agreement with the porosity-controlled compressive behavior of the aerogels. Therefore, it can be concluded that after the elastic deformation, the primary plastic deformation is correlated to the self-contraction of the sample into its own pores followed by a brittle fragmentation at the rupture strain (the inset in Figure 5.6a shows a typical PBO sample before and after the compression test).

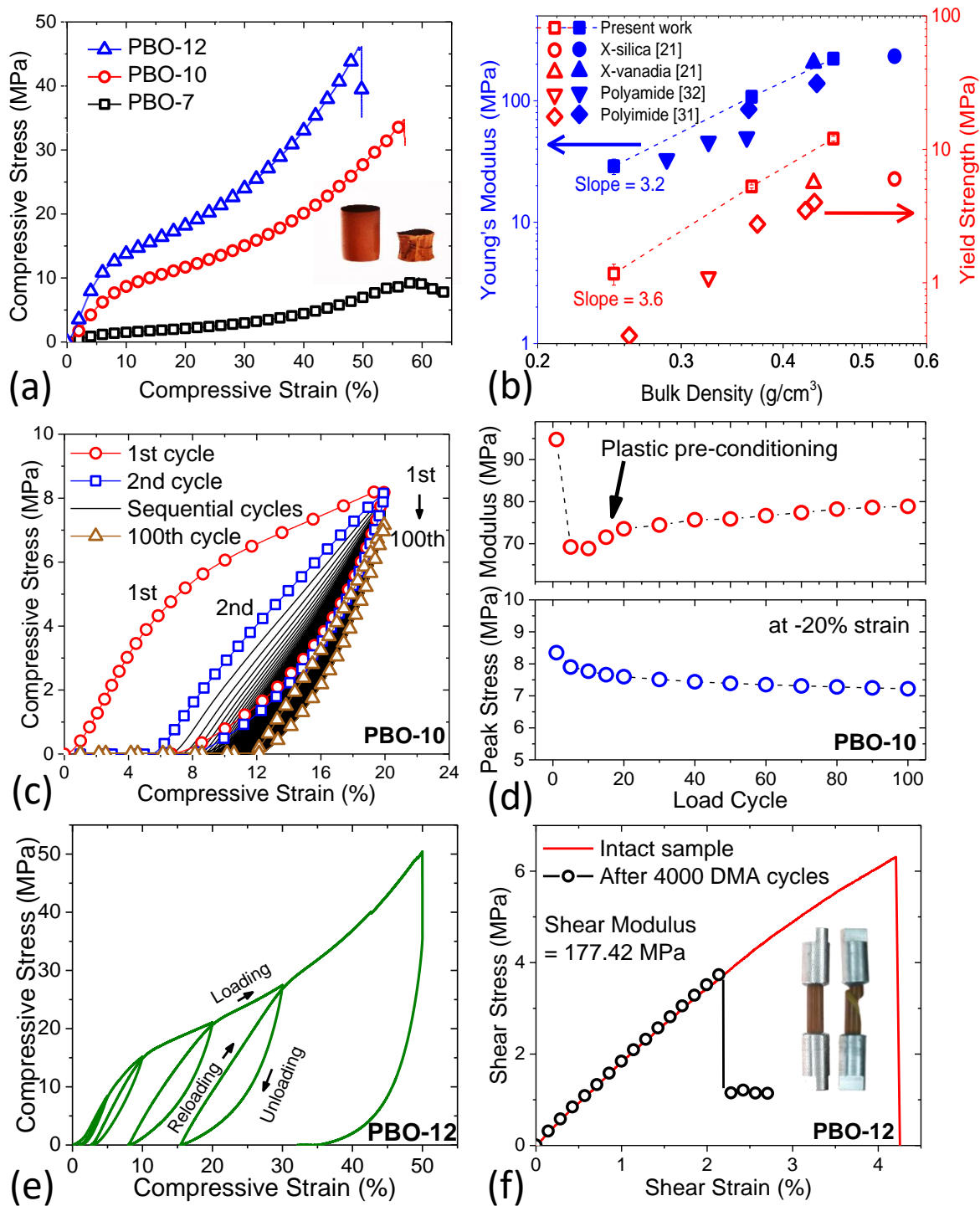


Figure 5.6. (a) Typical quasi-static uniaxial compression stress-strain responses of the PBO aerogels at different bulk densities; (b) Power-law relationships of the Young's modulus and the yield strength with bulk density of the PBO aerogels along

with those values for X-silica, X-vanadia, polyimide, and polyamide (Kevlar-like) aerogels at the same density range; (c) Cyclic quasi-static load-unload compression testing at -20% strain of PBO-10 for 100 cycles; (d) Apparent Young's modulus (top) and peak stress (bottom) values of the PBO-10 at different cycles; (e) Sequential cyclic load-unload-reload compression testing of the PBO-12 sample; and (f) Quasi-static pure torsion testing of intact and preloaded PBO-12 samples. All experiments have been carried out at room temperature. Insets in (a) and (f) are the typical PBO samples before and after quasi-static compression and pure torsion tests, respectively.

In order to examine the material durability, different cyclic loading-unloading compression tests must be carried out. Following the existence of a scaling behavior for the PBO samples with respect to their densities, cyclic loading-unloading compression tests can be carried out only at one density. Therefore, the number of required experiments can be dramatically reduced. In this way, the stability and resilient property of the aerogels under cyclic loadings were studied using a cyclic loading-unloading compression test at -20% strain level for PBO-10 as a benchmark sample (Figure 5.6c). At this strain level, a decent plastic deformation can be applied to the sample. The starting point at each cycle is the same and equal to the initial sample length for the entire 100 cycles. Transient behavior is observed in the cyclic stress-strain response of the PBO aerogel. The Young's modulus and the peak stress at -20% strain level as a function of the number of cycles are shown in Figure 5.6d. The general behavior of the peak stress is indicating a relaxation mechanism, mainly due to possible crack initiations in each cycle (only ~15% drop during 100 cycles). However, the apparent Young's modulus (i.e., modulus in Figure 5.6d) as a function of the number of loading cycles shows a drop during the first ten cycles essentially as a result of microstructural buckling, adhesion, and friction between polymeric branches as well as crack formation due to the large initial plastic deformations. Afterward, the apparent Young's modulus starts to gradually increase continuously to the last cycle. This phenomenon is called "plastic (or mechanical) pre-conditioning" which is related to the removal or a significant reduction in the polymer intrinsic post-yield softening after applying cyclic deformations.<sup>45</sup> The modulus enhancement is simultaneous with the gradual decrease in the permanent plastic strain after the unloading part of each cycle which is ultimately ended to a complete viscoelastic loading-unloading cycle without any plastic deformation at 100<sup>th</sup> cycle (see Figure 5.6c).

In the next compression test, the PBO-12 samples were considered as the benchmark and were compressed quasi-statically at five-stepped cycles at different strain levels of -5, -10, -20, -30 and -45%, in sequence. In this experiment, in contrast with the previous one, the starting point at each cycle is the end of the unloading part of the previous cycle. Figure 5.6e shows the cyclic stress-strain curve of a PBO-12 sample containing a nonlinear recovery at each unloading curve. This nonlinear unloading path is due to the material's inherent viscosity, which causes the displacement to lag behind the load. All loading curves rise back to the maximum stress point of their own previous cycle, indicating the presence of a strong memory effect in the PBO aerogels. The origin of this memory effect would be the programmed plastic stress state in the polymer chains during the previous loading cycle that can be reached after unloading and reloading steps. At each cycle, the reloading part does not follow the unloading part, resulting in the formation of a hysteresis loop. The formation of hysteresis loops is related to mechanical energy absorption and later dissipation as heat as a result of internal friction within the material. Furthermore, the torsional properties of the PBO-12 samples were studied via a quasi-static pure torsion test on intact and preloaded samples. Figure 5.6f shows the shear stress-strain curves of the PBO-12 samples. Despite the compressional ductility in the PBO aerogels, they are brittle in torsion. The typical PBO sample before and after the torsion test is shown in the inset of Figure 5.6f. For homogeneous isotropic materials, the shear modulus ( $G$ ) can be calculated using [109]:

$$G = \frac{E}{2(1 + \nu)}, \quad (5.1)$$

where  $E$  is Young's modulus and  $\nu$  is the Poisson's ratio. Using Equation 5.1 and the experimental data for the PBO-12 sample, the shear modulus is estimated to be 90.4 MPa while the experimental shear modulus (i.e., ~177 MPa) is almost two times stiffer, which confirms the existence of a *strong anisotropy* in the PBO aerogels. The results for the preloaded sample also show no drop in the shear modulus even after 4000 preloading cycles on the PBO aerogels which confirms the strong mechanical durability for these PBO aerogels.

#### 5.2.4.2. *Quasi-static compressive properties at elevated temperatures*

In order to assess the mechanical performance of the aerogels at elevated temperatures, systematic quasi-static compression experiments at different densities were carried out. The samples were

placed in a heat chamber at the target temperature for at least 45 min before starting the test. The typical stress-strain curve of PBO-12 at different temperatures are shown in the Supporting Information (check Figure S2 in [108]). The fundamental mechanical properties of the PBO samples as a function of temperature are shown in Figures 5.7a to 5.7d. The Young's modulus of the aerogels at different temperatures, shown in Figure 5.7a, is representing a gradual softening at a similar rate for all densities. At the highest temperature (i.e., 250 °C), in comparison with room temperature, Young's modulus was decreased by ~55% for PBO-7 and PBO-10 while this drop is only ~45% for PBO-12. A higher density of cross-linked networks at PBO-12 in comparison with the other two lower density samples could be related to the lower drop in Young's modulus over a similar temperature change, although it should be noted that PBO-12 is still a low-density sample (i.e., 0.46 g/cm<sup>3</sup>). On the other hand, the compressive strength (i.e., 0.2% offset yield point) has an *initial hardening* at low temperatures (Figure 5.7b) unlike most of the other glassy polymers. The increase in the strength with the rise of temperature to 50 °C might be partly related to the expansion of the trapped air molecules and a low-energy conformational adjustment process in the aerogel samples which needs to be studied further. However, pragmatically, high-temperature structural applications can definitely realize leverage from this enhancement as the compressive strength at 150 °C at all densities is equal to their room temperature values. Also, the compressibility of the aerogels is improved from ~50% to ~60% as a result of a temperature increase to 200 °C (Figure 5.7c). All these different kinds of behavior indicate that PBO aerogels are extremely *thermally-resilient* at elevated temperatures. In the last part of those experiments, the effect of temperature soaking-time on the mechanical behavior of the PBO aerogels was examined. Two sets of experiment each repeated three times (only PBO-10 was tested) were carried out in the heat chamber at the target temperature (i.e., 200 °C) for 45 min and for 24 h, respectively. The average compressive stress-strain curves of the two PBO-10 experiments are shown in Figure 5.7d. Clearly, the longer soaking time caused an overall hardening both in the modulus and the strength of the material, probably due to further conformational adjustments, which is very attractive for practical engineering applications where the material will stay at high service temperatures for a long time. Moreover, the dynamic temperature distribution of the PBO aerogels at the lowest density on a heat stage was monitored using an infrared camera (Figure

5.7e). The temperature gradient from the heat stage through the other end of the aerogel sample was continuously growing for the initial 10 s and maintained relatively unchanged after 1 min. The heat stage was at 100 °C with room temperature at 17 °C. The opposite end of the PBO sample with only 23 mm length was at 17 °C for the entire time, which indicates the strong thermal insulation properties of these aerogels. This interesting behavior led us to measure the thermal conductivities of the PBO aerogels at all densities. The aerogels showed a thermal conductivity of 0.097 W/mK at the lowest density up to 0.13 W/mK at the highest density. Compared to silica aerogel, the thermal conductivities are higher but still, the PBO aerogels can be considered as thermally insulating materials. In comparison with phenolic foams (conventional thermal insulators)<sup>49</sup> of similar density, the thermal conductivities of PBO aerogels are lower, however, compared to the phenolic aerogels including resorcinol-formaldehyde derived aerogels [3], the PBO thermal conductivities are higher [39]. The flammability of the aerogels was also studied under a direct external flame. The aerogels were self-extinguishing, and their structural integrity was retained in both carbonized and uncarbonized regions (please see Supporting Information, Movie S2 in [108]). In order to study the material degradation with respect to heat in the PBO aerogel samples, Thermogravimetric analyses (TGA) were performed and the results are shown in the supporting, Figure S3 in [108]. The TGA results show that all samples are equally resistant to heat and starting to lose mass at about 330 °C. Up to 700 °C, only 50% mass-loss, at maximum, was observed for the aerogels. These results considered together indicate that the PBO aerogels could serve the dual function of a robust fire-proof thermal insulator in a broad range of engineering applications.

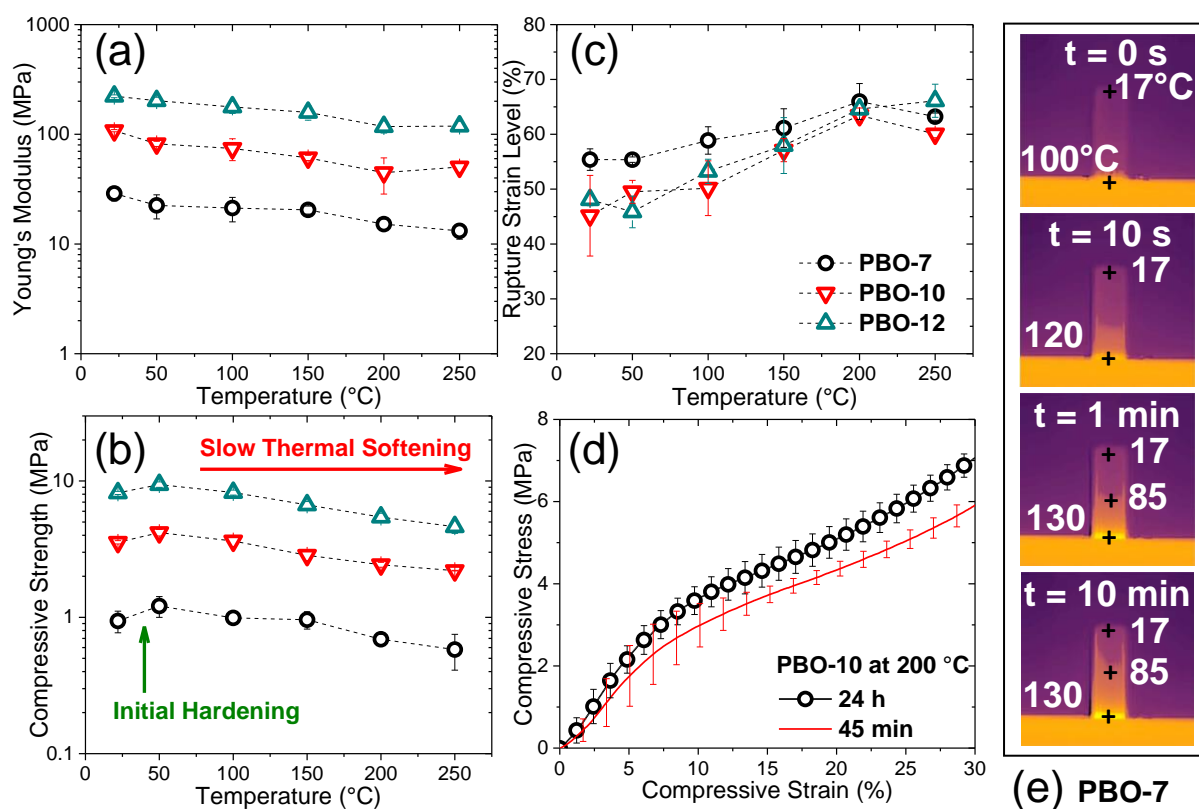


Figure 5.7. The quasi-static compressive properties of PBO aerogels at elevated temperatures: (a) Young's modulus; (b) Compressive strength; and (c) Rupture strain level. (d) The effect of thermal soaking time on the compressive stress-strain behavior of PBO-10 sample. And (e) Infrared images of PBO-7 sample (23 mm length and 7.6 mm diameter) on a heating stage for 10 min time interval.

#### 5.2.4.3. High-torque dynamic mechanical analysis in shear at elevated temperatures

Dynamic Mechanical Analysis (DMA) has been used extensively by material scientists in order to obtain the viscoelastic properties of polymeric materials. However, in most cases, the material is underloaded in their elastic region. In other words, the applied load is usually very small, and therefore the true viscoelastic response of the material might not be observed. On the other hand, while special attention must be made to carry out the experiments in the elastic region of the material, the DMA experiment can be operated at higher load/torque amplitudes using a high force/torque DMA setup. Here, the viscoelastic properties of the PBO aerogel in shear mode were measured using an Instron ElectroPuls E10000 load frame (for more details please refer to the

Experimental section). Under the cyclic rotational control mode, the PBO-12 sample was tested at 1% shear strain offset with 0.1% oscillatory shear strain amplitude at different temperatures and rotational frequencies. Under those conditions, the sample experienced a 3° rotational angle offset and a 0.5° oscillatory rotational angle amplitude, which is considered a large oscillatory amplitude for the proposed viscoelastic characterization. Figure 5.8 shows the shear viscoelastic properties of PBO-12 at different rotational frequencies and elevated temperatures. In order to reach equilibrium conditions, samples were held at least 45 min at each target temperature. Then, the steady-state response (torque) to the harmonic excitation (rotational angle) was measured. The storage modulus is shown in Figure 5.8a. In the log-log plane, the storage modulus as a function of frequency at each temperature showed a straight line. The storage was reduced with increasing temperature. Even though applied temperatures were well below the glass transition regime, the dynamic modulus was very sensitive to the temperature. The equivalence concept between frequency and temperature was then used to construct a *viscoelastic master curve* for the storage modulus following the frequency-temperature superposition principle [110]. The storage master curve for PBO-12 at the reference temperature of 59 °C is shown in Figure 5.8b. The associated shift factor plot is also shown in the inset of Figure 5.8b, namely the logarithmic shift factor,  $\log(a_F)$ . Although the storage moduli were only measured up to 1 Hz, the obtained master curve can be utilized to represent the PBO aerogel behavior over three decades of frequency (i.e., up to 1000 Hz). Loss moduli were typically lower than the corresponding storage values over the entire frequency and temperature range (Figure 5.8c). At 44 °C and above, the loss moduli were not changing. A similar trend can be seen for the behavior of  $\tan\delta$ , which is defined as the ratio of loss over storage moduli (Figure 5.8d). It is worth mentioning that the storage modulus of the aerogels tripled at the highest frequencies with respect to the quasi-static loading condition, which shows a high-frequency dependency [60].

The isofrequency shear storage and loss moduli of the PBO-12 aerogels at 1 Hz as a function of temperature are shown in Figure 5.9. The storage (loss) modulus at 60 °C was about 10% lower (higher) than that at 20 °C, indicating a robust dynamic behavior for the aerogels at elevated temperatures. In future work, the frequency-dependent storage master curve can be correlated to the shear creep master curve through the interconversion of linear viscoelastic properties.

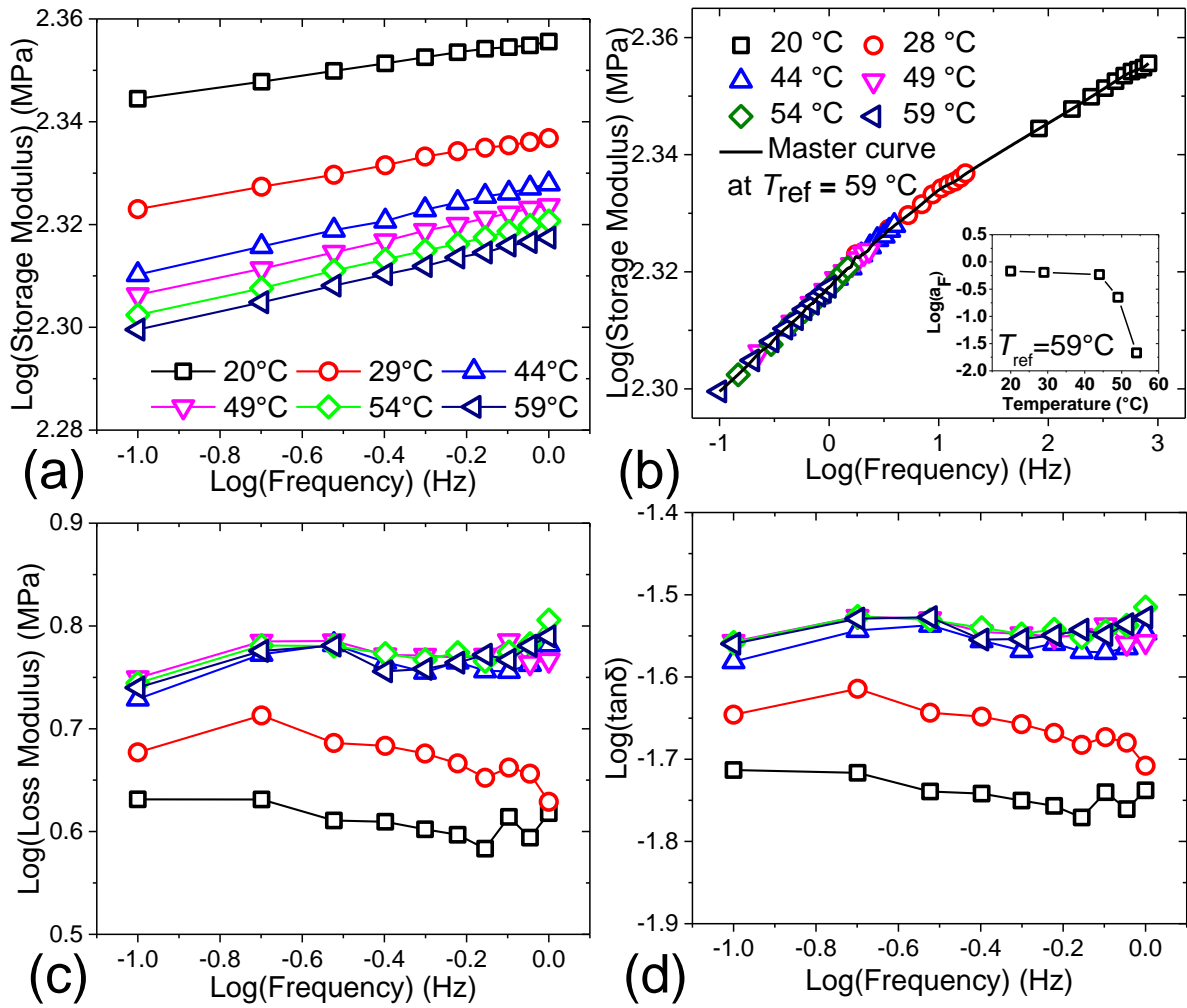


Figure 5.8. Shear viscoelastic properties of PBO-12 sample as a function of frequencies at different temperatures: (a) Storage modulus; (b) Master curve for storage modulus and the storage shift factor at different temperatures in the inset; (c) Loss modulus; and (d)  $\text{tan}\delta$ .

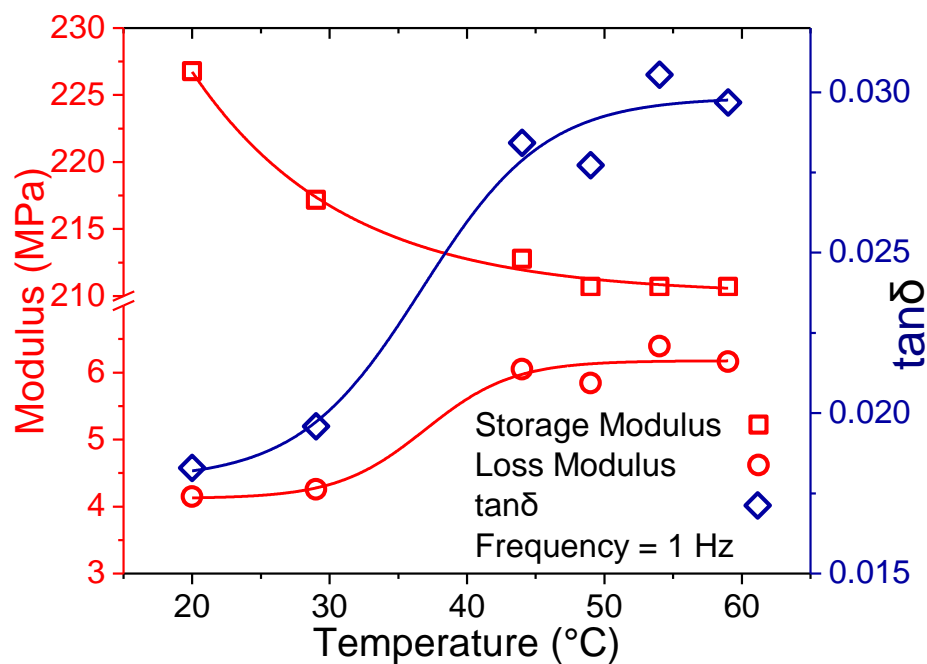


Figure 5.9. Isofrequency shear complex modulus and  $\tan \delta$  of PBO-12 as a function of temperature at the reference frequency of 1 Hz.

### 5.3. Conclusion

PBO aerogels were prepared at room temperature and dried under ambient pressure at bulk densities even lower than their supercritical dried counterparts of similar monomer concentration. Curing in air stabilized the structure and rendered the resulting materials suitable for high-temperature applications. PBO aerogels showed a highly promising combination of excellent mechanical properties with superhydrophobicity, low thermal conduction, and fire resistance. In particular, the high Young's modulus and mechanical strength of the PBO aerogels in comparison with other high-performance polymeric and polymer cross-linked aerogels at all densities generate new design options for high-performance structural applications. Their robust thermo-mechanical properties with low thermal conductivity and fire-retardancy render these aerogels excellent candidates for commercial thermal protection applications.

#### 5.4. Experimental section

*Materials:* Anhydrous acetone, anhydrous acetonitrile, anhydrous pentane, aniline, chloroform, hydrochloric acid, N,N-dimethylformamide (DMF), and sodium hydroxide were obtained from Fisher Scientific (Hampton, NH). Bisphenol A (BPA) and paraformaldehyde were supplied by Frontier Scientific (Logan, UT). 5 ml plastic vials were used as molds. All purchased materials were used without further processing except for aniline, which was extra-distilled.

*Synthesis of BO monomer:* In the synthesis, 22.82 g BPA, 12.01 g paraformaldehyde, and 18.23 mL of distilled aniline were combined in a round bottom flask. The mixture was stirred continuously for 1 h in an oil bath that was maintained at 80 °C. The mixture turned to a light yellow solid. Then chloroform was added to the flask at 55 °C until the solid was fully dissolved. Next, the solution was extracted three times with a freshly-prepared 3 M sodium hydroxide and three times with deionized water. The solution was dried over anhydrous sodium sulfate and filtered to remove water. The chloroform was then removed by heating on a hot plate at about 55 °C until the resulting mixture became a clear, viscous yellow liquid. The liquid was vacuum-dried at room temperature for 24 h, in which it became a fluffy, pale yellow, crystalline powder.

*Preparation of PBO aerogels:* In a typical synthesis, BO monomer and 12.1N HCl catalyst were separately dissolved in DMF (exact values are listed in the Supporting Information, Table S1). The two solutions were combined and stirred at room temperature for 10 minutes. The resulting sols were poured into molds and were allowed to gel. Wet-gels were aged in their molds for 24 h at room temperature. Afterward, wet-gels were removed from the molds and washed successively twice with DMF, acetone, acetonitrile, and pentane, allowing a 12 h stay in each bath. Pentane filled wet-gels were allowed to dry at room temperature and pressure for 24 h. The resulting aerogels were then step-cured in a regular oven in the air at 160 °C for 30 min, at 180 °C for 30 min, and finally at 200 °C for 24 h. The final materials are referred to as PBO-xx, where xx stands for the weight percent of the monomer concentration in the sol.

*Chemical characterization:* Solid-state CPMAS <sup>13</sup>C NMR spectra were obtained with powdered samples on a Bruker Avance III 400 MHz spectrometer with a carbon frequency of 100 MHz using

a 7 mm Bruker MAS probe at a magic angle spinning rate of 5 kHz with the CPMAS pulse sequence. The Magic Angle Spinning (MAS) pulse sequence was applied by using a series of four properly timed  $180^\circ$  pulses on the carbon channel at different points of a cycle before the acquisition of the FID, after an initial excitation with a  $90^\circ$  pulse on the proton channel. The  $90^\circ$  excitation pulse on the proton and the  $180^\circ$  excitation pulse on carbon were set to 4.2 and 10  $\mu$ s, respectively. A contact time of 3 ms was used for cross-polarization. Infrared (IR) spectra were obtained using a Nicolet-FTIR Model 750 spectrometer by mixing the sample with KBr and then compressing it to pellets.

*Physical characterization:* Bulk densities ( $\rho_b$ ) were determined from the weight and the physical dimensions of the samples. Skeletal densities ( $\rho_s$ ) were determined with helium pycnometry using a Micromeritics AccuPyc II 1340 instrument. Porosities ( $\Pi$ ) as a percent of empty space were determined from the  $\rho_b$  and  $\rho_s$  values via  $\Pi = 100 \times [(\rho_s - \rho_b) / \rho_s]$ . Surface area and pore size distributions were determined with N<sub>2</sub>-sorption porosimetry using a Micromeritics ASAP 2020 surface area and porosity analyzer equipped with a low pressure transducer (0.1 Torr) for micropore analysis. Samples for porosimetry and skeletal density determination were degassed for 24 h, at 80 °C, under a vacuum, before analysis. Average pore diameters were determined with the  $4V/\sigma$  method, where  $V$  is the pore volume per gram of sample and  $\sigma$ , the surface area determined by the Brunauer–Emmett–Teller (BET) method.  $V$  either can be taken as the single highest volume of N<sub>2</sub> adsorbed along the adsorption isotherm or can be calculated from the relationship  $V = V_{\text{Total}} = (1/\rho_b) - (1/\rho_s)$ . Materials lack macroporosity when the two average pore diameters calculated with the two different  $V$  values coincide. Scanning electron microscopy (SEM) was conducted with Au/Pd (60/40) coated samples on a Hitachi Model S-4700 field emission microscope. The sample was placed on the stub with C-dot. Thin sticky Cu strips were cut and placed on the edges and top of the sample leaving some space for the analysis. Water-contact angles were measured with a Rame-Hart Model 250 standard goniometer equipped with a high-resolution camera, using the static sessile drop method, in which a 5  $\mu$ L droplet of water is placed on the sample surface followed by imaging. The samples were prepared by cutting disks with a knife; surfaces were smoothed with sandpaper (3M Abrasives, 320 grit, part no. 32541) and were cleaned with a

stream of dry N<sub>2</sub> at high pressure. Contact angle data were collected using three separate samples for each run (formulation) immediately upon placement of the water droplets on the samples. Contact angles were determined with the DROPimage Advanced v2.4 software. A total of 10 measurements were taken by the computer in rapid succession. Results were reported as averages over the 3 samples (30 measurements) for each formulation.<sup>43</sup> For thermal insulation studies, the sample was placed on the hot plate set at 100 °C and then the dynamic temperature distribution in the sample was observed using a FLIR infrared camera (FLIR Systems, Inc., Model: FLIR ONE PRO). TGA analysis was performed on a TGA/DSC 1 STARe System (Mettler Toledo AG Analytical, Switzerland) with a temperature range of 50–700 °C and a ramp rate of 10 °C min<sup>-1</sup> under an N<sub>2</sub> atmosphere. The total thermal conductivities of all samples were calculated at 23 °C via  $\lambda_{\text{Total}} = R \times c_p \times \rho_b$ , as has been described recently.<sup>43</sup> The thermal diffusivity, R, of each sample, was determined at room temperature and atmospheric pressure with a Netzsch NanoFlash Model LFA 447 flash diffusivity instrument using disk samples ~1 cm in diameter, 2–3 mm thick. Specific heat capacities,  $c_p$ , at 23 °C were measured with powders of the samples (5–10 mg) using a TA Instruments Differential Scanning Calorimeter Model Q2000 calibrated against a sapphire standard and run from 0 to 30 °C at 1.0 °C min<sup>-1</sup> in the modulated T4P mode. The modulation amplitude was set at 0.133 °C and the modulation period at 100 s. PBO aerogel samples and two standards (rutile and corundum) were outgassed for 24 h, at 80 °C, under vacuum, before heat capacity measurements. First, the heat capacities of rutile, and corundum were measured three times each just before running the PBO samples. These experimental heat capacity values were compared with literature values and were used in order to calculate a calibration factor (= 0.969). Then, we measured the heat capacities of the three PBO aerogels under the same conditions, using three samples from each formulation. The heat capacity values of each sample were multiplied by the calibration factor.

*Mechanical characterization:* Quasi-static compression tests were performed on an Instron mechanical testing system (Instron Inc., Model 5969, Norwood, MA) with 1 kN load cell (with an accuracy of 0.5% of the reading). The compression strain rate was set to 0.001 s<sup>-1</sup>. Cylindrical-shaped samples with 7.6 mm diameter and heights ranged from 8 to 11 mm were cut from a larger

PBO aerogel cylindrical sample. Three samples at each density were tested. In order to measure the Poisson's ratios of the aerogels at room temperature, a random speckle pattern was generated on the surface under observation of the compression test sample using a quick-drying white ink. Three-dimensional DIC technique, a non-contact full-field deformation measurement method, was used to measure the surface deformations using commercially available 3D SpeckleTrack software (Framingham, MA). Two CCD cameras (BASLER acA3800-14um, Germany) and their lenses (Kowa F1.8 mm, Japan) are used to acquire the left and right images (3840 pixels  $\times$  2748 pixels) of the test sample after several calibrations. For high-temperature mechanical measurements, an Instron environmental chamber (Instron Inc., Model 5969, Norwood, MA) was used. The sample was soaked at the target temperature for at least 45 min before the measurement. Three measurements have been made at each temperature for each density. Quasi-static shear tests were performed using an Instron Electropuls E10000 load frame (Instron Inc., Norwood, MA) with a 1kN load cell and 25 Nm torque cell. Cylindrical samples with a diameter of 7.6 mm and a height of 23 mm were glued to the torsion grips. Special attention has been made to ensure that the contact shear strength is being higher than the maximum shear strength of the sample. The samples were glued to the grips using a two-part epoxy glue (J-B Weld Co., Sulphur Springs, TX) with the nominal strength of 3960 psi. The torsion rate was set to 1 °/min for quasi-static pure torsion tests. No significant normal stress was observed during the torsion tests. It is worth mentioning that the signal/noise ratio of the measurements was dramatically improved when all transducers' signals were balanced after the frame is on full power. DMA measurements in torsion were also performed on a sample with a similar configuration as the pure torsion tests using the same Instron Electropuls E10000 load frame. The sample was soaked at the target temperature for at least 45 min before the measurement. One sample is used for all measurements. In a rotational control mode, the steady-state response (torque) to the harmonic excitation (rotational angle) was measured. For each frequency, 50 cycles were considered. The rotational angle was set to a 3° offset (1% shear strain) and oscillating rotational amplitude of 0.5° (0.1% shear strain). Similar Instron environmental chamber (Instron Inc., Model 5969, Norwood, MA) was used for high-temperature measurements with at least 45 min thermal soaking.

## REFERENCES

- [1] Kistler, S. S., 1931, "Coherent Expanded Aerogels and Jellies," *Nature*, **127**(3211), pp. 741–741.
- [2] Pierre, A. C., 2011, "History of Aerogels," *Aerogels Handbook*, Springer New York, New York, NY, pp. 3–18.
- [3] Ebert, H.-P., 2011, "Thermal Properties of Aerogels," *Aerogels Handbook*, Springer New York, New York, NY, pp. 537–564.
- [4] Meador, M. A. B., Capadona, L. A., McCorkle, L., Papadopoulos, D. S., and Nicholas, L., 2007, "Structure–Property Relationships in Porous 3D Nanostructures as a Function of Preparation Conditions: Isocyanate Cross-Linked Silica Aerogels," *Chem. Mater.*, **19**(9), pp. 2247–2260.
- [5] Leventis, N., Sotiriou-Leventis, C., Chandrasekaran, N., Mulik, S., Larimore, Z. J., Lu, H., Churu, G., and Mang, J. T., 2010, "Multifunctional Polyurea Aerogels from Isocyanates and Water. A Structure–Property Case Study," *Chem. Mater.*, **22**(24), pp. 6692–6710.
- [6] Chidambareswarapattar, C., McCarver, P. M., Luo, H., Lu, H., Sotiriou-Leventis, C., and Leventis, N., 2013, "Fractal Multiscale Nanoporous Polyurethanes: Flexible to Extremely Rigid Aerogels from Multifunctional Small Molecules," *Chem. Mater.*, **25**(15), pp. 3205–3224.
- [7] Chidambareswarapattar, C., Xu, L., Sotiriou-Leventis, C., Leventis, N., Skiff, W. M., Tattershall, C. E., Kalkan, A. K., Mang, J. T., Sotiriou-Leventis, C., and Leventis, N., 2013, "Robust Monolithic Multiscale Nanoporous Polyimides and Conversion to Isomorphic Carbons," *RSC Adv.*, **3**(48), pp. 26459–26469.
- [8] Leventis, N., Chidambareswarapattar, C., Mohite, D. P., Larimore, Z. J., Lu, H., and Sotiriou-Leventis, C., 2011, "Multifunctional Porous Aramids (Aerogels) by Efficient Reaction of Carboxylic Acids and Isocyanates," *J. Mater. Chem.*, **21**(32), pp. 11981–11986.

- [9] Lu, H., Luo, H., and Leventis, N., 2011, “Mechanical Characterization of Aerogels,” *Aerogels Handbook*, Springer New York, New York, NY, pp. 499–535.
- [10] Leventis, N., and Lu, H., 2011, “Polymer-Crosslinked Aerogels,” *Aerogels Handbook*, Springer New York, New York, NY, pp. 251–285.
- [11] Rigacci, A., and Achard, P., 2011, “Cellulosic and Polyurethane Aerogels,” *Aerogels Handbook*, Springer New York, New York, NY, pp. 191–214.
- [12] Malakooti, S., Churu, H. G., Lee, A., Xu, T., Luo, H., Xiang, N., Sotiriou-Leventis, C., Leventis, N., and Lu, H., 2017, “Sound Insulation Properties in Low-Density, Mechanically Strong and Ductile Nanoporous Polyurea Aerogels,” *J. Non. Cryst. Solids*, **476**, pp. 36–45.
- [13] Malakooti, S., Churu, H. G., Lee, A., Rostami, S., May, S. J., Ghidei, S., Wang, F., Lu, Q., Luo, H., Xiang, N., Sotiriou-Leventis, C., Leventis, N., and Lu, H., 2018, “Sound Transmission Loss Enhancement in an Inorganic-Organic Laminated Wall Panel Using Multifunctional Low-Density Nanoporous Polyurea Aerogels: Experiment and Modeling,” *Adv. Eng. Mater.*, **20**(6), p. 1700937.
- [14] Malakooti, S., Rostami, S., Churu, H. G., Luo, H., Clark, J., Casarez, F., Rettenmaier, O., Daryadel, S., Minary-Jolandan, M., Sotiriou-Leventis, C., Leventis, N., and Lu, H., 2018, “Scalable, Hydrophobic and Highly-Stretchable Poly(Isocyanurate–Urethane) Aerogels,” *RSC Adv.*, **8**(38), pp. 21214–21223.
- [15] Malakooti, S., Qin, G., Mandal, C., Soni, R., Taghvaei, T., Ren, Y., Chen, H., Tsao, N., Shiao, J., Kulkarni, S. S., Sotiriou-Leventis, C., Leventis, N., and Lu, H., 2019, “Low-Cost, Ambient-Dried, Superhydrophobic, High Strength, Thermally Insulating, and Thermally Resilient Polybenzoxazine Aerogels,” *ACS Appl. Polym. Mater.*, **1**(9), pp. 2322–2333.
- [16] Beranek, L. L., and Ver, I. L., 1992, *Noise and Vibration Control Engineering - Principles and Applications*.

- [17] Pierce, A. D., 1981, *Acoustics : An Introduction to Its Physical Principles and Applications*, McGraw-Hill Book Co.
- [18] Forest, L., Gibiat, V., and Woignier, T., 1998, “Biot’s Theory of Acoustic Propagation in Porous Media Applied to Aerogels and Alkogels,” *J. Non. Cryst. Solids*, **225**, pp. 287–292.
- [19] De Vos, R., and Biesmans, G. L. J. G., 1994, “Organic Aerogels.”
- [20] Lu, H., Xiang, N., Leventis, N., and Sotiriou-Leventis, C., 2013, “Acoustic Attenuators Based on Porous Nanostructured Materials,” p. US Patent # 9,068,346 B1.
- [21] Roland, C. M., Twigg, J. N., Vu, Y., and Mott, P. H., 2006, “High Strain Rate Mechanical Behavior of Polyurea.”
- [22] Jensen, J. S., 2003, “Phononic Band Gaps and Vibrations in One- and Two-Dimensional Mass–Spring Structures,” *J. Sound Vib.*, **266**(5), pp. 1053–1078.
- [23] Salissou, Y., Panneton, R., and Doutres, O., 2012, “Complement to Standard Method for Measuring Normal Incidence Sound Transmission Loss with Three Microphones,” *J. Acoust. Soc. Am.*, **131**(3), pp. EL216–EL222.
- [24] Malakooti, S., Mohammadi, N., Mahjoob, M. J., and Mohammadi, K., 2010, “Identification of Adhesive Bond in a Multi-Layered Structure via Sound Insulation Characteristics,” *J. Mech.*, **26**(3).
- [25] Allard, J.-F., Atalla, N., and Wiley InterScience (Online service), 2009, *Propagation of Sound in Porous Media : Modelling Sound Absorbing Materials*, Wiley.
- [26] Attenborough, K., 1982, “Acoustical Characteristics of Porous Materials,” *Phys. Rep.*, **82**(3), pp. 179–227.
- [27] Bolton, J. S., Shiau, N.-M., and Kang, Y. J., 1996, “Sound Transmission through Multi-Panel Structures Lined with Elastic Porous Materials,” *J. Sound Vib.*, **191**(3), pp. 317–347.

- [28] Fahy, F., and Gardonio, P., 2007, *Sound and Structural Vibration : Radiation, Transmission and Response*, Elsevier/Academic.
- [29] Fan, H., Hartshorn, C., Buchheit, T., Tallant, D., Assink, R., Simpson, R., Kissel, D. J., Lacks, D. J., Torquato, S., and Brinker, A. C. J., 2007, “Modulus–Density Scaling Behaviour and Framework Architecture of Nanoporous Self-Assembled Silicas.”
- [30] Qiao, J., Amirkhizi, A. V., Schaaf, K., Nemat-Nasser, S., and Wu, G., 2011, “Dynamic Mechanical and Ultrasonic Properties of Polyurea,” *Mech. Mater.*, **43**, pp. 598–607.
- [31] Deymier, P. A., 2013, “Introduction to Phononic Crystals and Acoustic Metamaterials,” pp. 1–12.
- [32] Gibson, R. F., 2010, “A Review of Recent Research on Mechanics of Multifunctional Composite Materials and Structures,” *Compos. Struct.*, **92**(12), pp. 2793–2810.
- [33] Gasser, S., Brechet, Y., and Paun, F., 2004, “Materials Design for Acoustic Liners: An Example of Tailored Multifunctional Materials,” *Adv. Eng. Mater.*, **6**(12), pp. 97–102.
- [34] Tong, L., Mouritz, A. P., and Bannister, M. K., 2002, *3D Fibre Reinforced Polymer Composites*, Elsevier.
- [35] Golosnoy, I. O., Tan, J. C., and Clyne, T. W., 2008, “Ferrous Fibre Network Materials for Jet Noise Reduction in Aeroengines Part I: Acoustic Effects,” *Adv. Eng. Mater.*, **10**(3), pp. 192–200.
- [36] Pierre, A. C., and Pajonk, G. M., 2002, “Chemistry of Aerogels and Their Applications,” *Chem. Rev.*, **102**(11), pp. 4243–4266.
- [37] Leventis, N., Sotiriou-Leventis, C., Zhang, G., and Rawashdeh, A.-M. M., 2002, “Nanoengineering Strong Silica Aerogels,” *Nano Lett.*, **2**(9), pp. 957–960.
- [38] Pierre, A. C., and Rigacci, A., 2011, “SiO<sub>2</sub> Aerogels,” *Aerogels Handbook*, Springer New York, New York, NY, pp. 21–45.

- [39] Lu, X., Arduini-Schuster, M. C., Kuhn, J., Nilsson, O., Fricke, J., and Pekala, R. W., 1992, “Thermal Conductivity of Monolithic Organic Aerogels,” *Science* (80-. ), **255**(5047), pp. 971–972.
- [40] Hinze, B., and Rösler, J., 2014, “Measuring and Simulating Acoustic Absorption of Open-Celled Metals,” *Adv. Eng. Mater.*, **16**(3), pp. 284–288.
- [41] 2016, “Standard Test Method for Laboratory Measurement of Airborne Sound Transmission Loss of Building Partitions and Elements 1,” ASTM E90.
- [42] 2004, “Acoustics -- Measurement of Sound Insulation in Buildings and of Building Elements,” ISO 140.
- [43] Graff, K. F., 1991, *Wave Motion in Elastic Solids*, Dover Publications.
- [44] Biot, M. A., 1956, “Theory of Propagation of Elastic Waves in a Fluid-Saturated Porous Solid. II. Higher Frequency Range,” *J. Acoust. Soc. Am.*, **28**(2), pp. 179–191.
- [45] Biot, M. A., 1956, “Theory of Propagation of Elastic Waves in a Fluid-Saturated Porous Solid. I. Low-Frequency Range,” *J. Acoust. Soc. Am.*, **28**(2), pp. 168–178.
- [46] Biot, M. A., 1962, “Mechanics of Deformation and Acoustic Propagation in Porous Media,” *J. Appl. Phys.*, **33**(4), pp. 1482–1498.
- [47] Bourbié, T., Coussy, O., and Zinszner, B., 1987, *Acoustics of Porous Media*, Gulf Pub. Co.
- [48] Kang, H.-J., Ih, J.-G., Kim, J.-S., and Kim, H.-S., 2000, “Prediction of Sound Transmission Loss through Multilayered Panels by Using Gaussian Distribution of Directional Incident Energy,” *J. Acoust. Soc. Am.*
- [49] Pellicier, A., and Trompette, N., 2007, “A Review of Analytical Methods, Based on the Wave Approach, to Compute Partitions Transmission Loss,” *Appl. Acoust.*, **68**, pp. 1192–1212.

- [50] Chonan, S., and Kugo, Y., 1991, “Acoustic Design of a Three-layered Plate with High Sound Interception,” *J. Acoust. Soc. Am.*, **89**(2), pp. 792–798.
- [51] 2004, “ASTM E413-04, Classification for Rating Sound Insulation, ASTM International, West Conshohocken, PA, 2004.”
- [52] Schäfer, H., Milow, B., and Ratke, L., 2013, “Synthesis of Inorganic Aerogels via Rapid Gelation Using Chloride Precursors,” *RSC Adv.*, **3**, pp. 15263–15272.
- [53] Scherer, G. W., Smith, D. M., Qiu, X., and Anderson, J. M., 1995, “Compression of Aerogels,” *J. Non. Cryst. Solids*, **186**, pp. 316–320.
- [54] Katti, A., Shimpi, N., Roy, S., Lu, H., Fabrizio, E. F., Dass, A., Capadona, L. A., and Leventis, N., 2006, “Chemical, Physical, and Mechanical Characterization of Isocyanate Cross-Linked Amine-Modified Silica Aerogels,” *Chem. Mater.*, **18**(2), pp. 285–296.
- [55] Roy, S., and Hossain, A., 2008, “Modeling of Stiffness, Strength, and Structure–Property Relationship in Crosslinked Silica Aerogel,” *Multiscale Modeling and Simulation of Composite Materials and Structures*, Y.W. Kwon, D.H. Allen, and R. Talreja, eds., Springer, p. 463.
- [56] Luo, H., Churu, G., Fabrizio, E. F., Schnobrich, J., Hobbs, A., Dass, A., Mulik, S., Zhang, Y., Grady, B. P., Capecelatro, A., Sotiriou-Leventis, C., Lu, H., and Leventis, N., 2008, “Synthesis and Characterization of the Physical, Chemical and Mechanical Properties of Isocyanate-Crosslinked Vanadia Aerogels,” *J. Sol-Gel Sci. Technol.*, **48**(1–2), pp. 113–134.
- [57] Wingfield, C., Baski, A., Bertino, M. F., Leventis, N., Mohite, D. P., and Lu, H., 2009, “Fabrication of Sol–Gel Materials with Anisotropic Physical Properties by Photo-Cross-Linking,” *Chem. Mater.*, **21**(10), pp. 2108–2114.

- [58] Leventis, N., Sotiriou-Leventis, C., Mulik, S., Dass, A., Schnobrich, J., Hobbs, A., Fabrizio, E. F., Luo, H., Churu, G., Zhang, Y., and Lu, H., 2008, "Polymer Nanoencapsulated Mesoporous Vanadia with Unusual Ductility at Cryogenic Temperatures," *J. Mater. Chem.*, **18**(21), pp. 2475–2482.
- [59] Luo, H., Lu, H., and Leventis, N., 2006, "The Compressive Behavior of Isocyanate-Crosslinked Silica Aerogel at High Strain Rates," *Mech. Time-Dependent Mater.*, **10**(2), pp. 83–111.
- [60] Churu, G., Zupančič, B., Mohite, D., Wisner, C., Luo, H., Emri, I., Sotiriou-Leventis, C., Leventis, N., and Lu, H., 2015, "Synthesis and Mechanical Characterization of Mechanically Strong, Polyurea-Crosslinked, Ordered Mesoporous Silica Aerogels," *J. Sol-Gel Sci. Technol.*, **75**(1), pp. 98–123.
- [61] Mulik, S., Sotiriou-Leventis, C., Churu, G., Lu, H., and Leventis, N., 2008, "Cross-Linking 3D Assemblies of Nanoparticles into Mechanically Strong Aerogels by Surface-Initiated Free-Radical Polymerization," *Chem. Mater.*, **20**(15), pp. 5035–5046.
- [62] Pekala, R. W., Alviso, C. T., and LeMay, J. D., 1990, "Organic Aerogels: Microstructural Dependence of Mechanical Properties in Compression," *J. Non. Cryst. Solids*, **125**(1–2), pp. 67–75.
- [63] C. Tan, B. M. Fung, J. K. Newman, and C. Vu, 2001, "Organic Aerogels with Very High Impact Strength," *Adv. Mater.*, **13**(9), pp. 644–646.
- [64] Donthula, S., Mandal, C., Leventis, T., Schisler, J., Saeed, A. M., Sotiriou-Leventis, C., and Leventis, N., 2017, "Shape Memory Superelastic Poly(Isocyanurate-Urethane) Aerogels (PIR-PUR) for Deployable Panels and Biomimetic Applications," *Chem. Mater.*, **29**(10), pp. 4461–4477.
- [65] Mohite, D. P., Mahadik-Khanolkar, S., Luo, H., Lu, H., Sotiriou-Leventis, C., and Leventis, N., 2013, "Polydicyclopentadiene Aerogels Grafted with PMMA: I. Molecular and Interparticle Crosslinking," *Soft Matter*, **9**(5), pp. 1516–1530.

- [66] Mohite, D. P., Mahadik-Khanolkar, S., Luo, H., Lu, H., Sotiriou-Leventis, C., and Leventis, N., 2013, “Polydicyclopentadiene Aerogels Grafted with PMMA: II. Nanoscopic Characterization and Origin of Macroscopic Deformation,” *Soft Matter*, **9**(5), pp. 1531–1539.
- [67] Luo, H., Zhang, Y., Wang, B., and Lu, H., 2010, “Characterization of the Compressive Behavior of Glass Fiber Reinforced Polyurethane Foam at Different Strain Rates,” *J. Offshore Mech. Arct. Eng.*, **132**(2), p. 021301.
- [68] Luo, H., Roy, S., and Lu, H., 2012, “Dynamic Compressive Behavior of Unidirectional IM7/5250-4 Laminate after Thermal Oxidation,” *Compos. Sci. Technol.*, **72**(2), pp. 159–166.
- [69] Frew, D. J., Forrestal, M. J., and Chen, W., 2002, “Pulse Shaping Techniques for Testing Brittle Materials with a Split Hopkinson Pressure Bar,” *Exp. Mech.*, **42**(1), pp. 93–106.
- [70] Gray, G. T., 2000, *Classic Split-Hopkinson Pressure Bar Testing*, ASM International, Materials Park, Ohio.
- [71] Gama, B. A., Lopatnikov, S. L., and Gillespie, J. W., 2004, “Hopkinson Bar Experimental Technique: A Critical Review,” *Appl. Mech. Rev.*, **57**(4), p. 223.
- [72] Bauer, J., Meza, L. R., Schaedler, T. A., Schwaiger, R., Zheng, X., and Valdevit, L., 2017, “Nanolattices: An Emerging Class of Mechanical Metamaterials,” *Adv. Mater.*, **29**(40), p. 1701850.
- [73] Li, Q., Chen, L., Gadinski, M. R., Zhang, S., Zhang, G., Li, H. U., Iagodkine, E., Haque, A., Chen, L.-Q., Jackson, T. N., and Wang, Q., 2015, “Flexible High-Temperature Dielectric Materials from Polymer Nanocomposites,” *Nat.* 2015 5237562, **523**(7562), p. 576.
- [74] Galinski, H., Favraud, G., Dong, H., Gongora, J. S. T., Favaro, G., Döbeli, M., Spolenak, R., Fratolocchi, A., and Capasso, F., 2016, “Scalable, Ultra-Resistant Structural Colors Based on Network Metamaterials,” *Light Sci. Appl.*, **6**(5), p. e16233.

- [75] Yu, R., Ching, K.-L., Lin, Q., Leung, S.-F., Arcrossito, D., and Fan, Z., 2011, “Strong Light Absorption of Self-Organized 3-D Nanospike Arrays for Photovoltaic Applications,” *ACS Nano*, **5**(11), pp. 9291–9298.
- [76] Brinker, C. J., and Scherer, G. W., eds., 1990, *Sol-Gel Science: The Physics and Chemistry of Sol-Gel Processing*, Academic Press.
- [77] Si, Y., Yu, J., Tang, X., Ge, J., and Ding, B., 2014, “Ultralight Nanofibre-Assembled Cellular Aerogels with Superelasticity and Multifunctionality,” *Nat. Commun.*, **5**.
- [78] Qian, Z., Wang, Z., Zhao, N., and Xu, J., 2018, “Aerogels Derived from Polymer Nanofibers and Their Applications,” *Macromol. Rapid Commun.*, **39**(14), p. 1700724.
- [79] Smirnova, I., and Gurikov, P., 2017, “Aerogels in Chemical Engineering: Strategies Toward Tailor-Made Aerogels,” *Annu. Rev. Chem. Biomol. Eng.*, **8**(1), pp. 307–334.
- [80] Toivonen, M. S., Kaskela, A., Rojas, O. J., Kauppinen, E. I., and Ikkala, O., 2015, “Ambient-Dried Cellulose Nanofibril Aerogel Membranes with High Tensile Strength and Their Use for Aerosol Collection and Templates for Transparent, Flexible Devices,” *Adv. Funct. Mater.*, **25**(42), pp. 6618–6626.
- [81] Leventis, N., Sotiriou-Leventis, C., Mulik, S., Dass, A., Schnobrich, J., Hobbs, A., Fabrizio, E. F., Luo, H., Churu, G., Zhang, Y., and Lu, H., 2008, “Polymer Nanoencapsulated Mesoporous Vanadia with Unusual Ductility at Cryogenic Temperatures,” *J. Mater. Chem.*, **18**(21), p. 2475.
- [82] Mohite, D. P., Larimore, Z. J., Lu, H., Mang, J. T., Sotiriou-Leventis, C., and Leventis, N., 2012, “Monolithic Hierarchical Fractal Assemblies of Silica Nanoparticles Cross-Linked with Polynorbornene via ROMP: A Structure–Property Correlation from Molecular to Bulk through Nano,” *Chem. Mater.*, **24**(17), pp. 3434–3448.
- [83] Kim, C. H. J., Zhao, D., Lee, G., and Liu, J., 2016, “Strong, Machinable Carbon Aerogels for High Performance Supercapacitors,” *Adv. Funct. Mater.*, **26**(27), pp. 4976–4983.

- [84] Rewatkar, P. M., Taghvaei, T., Saeed, A. M., Donthula, S., Mandal, C., Chandrasekaran, N., Leventis, T., Shruthi, T. K., Sotiriou-Leventis, C., and Leventis, N., 2018, “Sturdy, Monolithic SiC and Si<sub>3</sub>N<sub>4</sub> Aerogels from Compressed Polymer-Cross-Linked Silica Xerogel Powders,” *Chem. Mater.*, **30**(5), pp. 1635–1647.
- [85] Leventis, N., Sotiriou-Leventis, C., Saeed, A. M., Donthula, S., Majedi Far, H., Rewatkar, P. M., Kaiser, H., Robertson, J. D., Lu, H., and Churu, G., 2016, “Nanoporous Polyurea from a Triisocyanate and Boric Acid: A Paradigm of a General Reaction Pathway for Isocyanates and Mineral Acids,” *Chem. Mater.*, **28**(1), pp. 67–78.
- [86] Chriti, D., Raptopoulos, G., Papastergiou, M., Paraskevopoulou, P., Chriti, D., Raptopoulos, G., Papastergiou, M., and Paraskevopoulou, P., 2018, “Millimeter-Size Spherical Polyurea Aerogel Beads with Narrow Size Distribution,” *Gels*, **4**(3), p. 66.
- [87] Wu, C., Taghvaei, T., Wei, C., Ghasemi, A., Chen, G., Leventis, N., and Gao, W., 2018, “Multi-Scale Progressive Failure Mechanism and Mechanical Properties of Nanofibrous Polyurea Aerogels,” *Soft Matter*, **14**(38), pp. 7801–7808.
- [88] Bang, A., Buback, C., Sotiriou-Leventis, C., and Leventis, N., 2014, “Flexible Aerogels from Hyperbranched Polyurethanes: Probing the Role of Molecular Rigidity with Poly(Urethane Acrylates) Versus Poly(Urethane Norbornenes),” *Chem. Mater.*, **26**(24), pp. 6979–6993.
- [89] Donthula, S., Mandal, C., Schisler, J., Leventis, T., Meador, M. A. B., Sotiriou-Leventis, C., and Leventis, N., 2018, “Nanostructure-Dependent Marcus-Type Correlation of the Shape Recovery Rate and the Young’s Modulus in Shape Memory Polymer Aerogels,” *ACS Appl. Mater. Interfaces*, **10**(27), pp. 23321–23334.
- [90] Papastergiou, M., Kanellou, A., Chriti, D., Raptopoulos, G., and Paraskevopoulou, P., 2018, “Poly(Urethane-Acrylate) Aerogels via Radical Polymerization of Dendritic Urethane-Acrylate Monomers,” *Materials (Basel)*, **11**(11), p. 2249.

- [91] Kanellou, A., Anyfantis, G., Chriti, D., Raptopoulos, G., Pitsikalis, M., Paraskevopoulou, P., Kanellou, A., Anyfantis, G. C., Chriti, D., Raptopoulos, G., Pitsikalis, M., and Paraskevopoulou, P., 2018, "Poly(Urethane-Norbornene) Aerogels via Ring Opening Metathesis Polymerization of Dendritic Urethane-Norbornene Monomers: Structure-Property Relationships as a Function of an Aliphatic Versus an Aromatic Core and the Number of Peripheral Norbornene Moieties," *Molecules*, **23**(5), p. 1007.
- [92] Papastergiou, M., Chriti, D., Damalas, D. E., Raptopoulos, G., and Paraskevopoulou, P., 2019, "Poly(Urethane-Acrylate) Aerogels from the Isocyanurate Trimer of Isophorone Diisocyanate," *J. Supercrit. Fluids*, **148**, pp. 42–54.
- [93] Chidambareswarapattar, C., Xu, L., Sotiriou-Leventis, C., and Leventis, N., 2013, "Robust Monolithic Multiscale Nanoporous Polyimides and Conversion to Isomorphic Carbons," *RSC Adv.*, **3**(48), pp. 26459–26469.
- [94] Leventis, N., Chidambareswarapattar, C., Mohite, D. P., Larimore, Z. J., Lu, H., and Sotiriou-Leventis, C., 2011, "Multifunctional Porous Aramids (Aerogels) by Efficient Reaction of Carboxylic Acids and Isocyanates," *J. Mater. Chem.*, **21**(32), pp. 11981–11986.
- [95] Saeed, A. M., Wisner, C. A., Donthula, S., Majedi Far, H., Sotiriou-Leventis, C., and Leventis, N., 2016, "Reuseable Monolithic Nanoporous Graphite-Supported Nanocatalysts (Fe, Au, Pt, Pd, Ni, and Rh) from Pyrolysis and Galvanic Transmetalation of Ferrocene-Based Polyamide Aerogels," *Chem. Mater.*, **28**(13), pp. 4867–4877.
- [96] Saeed, A. M., Rewatkar, P. M., Majedi Far, H., Taghvaei, T., Donthula, S., Mandal, C., Sotiriou-Leventis, C., and Leventis, N., 2017, "Selective CO<sub>2</sub> Sequestration with Monolithic Bimodal Micro/Macroporous Carbon Aerogels Derived from Stepwise Pyrolytic Decomposition of Polyamide-Polyimide-Polyurea Random Copolymers," *ACS Appl. Mater. Interfaces*, **9**(15), pp. 13520–13536.

- [97] Ishida, H., 2011, "Overview and Historical Background of Polybenzoxazine Research," *Handbook of Benzoxazine Resins*, H. Ishida, and T. Agag, eds., Elsevier, pp. 3–81.
- [98] Lorjai, P., Chaisuwan, T., and Wongkasemjit, S., 2009, "Porous Structure of Polybenzoxazine-Based Organic Aerogel Prepared by Sol–Gel Process and Their Carbon Aerogels," *J. Sol-Gel Sci. Technol.*, **52**(1), pp. 56–64.
- [99] Lorjai, P., Wongkasemjit, S., Chaisuwan, T., and Jamieson, A. M., 2011, "Significant Enhancement of Thermal Stability in the Non-Oxidative Thermal Degradation of Bisphenol-A/Aniline Based Polybenzoxazine Aerogel," *Polym. Degrad. Stab.*, **96**(4), pp. 708–718.
- [100] Mahadik-Khanolkar, S., Donthula, S., Sotiriou-Leventis, C., and Leventis, N., 2014, "Polybenzoxazine Aerogels. 1. High-Yield Room-Temperature Acid-Catalyzed Synthesis of Robust Monoliths, Oxidative Aromatization, and Conversion to Microporous Carbons," *Chem. Mater.*, **26**(3), pp. 1303–1317.
- [101] Mahadik-Khanolkar, S., Donthula, S., Bang, A., Wisner, C., Sotiriou-Leventis, C., and Leventis, N., 2014, "Polybenzoxazine Aerogels. 2. Interpenetrating Networks with Iron Oxide and the Carbothermal Synthesis of Highly Porous Monolithic Pure Iron(0) Aerogels as Energetic Materials," *Chem. Mater.*, **26**(3), pp. 1318–1331.
- [102] Leventis, N., Palczer, A., McCorkle, L., Zhang, G., and Sotiriou-Leventis, C., 2005, "Nanoengineered Silica-Polymer Composite Aerogels with No Need for Supercritical Fluid Drying," *J. Sol-Gel Sci. Technol.*, **35**(2), pp. 99–105.
- [103] Silverstein, R. M., Webster, F. X., and Kiemle, D. J., 2005, *Spectrometric Identification of Organic Compounds.*, John Wiley & Sons.
- [104] Vareda, J. P., Lamy-Mendes, A., and Durães, L., 2018, "A Reconsideration on the Definition of the Term Aerogel Based on Current Drying Trends," *Microporous Mesoporous Mater.*, **258**, pp. 211–216.

- [105] Du, A., Zhou, B., Zhang, Z., and Shen, J., 2013, “A Special Material or a New State of Matter: A Review and Reconsideration of the Aerogel,” *Materials (Basel)*, **6**(3), pp. 941–968.
- [106] Leventis, N., Chidambareswarapattar, C., Bang, A., and Sotiriou-Leventis, C., 2014, “Cocoon-in-Web-Like Superhydrophobic Aerogels from Hydrophilic Polyurea and Use in Environmental Remediation,” *ACS Appl. Mater. Interfaces*, **6**(9), pp. 6872–6882.
- [107] Leventis, N., Sotiriou-Leventis, C., Chandrasekaran, N., Mulik, S., Larimore, Z. J., Lu, H., Churu, G., and Mang, J. T., 2010, “Multifunctional Polyurea Aerogels from Isocyanates and Water. A Structure-Property Case Study,” *Chem. Mater.*, **22**(24), pp. 6692–6710.
- [108] Malakooti, S., Qin, G., Mandal, C., Soni, R., Taghvaei, T., Ren, Y., Chen, H., Tsao, N., Shiao, J., Kulkarni, S. S., Sotiriou-Leventis, C., Leventis, N., and Lu, H., 2019, “Low-Cost, Ambient-Dried, Superhydrophobic, High Strength, Thermally Insulating, and Thermally Resilient Polybenzoxazine Aerogels,” *ACS Appl. Polym. Mater.*, **1**(9), pp. 2322–2333.
- [109] Timoshenko, S., and Goodier, J. N., 1934, *Theory of Elasticity*, McGraw-Hill Book Co.
- [110] Ferry, J. D., 1980, *Viscoelastic Properties of Polymers*, WILEY-VCH Verlag.

## **BIOGRAPHICAL SKETCH**

Sadeq Malakooti was born and raised in Iran. He earned BSc and MSc degrees in Mechanical Engineering at the University of Birjand and Iran University of Science and Technology in Iran. Afterward, he moved to the US to pursue his second MSc in Physics at Ball State University in Indiana, graduating in 2014. Currently, Sadeq is a ME doctoral candidate at The University of Texas at Dallas (UTD) under the supervision of Dr. Hongbing Lu. Before joining UTD, he was an adjunct faculty member at Ivy Tech Community College in Indiana for two years.

## **CURRICULUM VITAE**

### **SADEQ MALAKOOTI**

Department of Mechanical Engineering

The University of Texas at Dallas, Richardson, TX 75080

E-mail: smalakooti@utdallas.edu

### **EDUCATION**

May 2020 - Ph.D. in Mechanical Engineering, The University of Texas at Dallas, Richardson, TX

THESIS - Scalable Synthesis and Dynamic Mechanical Characterization of Multifunctional Polymer Aerogels; Advisor: Professor Hongbing Lu

May 2014 - M.S. in Physics, Ball State University, Muncie, IN

THESIS - Electronic Properties of DNA Molecules under Different Electric Field Exposure Configurations; Advisor: Professor Yong Joe

May 2008 - M.S. in Mechanical Engineering, Iran University of Science and Technology, Iran

THESIS - Acoustic Radiation from a Submerged Hollow Spherical Shell; Advisor: Professor S. M. Hasheminejad

July 2005 - B.S. in Mechanical Engineering, University of Birjand, Iran

### **PUBLICATIONS**

#### Book Chapter

1. H. Luo, S. Malakooti, H.G. Churu, N. Leventis, H. Lu, Mechanical Characterization of Aerogels, in Aerogel Handbook, Edited by M. A. Aegerter, N. Leventis, and Koebel, Springer (2019) - in press

#### First-Author Peer-Reviewed Journal Papers

2. S. Malakooti, G. Qin, C. Mandal, R. Soni, T. Taghvaei, Y. Ren, H. Chen, N. Tsao, J. Shiao, S. S. Kulkarni, C. Sotiriou-Leventis, N. Leventis, H. Lu, Low-Cost, Ambient Dried, Superhydrophobic, High Strength, Thermally Insulating and Thermally Resilient Polybenzoxazine Aerogels, ACS Applied Polymer Materials, 9, 2322-2333 (2019)

3. S. Malakooti, S. Rostami, H.G. Churu, H. Luo, J. Clark, F. Casarez, O. Rettenmaier, S. Daryadel, M. Minary-Jolandan, C. Sotiriou-Leventis, N. Leventis, H. Lu, Scalable, hydrophobic and highly-stretchable poly(isocyanurate-urethane) aerogels, RSC Advances, 8, 2121421223 (2018)

4. S. Malakooti, H.G. Churu, A. Lee, S. Rostami, N. Xiang, F. Wang, Q. Lu, C. S- Leventis, N. Leventis, H. Lu, Sound transmission loss enhancement in an inorganic-organic laminated wall panel using multifunctional low-density nanoporous polyurea aerogels: experiment and modeling, *Advanced Engineering Materials*, 1700937 (2018)
5. S. Malakooti, H. G. Churu, A. Lee, T. Xu, H. Luo, N. Xiang, C. S- Leventis, N. Leventis, H. Lu, Sound insulation properties in low density, mechanically strong and ductile nanoporous polyurea aerogels, *Journal of Non-Crystalline Solids* 476, 36 (2017)
6. S. Malakooti, E.R. Hedin, Y.S. Joe, Tight-binding approach to strain-dependent DNA electronics, *Journal of Applied Physics* 114, 014701 (2013)
7. S. Malakooti, E.R. Hedin, Y.D. Kim, Y.S. Joe, Enhancement of charge transport in DNA molecules induced by the next nearest-neighbor effects, *Journal of Applied Physics* 112, 094703 (2012)
8. S. Malakooti, R. Malakooti, M. H. Valavi, Steady-state thermoelasticity of hollow nanospheres, *Journal of Computational and Theoretical Nanoscience* 8, 1727 (2011)
9. S. Malakooti, N. Mohammadi, M.J. Mahjoob, K. Mohammadi, Identification of adhesive bond in a multi-layered structure via sound insulation characteristics, *Journal of Mechanics* 26, 363 (2010)

#### **AWARDS AND HONORS**

- 2019 - Excellence in Education Doctoral Fellowship, Erik Jonsson School of Engineering, UTD
- 2019 - Best Poster Award, Research Week, The Office of Research, UTD
- 2018 - ASME Graduate Student Award (North Texas Section)
- 2017 - Louis Beecherl, Jr. Graduate Fellowship, Erik Jonsson School of Engineering, UTD
- 2016 - PhD Fellowship in Mechanical Engineering, Erik Jonsson School of Engineering, UTD
- 2015 - Jonsson School Grad. Study Scholarship, Erik Jonsson School of Engineering, UTD
- 2014 - Most Recognized Graduate Student, Graduate School, BSU
- 2013 - Cooper Science Award, Graduate School, BSU
- 2011 - Graduate Merit Fellowship, Graduate School, BSU